Thermal-fluid simulation of an air-to-CO_2 finned coil evaporator

R Strydom

Dissertation submitted in fulfilment of the requirements for the degree *Master* in Engineering at the Potchefstroom Campus of the North-West University

Supervisor: Dr. Martin van Eldik

Co-Supervisor: Mr. Werner Kaiser

November 2013

It all starts here ™

NORTH-WEST UNIVERSITY
YUNIBESITI YA BOKONE-BOPHIRIMA
NOORDWES-UNIVERSITEIT
®

Acknowledgements

The author of this thesis is very grateful for all of those involved in making this study possible.

My father, Rian, I thank you for your unfailing support, exceptional insight and for being a living example of determination. Thank you for the opportunity and financial support enabling my studies. My mother, Ina, I thank you for always believing in me and for your endless love, unconditional care and understanding. My sister, Daniëlle, I thank you for all your love, support and great enthusiasm.

You will always be my inspiration.

To my fiancé, Marti, thank you for your patient encouragement, love and support during this study. I could not have done it without you. I love you.

To my supervisor, Dr. Martin van Eldik, thank you for your enthusiasm, time, patience and financial support, making it possible for me to study fulltime. Also, thank you for your excellent guidance and advice in this field of study. I will never forget it.

To my co-supervisor, Mr. Werner Kaiser, thank you for your time, patience and invaluable insight. Also, I thank you for always being available for a quick enquiry.

To Mr. Izak Potgieter, thank you for your brilliant insight into heat pumps and for your assistance with the technical aspects of this study.

Lord, you are ever-present in your grace and love.

Abstract

Title:	Thermal-fluid simulation of an air-to-CO_2 finned coil evaporator.
Author:	Mr. Ruben Strydom
Supervisor:	Dr. Martin van Eldik
Co-supervisor:	Mr. Werner Kaiser
School:	School of Mechanical and Nuclear Engineering, North-West University.
Degree:	Master of Engineering (M.Eng Option B).

The increasing global pressure to phase out CFC's and HFC's has resulted in research focusing again on the use of natural refrigerants. CO_2 is one alternative that has very good thermal-fluid characteristics. However, a low critical point of 31.1°C and 73.2 Bar summons some challenges in the use of CO_2 in vapour compression heat pump cycles. This necessitates the implementation of a trans-critical cycle, generating much higher pressures than conventional heat pumps. The development of these trans-critical CO_2 heat pumps requires research and technical improvements in their components.

One such component is the finned coil evaporator used to transfer energy from air to the refrigerant. To aid in the design and development of this component, simulation models are required. However, the accuracy of these models depends strongly on the empirical correlations implemented, and therefore the use of accurate heat transfer and pressure drop correlations are important. Since CO_2 has some unique thermal-fluid characteristics, heat transfer and pressure drop correlations are still a prime research specific.

Thus, the present study aimed to develop a simulation model that incorporates current and accurate refrigerant-, and moist air-, heat transfer and pressure drop correlations. Using the NIST software package, EVAP-COND, verification of the simulation model were achieved, where the largest difference in the prediction of heat transfer rate was 1.7% with EVAP-COND as reference. The discrepancies are attributed to the updated correlations used in the present study. The developed model predicted 92.6% of the EVAP-COND predictions, to within ±20%.

The installation of a fully instrumented finned coil heat exchanger was done to upgrade an existing test bench. This enabled the generation of experimental data for a number of operating conditions and the validation of the simulation model with a maximum difference in heat transfer rate of 8.7%. However, the amount of lubricant in the system had significant detrimental effects on the heat transfer coefficient. A first order attempt at the implementation of a degradation factor in a modified simulation model had some success. In addition, large measurement uncertainties resulted in the experimental latent heat transfer rate data being disregarded.

The simulation of five extra RH conditions in EVAP-COND and the developed simulation served as an addition to the experimental conditions, which showed that the simulation agrees with the trend of an increase in inlet relative humidity as reported from literature. The simulation model was able to predict 82% of the experimental data to within ±20%. The developed simulation identified dehumidification to occur under the same conditions as EVAP-COND. Also, the developed simulation calculates the saturation point in the same vicinity as found in both EVAP-COND and the experimental data.

Good agreements between the data sets lead to the conclusion that the correlation of Wang *et al.* (2002) is applicable to the geometry of the wavy finned coil and that the Cheng *et al.* (2008a&b) correlation is applicable for the experimental ranges of this study.

It is recommended that the effects of lubricant be included in a further model development while a validation over a wider range of operating conditions would be of great interest.

Uittreksel

Titel:	Termiese-vloei simulasie van ‘n lug-tot-CO_2 gevinde-buis verdamper.
Outeur:	Mr. Ruben Strydom
Studieleier:	Dr. Martin van Eldik
Hulp- Studieleier:	Mr. Werner Kaiser
Skool:	Skool vir Meganiese en Kern Ingenieurswese, Noord-Wes Universiteit.
Graad:	Magister in Ingenieurswese (M.Eng Opsie B).

As gevolg van die toenemende druk op die uitfasering van CFC’s en HFC’s, is daar ‘n skuif in navorsing op koelmiddels. Die fokus is weer terug op natuurlike kandidate waar CO_2 een van die alternatiewe is met baie goeie termiese-vloei karakteristieke. Alhoewel, ‘n lae kritiese punt van 31.1°C en 73.2 Bar probleme veroorsaak in die gebruik van CO_2 in damp-kompressie hittepomp siklusse. Die implementering van ‘n trans-kritiese siklus word ‘n noodsaaklikheid, en genereer dus baie hoër drukke as konvensionele hitte pompe. Die ontwikkeling van hierdie trans-kritiese CO_2 hitte pompe vereis verdere navorsing en tegniese verbetering in hul komponente.

Een van hierdie komponente is die gevinde-buis verdamper wat gebruik word om energie vanaf die lug na die koelmiddel te skuif. Simulasie modelle word noodsaaklik om die ontwerp en ontwikkeling van hierdie komponent te ondersteun. Die akkuraatheid van hierdie modelle is sterk afhanklik van die empiriese korrelasies wat hulle implementeer en dus is die gebruik van akkurate hitte-oordrag en drukval korrelasies baie belangrik. Omdat CO_2 ‘n aantal baie unieke termiese-vloei eienskappe besit, is die ontwikkeling van hierdie korrelasies steeds ‘n sterk navorsings onderwerp.

Dus het die huidige studie as mikpunt, die ontwikkeling van ‘n simulasie model wat huidige en akkurate koelmiddel- en vogtige lug-, hitte-oordrag en drukval korrelasies gebruik. Deur die NIST sagteware pakket, EVAP-COND, te gebruik is die verifikasie van die simulasie model bewerkstellig en is die grootste verskil in hitte-oordrag tempo voorspelling, 1.7% met EVAP-COND as verwysing. Die teenstrydighede is toegeskryf aan die huidige korrelasie wat gebruik is in die ontwikkelde simulasie model. Die huidige model voorspel 92.6% van al die EVAP-COND voorspellings binne ±20%.

Die installasie van ‘n volledig geïnstrumenteerde gevinde-buis hitte ruiler is gedoen as opgradering van ‘n bestaande toets bank. Hierdie opgradering het die generering van eksperimentele data vir verskeie werks kondisies moontlik gemaak, en is gevolglik gebruik om die simulasie model te valideer met die grootste verskil in hitte-oordrag tempo 8.7%. Die hoeveelheid smeermiddel in die stelsel het alhoewel ‘n beduidende nadelige invloed op die hitte-oordrag koëffisiënt gehad. ‘n Eerste orde implementering van ‘n degraderings faktor is in ‘n gemodifiseerde simulasie model gebruik met matige sukses. Hoë meetings onsekerhede het ook gely na die verwerping van die eksperimentele latent hitte-oordrag tempo data.

As toevoeging tot die eksperimentele kondisies is vyf ekstra RH kondisies gesimuleer in EVAP-COND en die huidige model, wat wys dat die model ooreenkom met die tendens van ‘n verhoging in relatiewe humiditeit soos aangehaal uit die betrokke literatuur. Die huidige model het 82% van al die eksperimentele data voorspel binne ±20%. Onvogtiging is ook akkuraat geïdentifiseer om plaas te vind onder dieselfde kondisies aangedui deur EVAP-COND. Daarbenewens bereken die huidige simulasie die versadigings punt in dieselfde omgewing as EVAP-COND en soos gevind in die eksperimentele data.

Uit die goeie ooreenstemming tussen die data stele kan dit afgely word dat die korrelasie van Wang *et al.* (2002) toepaslik is vir die geometrie van die golf-vorm gevinde-buis hitte ruiler en dat die Cheng *et al.* (2008a&b) korrelasie ook van toepassing is op die eksperimentele reeks kondisies van hierdie studie.

Dit is aanbeveel dat die effekte van smeermiddel ingesluit word in ‘n verdere model ontwikkeling en dat validasie oor ‘n weier reeks werks kondisies gedoen word.

Table of contents

List of figures

List of tables

Nomenclature

A	: Surface area	m^2
A_{ff}	: Free flow area	m^2
A_f	: Total fin area	m^2
A_t	: Total outside tube area	m^2
A_o	: Total outside surface area ($A_t + A_f$)	m^2
B	: Forces acting on the body of CV	N
Cp	: Constant pressure specific heat	$J/(kg.K)$
D_c	: Collar diameter ($D_o + 2\delta_f$)	m
D_{eq}	: Equivalent diameter	m
D_h	: Hydraulic diameter	m
D_i	: Inner diameter of tube	m
D_o	: Outer diameter of tube	m
f	: Friction factor	-
F_s	: Fin spacing	m
Fr	: Froude number	-
G	: Mass flux	kg/m^2
g	: Gravitational acceleration, constant equal to 9.81	m/s^2
H	: Height	m
h	: Heat transfer coefficient	$W/(m^2 \cdot K)$
h_m	: Mass transfer coefficient	$kg/(m^2 \cdot s)$
i	: Enthalpy	J/kg
j	: Colburn-j factor for heat transfer	-
k	: Thermal conductivity	$W/(m \cdot K)$
L	: Length	m
Le	: Lewis number	-
m	: Function used in the Schmidt (1949) approximation	-
M	: Molecular weight	$kg/kmol$
$\dot{m}$	: Mass flow	kg/s

N	: Number of tube rows	-
Nu	: Nusselt number	-
P	: Total or stagnation pressure	Pa
P_l	: Longitudinal tube spacing	m
Pr	: Prandtl number	-
p_r	: Reduced pressure	-
P_t	: Transverse tube spacing	m
$\dot{Q}$	: Rate of energy transfer	W
q	: Heat flux	W/m^2
R_{eq}	: Equivalent circular fin radius as defined by Schmidt (1949)	m
Re	: Reynolds number	-
RH	: Relative humidity	%
r_o	: Outer radius of tube	m
S	: Nucleate boiling suppression factor	-
T	: Temperature	K
u	: Internal energy	J/kg
V	: Velocity	m/s
V_m	: Mean average velocity of the vapour phase	m/s
~~V~~	: Volume	m^3
$\dot{W}$	: Work done on the fluid	J/s
We	: Weber number	-
Z	: Elevation above a specified datum line	m
x	: Vapour quality	-
X_L	: Geometric parameter	m
X_M	: Geometric parameter	m

Greek

ε	: Void fraction	-
η	: Surface efficiency	-
ω	: Humidity ratio	kg_{water}/kg_{air}
ϕ	: Function used in the Schmidt (1949) approximation	-

ρ	: Density	kg/m^3
θ	: Angle	rad
μ	: Dynamic viscosity	$kg/(m \cdot s)$
σ	: Surface tension	N/m
τ	: Shear forces acting on the CV surface	N
δ	: Thickness	m

Subscripts

a : Air

A : Annular

avg : Average

cb : Convective boiling

D : Dryout

Dc : Based on the collar diameter

de : Dryout completion

di : Dryout inception

e : Outlet

f : Fin

H : Homogeneous

i : Inlet, Inner

I : Intermittent

IA : Intermittent-Annular transition

inc : Increment

l : Latent, Liquid

lv : Liquid-Vapour

LO : Considering the total vapour-liquid flow as liquid flow

M : Mist

nb : Nucleate boiling

o : Outer

r : Refrigerant (R 744 or CO_2)

s : Sensible

sh : Superheat zone

t : Tube

T : Total

tp : Two-phase

v : Vapour

w : Refer to water condensate film

Y : Correction factor

CHAPTER 1:
Introduction

1.1. Background

Traditionally, synthetic chlorofluorocarbon (CFC) and hydro chlorofluorocarbon (HCFC) based substances, have been the first candidates for use in the design of refrigeration systems. The Montreal protocol (effective since 1 January 1989) depicted the systematic production-, and application-, phase out of substances responsible for stratospheric ozone depletion (Austin & Sumathy, 2011). Adopted on 11 December 1997, the Kyoto Protocol included the aim that parties must legally commit to reducing their emissions of so-called greenhouse gasses that contribute to global warming (Hare, 1998). In agreement to this, the Copenhagen accord (United Nations, 2009) followed and showed support of the Kyoto protocol policies, although not a legally binding document.

This led to renewed interest in alternative natural refrigerant substances. One such substance that shows potential is carbon dioxide (CO_2). Table 1 (Kim *et al.*, 2004) gives some characteristics and properties of CO_2 (R-744) in comparison to other refrigerants.

Table 1: Properties and characteristics of refrigerants (Kim *et al.*, 2004).

	R-12	R-22	R-134a	R-407C	R-410A	R-717	R-290	R-744
ODP	1	0.05	0	0	0	0	0	0
GWP	8500	1700	1300	1600	1900	0	3	1
Flammability	No	No	No	No	No	Yes	Yes	No
Toxicity	No	No	No	No	No	Yes	No	No
Standard boiling point [°C]	-29.8	-40.8	-26.2	-43.8	-52.6	-33.3	-42.1	-78.4
Critical pressure [Bar]	41.1	49.7	40.7	46.4	47.9	114.2	42.5	73.8
Critical temperature [°C]	112	96	101.1	86.1	70.2	133	96.7	31.1
First commercial use as refrigerant	1931	1936	1990	1998	1998	1859	?	1869
Today	Older systems	No new production	Still Common	Used as replacement	Used as replacement	Used	Used	Used

R-12: *Dichlorodifluoromethane (Freon-12)* ***R-22:*** *Chlorodifluoromethane (Freon-22)*

R-134A*: 1,1,1,2-Tetrafluoroethane* ***R-407C:*** *Mixture of difluoromethane, pentafluoroethene and 1,1,1,2-tetrafluoroethane*

R-410A: *Mixture of difluoromethane and pentafluoroethene* ***R-717:*** *Ammonia R-290: Propane* ***R-744:*** *Carbon dioxide*

As can be seen from Table 1, the combination of very low Global Warming Potential (GWP) and a zero Ozone Depletion Potential (ODP); together with non-toxicity, non-flammability and good availability characteristics (Sawant *et al.*, 2003), makes CO_2 especially suited for refrigeration applications. Apart from these environmental benefits, CO_2 has some excellent thermo-physical properties. These include: high specific heat, high thermal conductivity, high vapour viscosity, low

liquid viscosity and very low surface tension (Zilio *et al.*, 2007) (Cheng *et al.*, 2006). These make for some unique heat transfer and two-phase flow characteristics.

However, it has been reported that thermal energy systems such as heat pumps using CO_2 are less effective than conventional systems (Yun & Kim, 2009). This is partly due to the inability of effectively transferring heat to ambient conditions below the critical point ($31.1°C$ and $73.8Bar$) and leads to the implementation of a trans-critical cycle as shown in Figure 1 (Huai *et al.*, 2004).

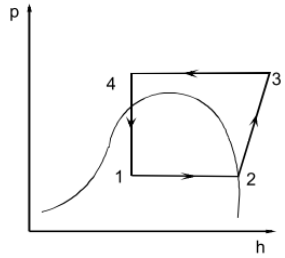

Figure 1: Trans-critical CO_2 cycle from Huai *et al.* (2004).

In this figure (Figure 1), the line between point one and two represents CO_2 evaporation taking place below the critical point (subcritical). The evaporated CO_2 gas is then compressed (point two to point three) to a pressure above the critical point (supercritical). From point three to point four, gas cooling takes place in this supercritical state and then from point four to point one, is expanded back to the lower pressure subcritical state. These changes between sub- and supercritical states form a trans-critical cycle.

As a result, the subcritical-side evaporation process occurs closer to the critical point than with conventional refrigerants (Kim *et al.*, 2004). Subcritical refrigerant pressures are thus higher than with conventional refrigerants and a lower subcritical refrigerant pressure drop, during the evaporation process, has been reported (Bendaoud *et al.*, 2010).

The properties mentioned above entail higher vapour densities and flow velocities (Pettersen *et al.*, 1998) which enable a 60% to 70% reduction in typical pipe diameters (Kim *et al.*, 2004). Finned coil heat exchangers offer a larger outside heat transfer area to core volume ratio, since a reduction in internal heat transfer area is possible, due to an increased CO_2 heat transfer coefficient (Kim *et al.*, 2004). The use of these heat exchangers as the evaporator component in air-source heat pump water heaters, such as the already available Ecocute system (Enex-ref, 2013), is common. Thus, CO_2 finned coil heat exchanger geometries only slightly differ from conventional geometries.

The above-mentioned inefficiency of CO_2 systems can be addressed (Yun & Kim, 2009) by increasing the performance of CO_2, finned coil heat exchangers. An integral part in this process is the accurate theoretical simulation of this component (Sarkar *et al.*, 2006); therefore, accurate correlations that predict heat transfer and pressure drop in the flow boiling process of CO_2 must be found (Austin & Sumathy, 2011).

In general, the heat transfer coefficient on the airside is smaller than that of the CO_2 refrigerant in a typical finned coil evaporator, leading to the overall heat transfer being more sensitive to this smaller airside coefficient (Austin & Sumathy, 2011). This highlights the need for the accurate prediction of the more dominant airside coefficient, especially when used in the simulation of such heat exchangers.

Various airside heat transfer and pressure drop correlations are available in open literature (Kim *et al.*, 1999, Wang & Chi, 2000). These correlations are highly dependent on geometric parameters such as fin type, fin spacing, fin thickness, tube diameter, tube spacing and number of tube rows (Kim *et al.*,

1999, Chen & Wang, 2008). Kim *et al.* (1999) reported that airside correlations usually miss-predict the heat transfer coefficients outside the range of the applicable parameters used to set up these correlations. Therefore, the correlation chosen to simulate the finned coil should have parameter ranges that closely match those of the finned coil.

Both Webb, 1990 and Kim *et al.,* 1997 developed correlations based on or largely including the faulty Beecher & Fagan, 1987 data set. However, Wang and co-authors did a series of comprehensive studies and developed several correlations. Of these, Wang *et al.* (2002) reported the single most promising correlation.

Fin temperatures of finned coil heat exchangers under evaporating conditions are often below the dew point temperature of the incoming air. As a result, not only heat transfer but also mass transfer takes place from the humid air (dehumidification) and have a very large influence on heat exchanger performance (Pirompugd *et al.*, 2007). The modelling of the very complex effects of condensation can be realised by employing the heat and mass transfer analogy (based on the Lewis number) in combination with a suitable heat transfer correlation.

Available flow boiling correlations are inaccurate when applied to CO_2 because of the previously mentioned unique thermo-physical properties especially its very low surface tension (Austin & Sumathy, 2011). This is arguably the most influential parameter in two-phase flow phenomena.

Various authors have made attempts in recent years to develop correlations specific to CO_2 flow boiling. The Hwang *et al.*, 1997 modified Bennett-Chen correlation as well as Cheng *et al.* (2008a&b) have shown general use in the simulation of CO_2 finned coil evaporators for both heat transfer as well as pressure drop.

In 2010, a vapour compression CO_2 heat pump test bench was built at the North-West University (NWU). It consisted of two CO_2-water concentric tube heat exchangers, a compressor and an electronic expansion valve. In 2011, a large-scale upgrade was done. The instrumentation went from only the most essential and very basic to where higher-level research could be accommodated. This included research on the accuracy of correlations regarding the flow boiling, as well as gas cooling, heat transfer and pressure drop characteristics of CO_2 as a refrigerant.

Since energy concerns in South Africa are at an all time high; CO_2 - water heaters, with air as the heat source, are gaining more focus as a green, environmentally friendly, and efficient replacement to conventional electric water heaters. Thus, research on these systems is of great interest to energy suppliers and equipment manufacturers.

1.2. Problem Statement

The design of efficient finned coil heat exchangers entails the use of simulation models. The accuracy of these models is very dependent on the heat transfer and pressure drop correlations that they use. Since CO_2 has some unique properties, the past few years have seen the development of new correlations. Most existing simulation models still use conventional correlations for general use and are inadequate when applied to CO_2. Thus, the development of an evaporator simulation model, exclusively for CO_2 finned coil evaporators, which can be later on integrated into a heat pump cycle simulation, are of great value.

1.3. Aims of this study

The aims of this study are to:

- Conduct a literature survey into existing heat transfer and pressure drop correlations for CO_2 and air as well as previous simulation studies.
- Upgrade the existing CO_2 heat pump test bench at the NWU to include an air-to-CO_2 finned coil evaporator along with additional instrumentation.

- Develop a simulation model of the finned coil evaporator upgrade, to characterize and predict its performance.
- Use the test bench and the commercial software package, EVAP-COND (NIST, 2003), to evaluate the performance of the simulation model.

1.4. Research Methodology

The following methodology is followed in order to achieve the above mentioned aims.

Conduct an in depth literature survey.

The literature survey will focus on the following main topics:

- A survey of available literature on moist air heat and mass transfer correlations, as well as pressure drop correlations will be conducted. Correlations for typical finned coil heat exchangers under dehumidifying conditions will be evaluated in terms of their geometric limitation. The geometric parameters and their effect on airside heat transfer and pressure drop that make CO_2 finned coil heat exchangers different from other finned coil heat exchangers will also be investigated. From this, appropriate correlations for the airside heat transfer and pressure drop will then be selected.
- The literature survey will also include proposed CO_2 flow boiling heat transfer and pressure drop correlations and an evaluation on their applicability. The most applicable correlation for CO_2 will then be selected.
- The modelling of finned coil heat exchangers can vary in complexity. The study will also consider different modelling techniques and strategies to adequately simulate the finned coil heat exchanger. Attributes such as the inclusion of tube-to-tube heat transfer, tube-axial heat transfer, transient or steady-state, multiple refrigerant circuitries, discretisation, collar resistances, dry, partially wet, fully wet as well as discontinuous two-phase flow patterns and homogeneous or separated flow models will be considered.
- Similar studies from the literature will be summarised to establish the trend in simulation of finned coil evaporators as well as the usage of correlations, assumptions and validations.
- Since heat pump systems include a compressor, lubricant is used to ensure the safe operation and longevity of the compressor. This lubricant may have an impact on CO_2 heat transfer and pressure drop characteristics and will therefore be investigated in the literature survey.

Upgrade the existing CO_2 heat pump test bench at the NWU.

The test bench at the NWU is currently equipped with a concentric tube water-to-CO_2 evaporator. The upgrade will consist of the design and procurement of a finned coil heat exchanger with a staggered, macro tube arrangement for possible dehumidification. It will be installed in parallel with the existing evaporator. The upgrade will enable experimental testing using either the concentric tube or the finned coil heat exchanger as evaporator component. In addition, an instrumentation upgrade to accommodate the present study will be done. This will include temperature and pressure sensors throughout a single circuit.

Develop a simulation model to predict the performance and characteristics of the finned coil evaporator.

In order to predict the performance characteristics of the wavy finned coil heat exchanger with a staggered, macro tube arrangement with possible dehumidification, a detailed simulation model will be developed. This model will use the most applicable and accurate correlations selected from literature.

Because of the very large variations in thermodynamic properties encountered in the flow boiling of CO_2, the simulation model will implement a discretisation scheme. This will ensure the adequate modelling and capture of the crossover regions between the various flow patterns.

In the discretised simulation of heat exchangers, large sets of equations must be solved simultaneously. Thus Engineering Equation Solver (EES) (Klein & Alvarado, 2012), will be used to simulate the finned coil heat exchanger.

Conduct experimental testing to generate data.

By operating the upgraded test bench at different conditions, experimental data will be generated. This data will include mass flow, temperatures and pressures of CO_2 throughout, as well as air relative humidity, velocity, temperatures and pressures before and after the finned coil.

Verify the simulation model with EVAP-COND.

By simulating the finned coil in the commercially available software package, EVAP-COND (NIST, 2003), the CO_2 temperature, pressure and vapour quality at each bend can be extracted. The sensible and latent heat transfer rates for each tube as well as the air dry-bulb temperature and relative humidity for each circuit are also available. The comparison of this data to the simulation model predictions will enable the verification the model.

Validate the simulation model with experimental data.

The experimental data obtained from the test bench, will be compared to the simulation model predictions in order to validate the model.

CHAPTER 2:
Literature Survey

This chapter serves as a review of applicable literature, to gain better insight into the airflow phenomena and effects of certain geometric parameters. The main topics of the literature survey are as follows:

- The history of CO_2 being used as a refrigerant.
- CO_2 heat transfer and pressure drop correlations.
- Airflow through fins and dehumidification.
- Air heat transfer and pressure drop correlations.
- Simulation strategies.
- Previous simulation studies.
- Compressor lubricants.

2.1. History of CO_2 as refrigerant

Dr. James Black, who was promoted to professor of chemistry at Glasgow University in 1755, discovered carbon dioxide in an experiment heating magnesium carbonate. It was later proven that this so-called “fixed air” is readily available and forms part of many common processes. Black had no thermodynamic or refrigeration interest and had done no further research in these fields (Pearson, 2005).

Almost a century later, the fundamentals of phase change, studied during the 1600s and 1700s, enabled inventors such as Oliver Evans, Jacob Perkins and Richard Trevithick to propose designs for refrigeration systems. Perkins was the first to build a vapour-compression system, which he also patented in 1834 (Calm, 2008). It used ethyl ether as refrigerant. His patent described a refrigerant essentially as a volatile fluid that was evaporated and condensed without waste. Thus, any “volatile fluid” that worked, and was available, qualified. Among these were ammonia, propane (which was advertised as the “safety refrigerant” over ammonia), various ethers, water, carbon dioxide, sulphur dioxide (SO2) and hydrocarbons (HC). Each of these refrigerants had some type of hazard. For instance naphtha (HC), Chemogene (mixture of petrol ether and naphtha) and chloromethane are highly flammable while ammonia and sulphur dioxide are very toxic. Carbon dioxide requires high-pressure equipment (Pearson, 2005) and all other ether-based substances are both flammable and toxic.

In 1930, Midgely & Henne published that the chlorination and fluorination of hydrocarbons altered their boiling point, flammability and toxicity (Calm, 2008). This enabled chemists to control not only the boiling point, which is a critical refrigerant selection parameter, but also the flammability and toxicity of the above mentioned substances. These CFCs and HCFCs dominated during the start of residential small air conditioning and heat pump systems (Calm, 2008).

CFCs were linked to stratospheric ozone depletion in 1974 by Frank Sherwood Rowland and Mario J. Molina (Molina & Rowland, 1974). Figure 2 illustrates the chemical reaction.

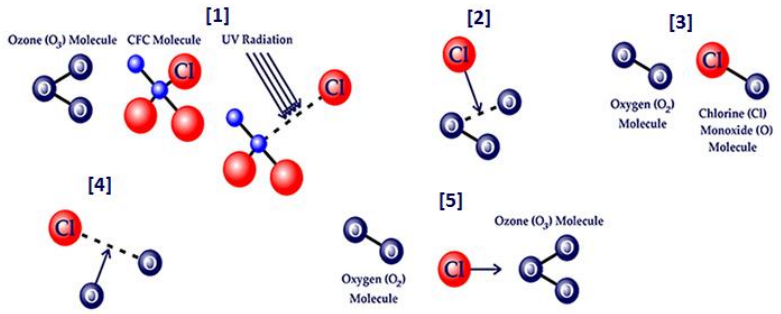

Figure 2: Illustration of ozone depletion reactions (Molina & Rowland, 1974).

The chlorine atom, in a typical CFC molecule, is dissociated by Ultra violet radiation [1]. The double covalent bonds between two oxygen atoms are overcome [2], and the chlorine atom bonds with one of the oxygen atoms to form a chlorine monoxide (ClO) molecule [3]. A free oxygen atom from the atmosphere then, again, breaks up the chlorine monoxide molecule [4] to form oxygen and free the chlorine atom, which is able to break up a new ozone molecule [5]. Thus, the chlorine atom is separated from the CFC molecule by UV radiation and reduces ozone to oxygen.

Initiating from the Vienna convention in 1987, the Montreal protocol (United Nations, 1987) has been effective since 1 January 1989. It stated that the production and use of CFC and HCFC refrigerants must be slowly decreased and ultimately eliminated, although existing equipment service is still allowed.

Global warming became a recognized crisis in August 1990, when the Intergovernmental Panel on Climate Change (IPCC) published their first assessment report. The report stated that human activities contribute significantly to global warming and that immediate action to reduce emissions of so-called greenhouse gasses must be taken. This report sparked the United Nations general assembly (in November 1990) to create a climate convention for signing at the Rio de Janeiro Earth summit in June 1992. The USA (who is also the biggest emitter) had refused to sign the agreement, claiming scientific uncertainties and unacceptable economic consequences. This led to the United Nations Framework Convention on Climate Change (UNFCCC) (Hare, 1998).

With the first Conference Of the Parties (COP 1) in March and April 1995, it was clear that industrialized countries showed little support and consequently the Berlin mandate was formed which ultimately lead to the legally binding Kyoto protocol to the UNFCCC on 11 December 1997 (Hare, 1998). With COP 6 in Bonn July 2001 and COP 7 in Marrakech November 2001, new softened emission targets were set for 2010.

The protocol identified the following as Greenhouse gasses: carbon dioxide, methane, nitrous oxide, hydro fluorocarbons, per fluorocarbons and sulphur hexafluoride (United Nations, 1998).

Only with the discovery of chlorofluorocarbons being responsible for stratospheric ozone depletion and the global warming potential of all fluorocarbons, have research been renewed and focus shifted back to natural refrigerants such as water, air, ammonia, propane and carbon dioxide.

Of these four candidates, carbon dioxide is a promising natural refrigerant because of its unique thermo-physical properties that enable high heat transfer coefficients and low pressure drops (Zhao & Bansal, 2009).

2.2. CO_2 properties

Carbon dioxide is a very attractive candidate as a natural refrigerant as discussed in Chapter 1 and shown in Table 1. It is widely available in large quantities, inexpensive and can be recaptured for reuse. A sub-critical CO_2 cycle (thus all cycle temperatures are below the critical temperature of

31.1°C) cannot reject heat at high temperatures. Hence, the use of a trans-critical cycle is justified. This means that gas cooler temperatures are higher than 31.1°C, and thus the rejection of heat above the critical point is possible. Some prominent properties, specific to heat transfer characteristics and heat exchanger design, is reproduced from Pettersen *et al.* (1998) in Table 2.

Table 2: Some properties of CO_2 compared with HCFC-22 and HFC-134a.

	HCFC-22*	HFC-134A*	CO_2*
Liquid thermal conductivity [$w/(m \cdot k)$]	0.099	0.092	0.111
Liquid kinematic viscosity [mm^2/s]	0.2	0.21	0.11
Liquid specific heat [$J/(kg \cdot K)$]	1180	1340	2430
Vapour density [kg/m^3]	21.5	14.4	97.6
Liquid density [kg/m^3]	1285	1293.5	926.4
Density ratio [-]	59.8	89.8	9.5
Surface tension [mN/m]	13.1	11.2	4.6

**These properties correspond to the saturated state at 0 ºC of the respective refrigerants.*

HCFC-22: Chlorodifluoromethane (Freon-22) ***HFC-134A:*** *1,1,1,2-Tetrafluoroethane* ***CO_2:*** *Carbon dioxide*

Pettersen *et al.* (1998) reported that the combination of high liquid thermal conductivity, high liquid specific heat and low kinematic viscosity leads to superior heat transfer characteristics. This can be attributed to higher Reynolds and Prandtl numbers at constant geometry and flow velocity. Experimental investigation has shown that surface tension is arguably the most important factor influencing heat transfer characteristics. However, it is not always included in correlations, which contribute to their inaccuracy, for example those of Shah, 1982, Gungor & Winterton, 1987 and Steiner & Ozawa, 1983. The very low value for CO_2 greatly promotes a lower friction factor, and in turn, smaller temperature glides. Lower liquid density also contributes to reducing the friction factor while higher vapour density will enhance heat transfer in the dryout region.

The relatively high vapour densities contribute to a higher volumetric heating capacity (Robinson & Groll, 1998). As a result, less refrigerant charge is needed, and heat exchanger components can be smaller and more compact. As CO_2 trans-critical systems operate at high pressures of typically 80 to 110Bar, smaller components can handle the high pressure much better while retaining good heat transfer.

2.3. CO_2 correlations

Because of the already mentioned unique thermo-physical properties of CO_2, flow boiling regimes and regime changes differ largely from conventional refrigerants. Common correlations generally under predict heat transfer and over predict pressure drop. Mastrullo *et al.* (2010) contributed this to the fact that most correlations are developed from experimental data at ordinary temperatures with fluids that has low reduced pressures. Various researchers have conducted studies on flow boiling phenomena inside tubes.

In 1997, Bredesen *et al.* measured heat transfer coefficients in 7mm inner diameter tubes while varying heat flux, mass flux and saturation temperature. They found that in the low-quality region, heat transfer increased with heat flux. Hwang *et al.*, 1997 tested six already used correlations for their applicability to CO_2 flow boiling, based on the Bredesen *et al.*, 1997 data. They went on to modify the vertical tube Bennett & Chen correlation with good results (Yun *et al.*, 2003).

Also in 1997, Knudsen & Jensen measured flow boiling data in a 10.06mm inner diameter tube and ultimately applied a 1.9 multiplier factor to the Shah, 1982 correlation to fit their data. Using a large set of 404 data points, Thome & Hajal (2004) developed a correlation that can predict 86% of the data to within ±30%. Their correlation was an update of the Kattan-Thome-Favrat correlation which is based on a phenomenological approach. Thus various flow regimes are characterised and modelled

seperately. Cheng *et al.* (2006) further developed the correlations of Thome & Hajal (2004) and Wojtan *et al.* (2005) which were then expanded to cover larger ranges, by Cheng *et al.* (2008a&b). The applicable ranges of some correlations are given in Table 3.

Table 3: Flow boiling heat transfer correlation ranges.

	Tube D_i $[mm]$	Mass flux $[kg/m^2]$	Heat flux $[W/m^2]$	Saturation temperature [℃]
Knudsen & Jensen, 1997	10.06	85 to 175	7 to 13	-25 to 10
Hwang *et al.*, 1997	7	200 to 400	3 to 9	-25 to 5
Yun *et al.*, 2001	6	170 to 320	10 to 20	5, 10
Yoon *et al.*, 2004	7.53	200 to 530	12 to 20	-4 to 20
Thome & Hajal (2004)	0.79 to 10.06	85 to 1440	5 to 36	-25 to 25
Cheng *et al.* (2006)	0.8 to 10	170 to 570	5 to 32	-28 to 25
Cheng *et al.* (2008a&b)	0.6 to 10	50 to 1500	1.8 to 46	-28 to 25

2.4. Airflow and dehumidification

As air flows through wavy fins, it follows the wave pattern depending on parameters such as flow velocity, fin pitch, wave angle and wave height. The airflow also splits around the tubes where parameters such as number of tube rows and collar diameter play an important role. It is clear that heat transfer is very difficult to describe for wavy fin heat exchangers. Over the years a lot of experimental research has been done on the heat transfer of wavy finned coil heat exchangers such as, Bourabaa *et al.* (2011), Chen & Wang (2008), Gray & Webb (1986), Kim *et al.* (1999), Pirompugd *et al.* (2007), Kuvannarat *et al.* (2006) and Wang *et al.* (2002).

Tao *et al.* (2007) did a three-dimensional numerical simulation study on local heat transfer and friction characteristics. They found that heat transfer is very low at the inlet of the fins but increases as the first wave apex approaches. After the apex, heat transfer drops dramatically and then more slowly as the wave trough is reached. The observation of a repetitive pattern in heat transfer for every wave apex and trough becomes clear. The pattern was attributed to the wave apex breaking up the thermal boundary layer, flow separation occurring just behind the apex and reverse flow occurring in the wave trough.

Figure 3 is reproduced from Tao *et al.* (2007) and shows the local Nusselt number rise and fall, which is proportional to the local heat transfer coefficient. The horizontal axes represent a non-dimensional length in the airflow direction.

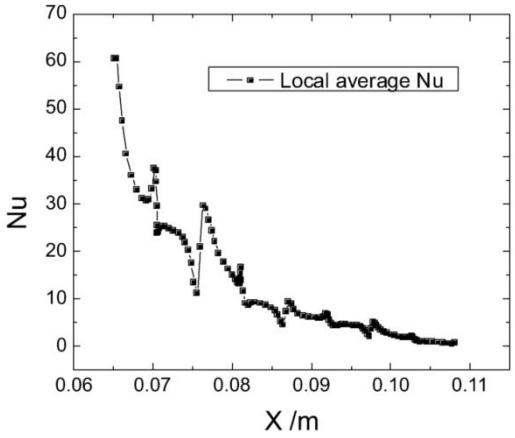

Figure 3: Local variations in average Nusselt number in the airflow direction (Tao *et al.*, 2007).

A recirculation zone also forms behind the tubes which contribute to a decreasing effect on heat transfer; however, depending on factors such as fin pitch and Reynolds number, vortices are shed from this recirculation zone that promotes airflow mixing and enhances heat transfer.

2.4.1. Dehumidification

Fin temperature falling below the dew point temperature of the oncoming humid air is a phenomenon commonly found in finned coil evaporators. Condensation of water vapour in the airflow to liquid on the finned tube surface occurs in the form of a film or droplet, mostly dependent on airflow velocity. This phenomenon greatly influences the airside performance and further adds to the complexity of airflow and airside heat transfer.

Wet surface

The formation of condensate on the fin surfaces, not only increases the friction factor, but also alters heat transfer characteristics. Hydrophilic coatings are sometimes used to promote water condensate drainage and inhibit corrosion, while reductions in pressure drop of 20% to 50% have been reported (Ma *et al.*, 2009). The form in which condensation takes place have a significant influence on the overall condensation effect and can be described as drop wise or film wise condensation.

When drop-wise condensation forms, it can act as a roughening element and vortex generator. If bridging occurs (usually with smaller fin pitches), it is possible that the airflow twists and local air velocity increases, resulting in a drastic increase in heat transfer. Droplets can also cause swirling vortices that can enter the main flow stream to increase mixing and consequently heat transfer (Kuvannarat *et al.*, 2006) as seen in Figure 4.

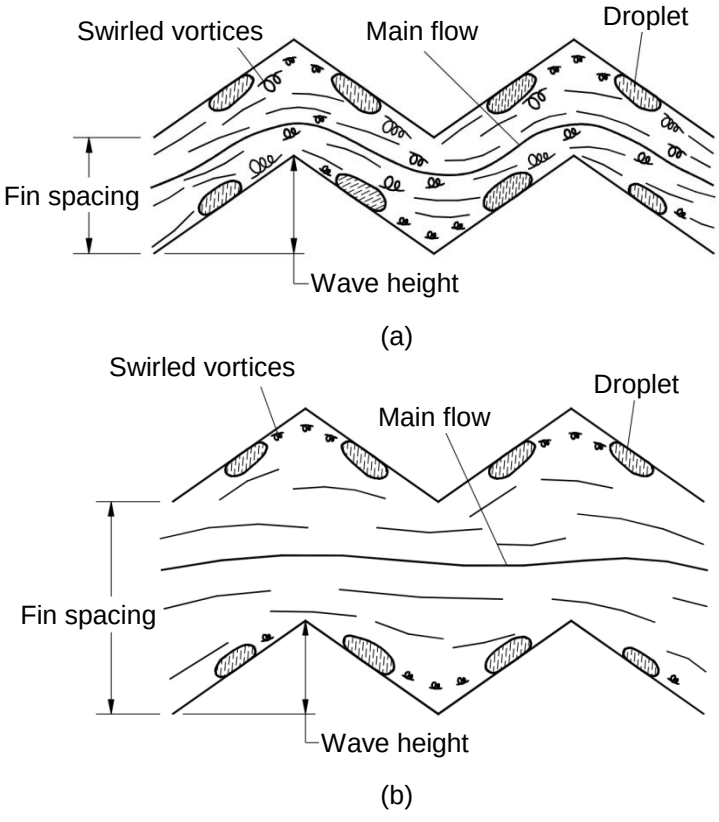

Figure 4: Schematic reproduced from Kuvannarat *et al.* (2006) showing the interaction between directed and swirled flow for small and large fin spacing (a) Small fin spacing (b) Large fin spacing.

Film wise condensation can decrease heat transfer as an additional thermal conductivity resistance through the water film adds to the overall heat transfer resistance. In addition, the pressure drop is

increased. Because of the wavy geometry, film wise condensation is very rare in wavy finned coil heat exchangers.

Partially wet surface

When the fin tip temperature is above the dew point temperature but the fin base, or tube, temperature is below it, partial condensation occurs and a partially wet surface prevails. Only those parts of the surface that is below the dew point temperature will cause dehumidification and condensation (Huzayyin *et al.*, 2007).

Mirth & Ramadhyani (1994) concluded early on that the partially and fully wet condition for finned coil heat exchangers is not yet fully understood; seeing that no conclusive evidence could be gathered from the literature.

As mentioned in Chapter 1, the evaporator for the present study will be discretised into separate elements. The simulation model handles these elements as either fully dry or fully wet, as discussed later in Chapter 4.

2.4.2.Geometric parameter effects

The present study entails the simulation of a wavy finned coil heat exchanger, with a staggered macro tube arrangement, and possible dehumidification. The focus of this section includes geometric parameters, and gives some indication of the expected influence of different geometric parameters on the heat transfer and pressure drop in the present study.

Fin type

Wang *et al.* (1997) reported that a wavy fin configuration increases heat transfer by approximately 55% to 70% from plain fins, while an increase of 66% to 140% in friction factor was observed. This increase in heat transfer leads to better flow mixing between the fins, a longer fin path in the airflow direction and consequently a larger surface area to accommodate heat transfer. It is evident that at higher air inlet velocities, wavy fin geometry will be more suitable than plain flat fins.

Fin pitch

It has been reported that at a constant Reynolds number, fin pitch has no significant impact on heat transfer coefficient. A simultaneous increasing and decreasing heat transfer phenomenon transpires. For an increase in fin pitch, better air mixing occurs, but the recirculation zone downstream of the wave apexes also increases, reducing heat transfer (Wongwises & Chokeman, 2005). Wang *et al.* (1997) also reported these findings.

However, some literature revealed that under dehumidifying conditions and for Reynolds numbers below 3000, an increase in fin pitch relates to a decrease in heat transfer performance (Pirompugd *et al.*, 2006). A probable cause is bridging of water condensate droplets on the outer surface. At smaller fin pitches and low Reynolds numbers, the vortex regions behind the tubes are eliminated to form a steady laminar flow and may contribute to the observed effect. While there is no effect on friction factor at low Reynolds number, at numbers over 2500 the friction factor shows a decrease with increase in fin pitch and vice versa (Wongwises & Chokeman, 2005).

Number of tube rows

Heat transfer and friction factors tend to decrease with increasing number of tube rows from 2 to 6 at Reynolds number below 4000. This is because at these low Reynolds numbers, vortices form behind the tubes and the downstream turbulence is small (Wongwises & Chokeman, 2005, Tao *et al.*, 2007). At Reynolds numbers above 4000, there is no influence on the friction factor (Wang *et al.*, 1997), however, because downstream eddies (shed from the tube cylinder in a staggered tube arrangement)

cause good mixing, an increase in heat transfer with increase in number of tube rows occurs. Contrary to this, for an inline tube arrangement, above a Reynolds number of 4000, tube row number has no influence on heat transfer. This is because at higher Reynolds number, the wavy pattern determines the airflow and breaks up the boundary layer at each wave apex (Wang *et al.*, 1997).

Fin thickness

In dry conditions, the heat transfer and friction factors do change when the fin thickness is varied from 0.115mm to 0.25mm (Wongwises & Chokeman, 2005). It has been reported that for tube rows equal to two and a fin pitch equal to 1.41mm, thicker fins increase heat transfer and friction factor while for larger fin pitches and number of tube rows the effect diminishes and is ultimately eliminated (Kuvannarat *et al.*, 2006). For small fin pitches, an increase in heat transfer with wave height is obtained (Pirompugd *et al.*, 2006). Tao *et al.* (2007) showed that an increase in wave angle increased the heat transfer performance and the friction factor.

The conduction resistance between fin and tube is determined by the manufacturing technique, whether it was chemically bonded, welded, brazed or mechanically extruded. Depending on these manufacturing techniques, the contact resistance in a typical finned coil can comprise between 2% and 7% of the total thermal resistance.

Larger diameter tubes directly increase the pressure drop, as a larger "obstacle" has to be passed. The only increase in heat transfer is due to better drainage of condensate on the fin surfaces (Wang & Liaw, 2012). Studies have shown that while keeping all other parameters constant, generally an increase in Reynolds number will produce an increase in heat transfer and a decrease in friction factor (Tao *et al.*, 2007). Friction factor and heat transfer usually increase with condensation as reported by Mirth & Ramadhyani (1994).

It is clear that because of the complexity of airflow, the experimental determination of the effects of variations in these parameters is very difficult to obtain. As some agreements are established, contradicting results still appear. This may be caused by the multitude of factors and parameters that have an influence. Difficulty in separating these parameters individually and systematically determining their effects, has led to inconclusive results. Table 4 is set up to summarise the effects of certain parameters as best found in agreeing literature, where a "+" indicates an increase and a "-" a decrease.

Table 4: The effect of an increase in some geometric parameters on heat transfer and pressure drop.

Parameter increase	Effect at Reynolds number below transition		Transition Reynolds number		Effect at Reynolds number above transition	
	Heat transfer	Friction factor	Heat transfer	Friction factor	Heat transfer	Friction factor
Fin pitch	-[d]	*ne*	3000[d]	2500	*ne*	-
Number of tube rows	-	-	4000	4000	+	*ne*
Fin thickness[c]	+	+	*n*	*n*	+	+
Wave height	+	*nr*	*n*	*n*	+	*nr*
Wave angle	+	+	*n*	*n*	+	+
Tube diameter	+[d]	+	*n*	*n*	+[d]	+
Reynolds number	+	-	*n*	*n*	+	-
Wet surface	-[c]	+	*n*	*n*	+[c]	+

[d] *- Indicates that the effect is only observed in dehumidifying conditions.*
[c] *- Subject to specific conditions; see heading.*
ne – No or negligible effect has been observed.
nr – No report on effect.
n – No transition Reynolds number.

2.5. Airside correlations

This section gives a summary of the most influential work on wavy finned tube air heat transfer and friction factor correlations, where different secondary fluids and techniques were used to correlate the airside data.

Yoshii, 1972 did some of the first experimental studies on wavy finned coil heat exchangers. They presented dry Nusselt number data for two eight-row staggered, and inline tube coils. Yoshii *et al*., 1973 conducted experiments on wet surface heat exchange with a two-row staggered tube arrangement (Mirth & Ramadhyani, 1994).

Beecher & Fagan, 1987 tested the effects of fin pattern on the heat transfer performance of the airside, and produced data for 21 wavy finned and seven plain-finned three-row staggered tube heat exchangers. They used imbedded sensors to measure the fin surface temperature. In addition, an electrical heating method kept the fins at a constant temperature.

Webb, 1990 correlated Beecher & Fagan's data, but Wang *et al.* (1997) reported that their technique assumed a fin efficiency of 100% and that there is no contact resistance between the fin and tube. These conditions can only be approached but are close to impossible to fully achieve in a practical commercial heat exchanger.

Mirth & Ramadhyani (1994) were the first to speculate that a systematic error was also present in Beecher & Fagan's data that caused higher Nusselt numbers. Mirth and Ramadhyani then went on to develop their own Nusselt number and friction factor correlations (Wang *et al.*, 1997). They used experimental data from five commercially manufactured heat exchangers with tube rows of 4 to 8, large outer tube diameters of 13.2mm to 16.4mm and large longitudinal and transverse pitches of 31.8mm to 38.5mm. Their dry surface correlation was able to predict 20% of the broader data gathered from literature. A friction factor correlation for wet surfaces was also developed (Mirth & Ramadhyani, 1994).

Kim *et al.*, 1997 correlated the results from both Beecher & Fagan, 1987 and Wang *et al.* (1997) where 92% of the heat transfer data were within ±10% and 91% of the friction data within ±15%. It was reported that the Webb, 1990 and the Kim *et al.* 1997 correlations generally over predicted the data. As already mentioned, possible errors in the Beecher & Fagan data source may be the cause. The following aspects were pointed out:

- Contact resistance between fin and tube that did not appear in the data.
- The contact resistance is usually absorbed in the airside resistance.
- Constant temperature approach assumed 100% fin efficiency.
- Arithmetic mean temperature difference (AMTD) rather than conventional log mean temperature difference (LMTD) or ε-NTU approach.
- An unclear derivation in connection with the LMTD approach.
- Very high corrugation angles.

Wang *et al.* (1997) proposed a correlation that includes a two row staggered tube arrangement, using more commercially available heat exchangers and experimental techniques that are more viable. Wang *et al.*, 1999b developed a correlation for larger tube outer diameters (12.7mm and 15.88mm before expansion), while Wang *et al.*, 1999c developed a correlation for smaller tube outer diameters (7.94mm and 9.53mm before expansion). It is not recommended by the authors to extrapolate these data for other geometric ranges as inappropriate results will be obtained.

In order to develop a correlation with broad ranges, Wang *et al.* (2002) tested 16 wavy fin heat exchangers and also included data from another 45 samples produced by Wang *et al.*, 1998, Wang *et al.*, 1999a, Wang *et al.*, 1999b and Wang *et al.*, 1999c. The correlation was able to predict 91% of the heat transfer data within 15% while 85% of the pressure drop data were predicted to within 15%.

These studies used the data reduction method proposed by Wang *et al.* (2000b). Table 5 is a reproduction from Wang *et al.* (2002) and shows the applicable ranges of the above mentioned correlations.

Table 5: Geometrical ranges of some airside heat transfer and friction factor correlations (Wang *et al.*, 2002).

	Samples	Re_{Dc} [-]	$D_c\ [mm]$	$P_t\ [mm]$	$P_l\ [mm]$	$F_s\ [mm]$	N
Webb, 1990	20	2000-9000	9.53-12.7	25.4-31.3	22-27.5	2.08-4.22	3
Kim *et al.*, 1997	32	500-6000	9.53-12.7	25.4-31.3	22-27.5	2.08-4.22	1-4
Wang *et al.*, 1999c	18	500-10000	13.6-16.85	31.75-38.1	27.5-33	2.98-6.43	1-6
Wang *et al.*, 1999d	27	300-8000	8.58-10.38	25.4	19.05-25.4	1.21-3.66	1-6
Wang *et al.* (2002)	61	300-10000	7.66-16.85	21-38.1	12.7-33	1.21-6.43	1-6

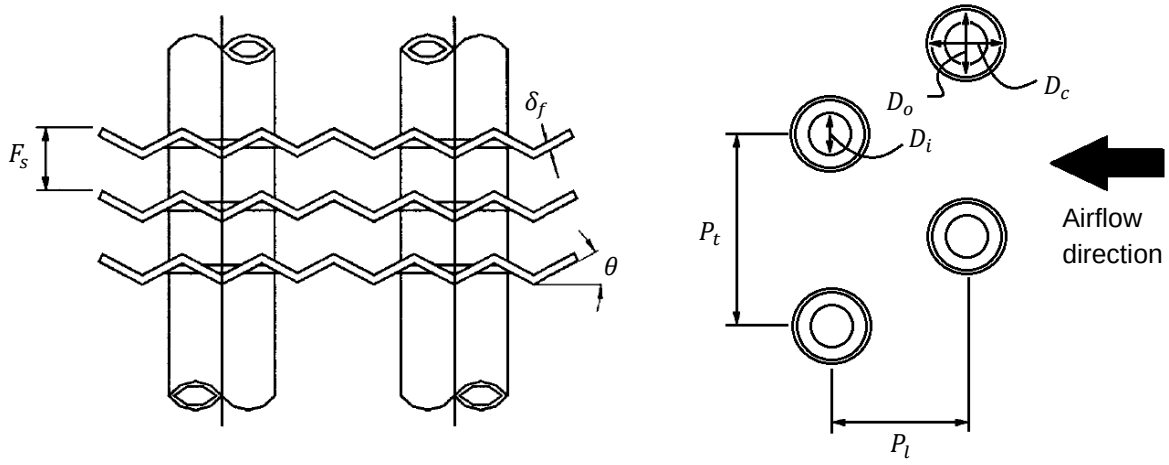

Figure 5: Basic geometric dimensions of a wavy finned coil heat exchanger partly reproduced from Wang *et al.* (2002).

All the correlations in the table above were derived from dry surface conditions. Literature with regard to wet and partially wet surface conditions on wavy fin and tube heat exchangers are rare. Kuvannarat *et al.* (2006) developed a correlation from 10 tested samples. The majority of which had only two tube rows and a collar diameter of between 9.76mm and 10.03mm, P_t equal to 25.4mm, P_l equal to 19.05mm, F_s between 1.41mm and 2.54mm, and δ_f between 0.115mm and 0.25mm. Thus, their correlation has a very limited range of applicability.

Usually little attention is given to mass transfer correlations because the heat and mass transfer analogy would enable the calculation of the mass transfer coefficient providing that an appropriate heat transfer correlation can be used. The heat and mass transfer analogy exists because the mechanisms and physical laws describing these two types of energy transfer are similar. However, Pirompugd *et al.* (2006) did develop a heat and mass transfer correlation from eighteen sample heat exchangers.

2.6. Correlation accuracy

The correlations discussed above are typically constructed by experimentally determining the effects of various parameters, converting them into non-dimensional entities, including them in the proposed equations and finally fitting a curve through the data. These steps are repeated to obtain the lowest least squares fit.

From various studies, it is clear that most correlations can only accurately predict the data, on which they are based, with the exception of successfully generalized correlations such as Dittus-Boelter (Incropera *et al.*, 2007). Because of the inconsistency and controversy in the techniques used to

develop these correlations, the correlations used in the present study must have base data strongly resembling that of the finned coil evaporator to be simulated. Thus, the ranges of geometric and thermodynamic parameters of the applicable correlations (Cheng *et al.*, 2008a&b, Wang *et al.*, 2002) must closely match those of the heat exchanger and heat pump test bench.

2.7. Simulation strategies

This section outlines various finned coil simulation strategies studied from literature. Some strategies are more complex while others are more accurate. These are:

- Lumped model (Dazhang *et al.*, 2009).
- Tube-by-tube (Domanski, 1999).
- Fundamental discretised elements (Bendaoud *et al.*, 2010).
- Nodes and elements (Oliet *et al.*, 2010).
- Resistance model (Singh *et al.*, 2008).
- Detailed model of moisture on fin and tube surfaces (Khudheyer, 2011).

The present study involves the simulation of an evaporator, where the refrigerant flowing on the inside is characterised by different flow regimes. Hence, simulation strategies such as the lumped and resistance models are inadequate. The tube-by-tube and fundamental discretised elements model are the most applicable to capture the different flow regimes. Of these, the fundamental discretised elements model is the more accurate strategy.

The nodes and elements model, such as that implemented by Oliet *et al.* (2010), and the detailed model of moisture on fin and tube surfaces, is developed to accurately model the outer surface temperature distributions. This requires heavy computer power and is not familiar to the author. Since the present study only requires the prediction of dehumidification, the fundamental discretised modelling of both fully wet and fully dry elements would suffice.

Researchers such as Aidoun & Ouzzane (2009) and Jiang *et al.* (2006) use a so-called junction tube connectivity matrix in order to define the tube connectivity and circuitry, which gives a more generic attribute. However, since the present study only defines the simulation of one finned coil (the test bench upgrade), this type of circuitry matrix will not be implemented.

2.8. Previous finned coil simulation studies

A short summary of a number of studies that contain a simulation of a CO_2 plate finned coil evaporator is given. Only the relevant literature regarding this component is summarised. Important aspects such as choice of correlation, modelling strategy, uncertainty analysis and assumptions are the focus.

2.8.1. Study by Robinson & Groll (1998)

In order to determine if a CO_2 finned coil heat exchanger can be made smaller than an R-22 finned coil heat exchanger, used in car air-conditioning applications, four computer models were developed in EES (Klein & Alvarado, 2012). This included a condenser and evaporator model for R-22, as well as a gas cooler and evaporator model for CO_2. The homogeneous CO_2 evaporator model was simplified by considering a discretised single finned tube with plain flat fins. The authors made the following simplifying assumptions:

- Negligible changes in potential energy.
- Steady state operation.
- Vapour saturation is reached.
- No temperature profile in airflow direction.
- Adiabatic fin edges.
- Two-phase transport properties were evaluated at a constant temperature.

- Fully wet (dehumidification).

In contrast to the study to be discussed in 2.8.5 by Bendaoud *et al.* (2010), the CO_2 evaporator was simulated at more applicable conditions with regard to the present simulation. The air inlet temperature was set at 22°C and relative humidity at 50%. An evaporating temperature of 0°C at 34.85Bar and a constant air velocity of 2m/s were implemented (Robinson & Groll, 1998).

Robinson & Groll, used the Hwang *et al.*, 1997 modified Bennett-Chen correlation to calculate the two-phase CO_2 heat transfer coefficient and for the single-phase, Petukhov, Kirillov and Popov's equation was applied as described by Incropera & DeWitt, 1990.

To calculate the two-phase CO_2 pressure drop, the modified Martinelli-Nelson correlation, as reported by Jung & Radermacher, 1989, was used; and also the method described by Incropera & DeWitt, 1990 for single-phase turbulent flow.

The airside heat transfer coefficient was calculated for laminar parallel flow over a flat plate and for cross flow over a cylinder, as given by Incropera & DeWitt, 1990. These calculated values were then weighted before the thermal resistances were multiplied by effective air-water vapour specific heats, as shown by Braun *et al.*, 1989, to account for wetted surfaces.

By varying the fin lengths, it is reported that a heat exchanger with a larger outside heat transfer area due to smaller outside tube diameters can be built, that is 27% lighter and takes up 29% to 40% less volume. Thus, CO_2 is the better refrigerant for car air-conditioning applications because of its unique thermo-physical properties.

2.8.2. Study by Domanski (1999)

A finned coil model was developed and the National Institute of Standards and Technology (NIST) produced the software EVAP-COND (NIST, 2003), which can be used to simulate finned coil evaporators as well as condensers. This software can be used to simulate and predict CO_2 evaporator performance but was not designed specifically for CO_2 evaporation. Although the model was verified using R-22, no conclusion could be drawn to the accuracy when applied to CO_2 (Domanski, 1999).

The software calculates the single-phase heat transfer coefficients according to McAdams ASHRAE, 1993 and for two-phase, up to a vapour quality value of 0.8; the software uses the correlation by Jung & Didion, 1989. Linear extrapolation obtains the coefficients for qualities of 0.8 to 1. An updated version later added the correlation by Thome, 2005. The single-phase CO_2 pressure drop was calculated according to Petukhov's correlation and two-phase according to the Pierre correlation. The heat transfer coefficients on the airside were calculated using Webb, 1990. Again, an updated version included the correlations by C.C. Wang from 1999 to 2001.

2.8.3. Study by Ouzzane & Aidoun (2008)

A simulation model was created for a wavy finned tube CO_2 evaporator under wet and partially wet conditions. The output of which was the outlet pressure and temperature for CO_2 as well as that of air; and heat exchanger capacity. It uses fluid property information from the NIST-REFPROP database. The homogeneous simulation model implements the following assumptions:

- Steady state operation.
- Both air and CO_2 flows are one-dimensional.
- Uniform airflow across the coil.
- Negligible heat loss to the environment.
- No frost.

To calculate the airside heat transfer and pressure drop, the correlation of Wang *et al.* (2002) was used. For two-phase CO_2 flow, the Hwang *et al.*, 1997 modified Bennett-Chen correlation was used for both heat transfer and pressure drop, while the formulation of Geary was used for pressure loss in return bends.

The model was validated with experimental data, manufacturer's data, and data found in open literature. Good heat transfer agreement was reported, although airside pressure drop showed only fair agreement. The accuracy of the friction factor correlation was deemed the cause.

2.8.4. Study by Dazhang *et al.* (2009)

In this study, a steady state lumped model was created to simulate a finned coil evaporator, for use in a CO_2 heat pump system. The model uses the following as input: geometrical parameters, CO_2 inlet temperature, enthalpy and mass flow; and air inlet temperature, relative humidity and velocity. Under the assumptions of no pressure drop, homogeneous flow, counter current heat exchange and negligible tube axial heat conduction, the output parameters of both CO_2 and air as well as the heat transfer capacity is calculated (Dazhang *et al.*, 2009).

For the two-phase region the Gungor & Winterton correlation was used to predict the CO_2 heat transfer coefficient while Petukhov's heat transfer correlation was used to predict the superheated region. The heat transfer coefficient on the airside was calculated as proposed by Wu Yezheng.

By varying parameters such as inlet air temperature, velocity and evaporating temperature the following results were obtained:

- In the two-phase region, heat transfer capability and CO_2 outlet enthalpy increased almost linearly with increasing air inlet temperature, while CO_2 outlet temperature remained constant.
- CO_2 outlet temperature decreased linearly as evaporating temperature increased.
- Heat transfer capacity and CO_2 outlet temperature increased as air velocity increased.

2.8.5. Study by Bendaoud *et al.* (2010)

The authors developed a homogeneous model to simulate the thermo-physical behaviour of a wavy finned coil CO_2 evaporator with a staggered tube arrangement. The model was designed for sub-cooled, two-phase and superheated CO_2 flows under the following assumptions:

- Steady state operation.
- One dimensional tube flow.
- Negligible gravity forces.
- Negligible heat loss to the environment.
- Uniform air velocity.
- Dry conditions (no condensation/dehumidification).

Although the model was designed for a wide range of operating parameters, it was validated at very low air temperatures that are typically found in supermarket applications. For validation, results from a previous model by Ouzzane & Aidoun (2008) with inlet air temperatures between -21.84°C and -10.1°C were used. Experimental data was also used from an ASHREA standard test bench at Canmet ENERGY Laboratories, with inlet air temperatures varied between -35°C and -15°C (Bendaoud *et al.*, 2010).

For calculating the single-phase CO_2 heat transfer coefficient, the correlation proposed by Petukhov and Kirillov as reported by Kakaç *et al.*, 1998 was used and the Drew *et al.*, 1932 correlation for friction factor. For two-phase flow, the Hwang *et al.*, 1997 modified Bennett-Chen correlation was used and for the airside heat transfer and the Wang *et al.* (2002) correlation for pressure drop. The CO_2 two-phase pressure drop was calculated by following a homogeneous approach. In another

study on refrigerant circuitry by Aidoun & Ouzzane (2009) the correlation by Rohsenow *et al.*, 1998 was used to predict the two-phase CO_2 pressure drop.

Good agreement with the experimental results was achieved. However, pressure drop calculations were not as accurate when compared to the experimental data. The authors attributed the discrepancy to possible large jumps, per iteration, in quality over a whole tube length, which may cause the correlation limits to be overshot.

Bendaoud *et al.* (2010) found that during CO_2 two-phase flow, heat transfer was at a maximum and pressure drop was lower than usual, compared to other refrigerants. As a result, a smaller temperature glide was observed. Another reported conclusion was that high air velocities give higher overall heat transfer and is expected considering the discussion in section 2.4.2.

2.8.6. Study by Minetto (2011)

In this study, a heat pump system used for residential hot water heating was developed. It featured two finned coil evaporators connected in parallel. A model was set up to determine the optimum gas cooler pressure for a constant water delivery temperature by varying the air inlet temperature between -5°C and 25°C with a relative humidity of 78%; except for 5°C and 10°C which were at 63% (Minetto, 2011).

CO_2 two-phase heat transfer coefficients were determined with the Chen *et al.* (2006) correlation and the single-phase coefficients with the Gnielinski, 1976 correlation. The two-phase pressure drop was calculated using the correlation by Friedel (1979) and single-phase pressure drop using Churchill's, 1977 correlation. Heat transfer coefficients on the airside and pressure drop for plain fins were calculated using Wang *et al.* (2000a).

The authors had drawn no conclusion to the accuracy of these correlations, although the overall heat pump model accurately predicted the experimental results.

2.8.7. Study by Wang *et al.* (2012)

A prototype air-source CO_2 heat pump water heater was experimentally tested to identify and describe the main factors affecting such a system. The authors also created simulation models for the cycle and for the prototype. They tested the effects of discharge pressure on CO_2 gas cooler outlet temperature, system Coefficient Of Performance (COP), evaporating pressure and the effect of superheat. Along with several other studies, they found that there is an optimum discharge pressure at which the system COP is a maximum. They also tested the effects of ambient and water outlet temperatures on gas cooler outlet temperature, system COP, evaporating temperatures and optimum pressure.

To simulate the evaporator, the correlation by Cheng *et al.* (2008a&b) was used for the two-phase heat transfer and pressure drop of CO_2, and the Dittus-Boelter (Incropera *et al.*, 2007) correlation for single-phase flow. For the heat transfer coefficient on the airside, Li *et al.*, 1997 was used and the friction factor calculated using Wang *et al.* (2000c). Their model produced good results when compared to data generated from the prototype (Wang *et al.*, 2012).

2.8.8. Summary

The seven studies described above are summarised in Table 6 according to the main topics of interest for the present study. It is clear that the airside heat transfer and pressure drop work of C.C. Wang (1997-2012) are the most influential while the Hwang *et al.*, 1997 modified Bennett-Chen correlation is most commonly used for two-phase heat transfer and pressure drop prediction.

Table 6: Main topics in the reviewed simulation studies.

Study	Two-phase		Single-phase		Airside		Uncertainty analysis	Model validation
	Heat transfer	*Friction factor*	*Heat transfer*	*Friction factor*	*Heat transfer*	*Friction factor*		
Robinson & Groll (1998)	Hwang *et al.*, 1997	Martinelly-Nelson	Petukhov, Kirillov and Popov's	Incropera & Dewit, 1990	Incropera & Dewit, 1990	Incropera & Dewit, 1990	None	None
Domanski (1999)	Jung & Didion, 1989	Pierre, 1964	McAdams ASHRAE, 1993	Petukhov, 1970	Webb, 1990	Webb, 1990	None	Experiment
Ouzzane & Aidoun (2008)	Hwang *et al.*, 1997	Hwang *et al.*, 1997	Not reported	Not reported	Wang *et al.* (2002)	Wang *et al.* (2002)	Kline & McClintock, 1953	Literature, manufacturer, experiment
Dazhang *et al.* (2009)	Gungor & Winterton, 1986	Neglected	Petukhov	Petukhov	Wu Yezheng	Neglected	None	None
Bendaoud *et al.* (2010)	Hwang *et al.*, 1997	Hwang *et al.*, 1997	Petukhov and Kirillov	Drew *et al.*, 1932	Wang *et al.* (2002)	Wang *et al.* (2002)	None	Experiment
Minetto (2011)	Chen *et al.* (2006)	Friedel (1979)	Gnielinski, 1976	Churchill, 1977	Wang *et al.* (2000a)	Wang *et al.* (2000a)	None	Experiment
Wang *et al.* (2012)	Cheng *et al.* (2008a&b)	Cheng *et al.* (2008a&b)	Dittus-Boelter	Not reported	Li *et al.*, 1997	Wang *et al.* (2000c)	Kline & McClintock 1953	Prototype

The results of this summary prompted decisions to use the following correlations for the different parameters. The correlations of Cheng *et al.* (2008a&b) for two-phase heat transfer and pressure drop. The Gnielinski, 1976 correlation for single-phase heat transfer and the Filonenko, 1954 correlation (Venter, 2010) for pressure drop. Furthermore, the Wang *et al.* (2002) correlation for air heat transfer and pressure drop will be used. In addition, the uncertainty analysis proposed by Kline & McClintock, 1953 will be considered.

2.9. Compressor lubricant

Vapour compression heat pump cycles employ a refrigerant compressor in order to achieve the pressure differential over the expansion valve. These compressors use a lubricating substance in order to achieve safe operation and longevity, as well as a seal enabling efficient vapour compression. As a result, some lubricant is picked up and transported by the refrigerant flow through the system components such as heat exchangers. Hence, this lubricant migration influences the heat transfer and pressure drop characteristics of the refrigerant-lubricant flow (Wang *et al.*, 2012).

Lubricant alters the thermo-physical properties of the refrigerant since lubricant viscosity; surface tension and density are orders of magnitude higher than that of the pure refrigerant. Thus, all the favourable properties of a good refrigerant are influenced by the addition of lubricant. These lubricants typically include:

- Poly alpha olefins (PAOs).
- Alkyl benzenes (ABs).
- Polyalkylene glycols (PAGs).
- Polyolesters (POEs).
- Polycarbonate (PC).

- Polyvinyl ether (PVE).
- Alkyl naphthalene (AN).
- Polymer ester (PME).

Of these, the partially miscible PAG and completely miscible POE lubricants are best suited for use in trans-critical CO_2 systems with semi-hermitic reciprocating compressors (Zhao & Bansal, 2009).

Dang *et al.* (2012) conducted a study on the effects of lubricating oil on the flow boiling heat transfer of carbon dioxide with a PAG-type lubricant in 2-6mm diameter horizontal smooth tubes. They found that at low lubricant concentrations, 0.5%-1%, the heat transfer coefficient decreased to half that of pure refrigerant while no further decrease with increase in concentration was observed. However, Cawte *et al.* (1996) found that a 2% concentration had a 12% heat transfer coefficient increase in their study on R12 and R22 in a 8mm diameter copper tube. Also, Zhao *et al.* (2002) found that at concentrations below 3% and vapour qualities below 0.45, the heat transfer coefficient is increased by about 5%-10%. They also reported that the detrimental effects of lubricant are decreased at high heat and mass flux values.

The local effects of lubricant are complex and very little literature on CO_2-lubricant mixtures is available (Zhao & Bansal, 2009). The complexity is made evident by the flow pattern sketches reproduced by Wang *et al.* (2012).

2.10. Summary

The literature survey discussed CO_2 as a refrigerant and the aspects of moist air flowing over fins. Relevant correlations for heat transfer and pressure drop were identified from their respective ranges and their use in similar simulation studies. The effect of the presence of lubricant was briefly described as best found in the available literature.

In the next chapter, the theory governing the heat and mass transfer as well as pressure drop of a finned coil evaporator will be presented.

CHAPTER 3:
Theory

This chapter discusses the theory of a finned coil heat exchanger with dehumidification. For this purpose, the finned coil is divided into several discrete finned tube elements. Within each element, a division between airside -, tube wall - and refrigerant side heat transfer is made. The discussion of this chapter is used to develop the simulation model.

3.1. Introduction

Figure 6 illustrates a simplified finned tube element under dry (Figure 6a) and wet (Figure 6b) conditions. The fins were excluded to simplify the drawings. The air stream is drawn horizontally from left to right ($T_{a,i}$ to $T_{a,e}$). A tube is sectioned in length and only the left side is shown while the CO_2 is flowing vertically from top to bottom ($T_{r,i}$ to $T_{r,e}$). Figure 6b shows the condensate film together with a line representing the change in humidity ratio of the air (ω_i to ω_e).

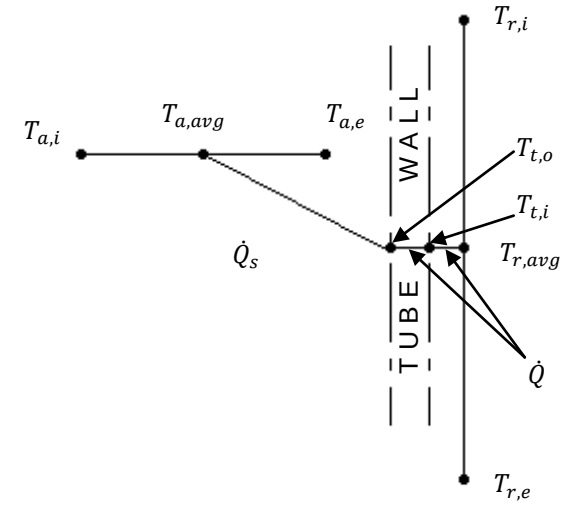

(a)

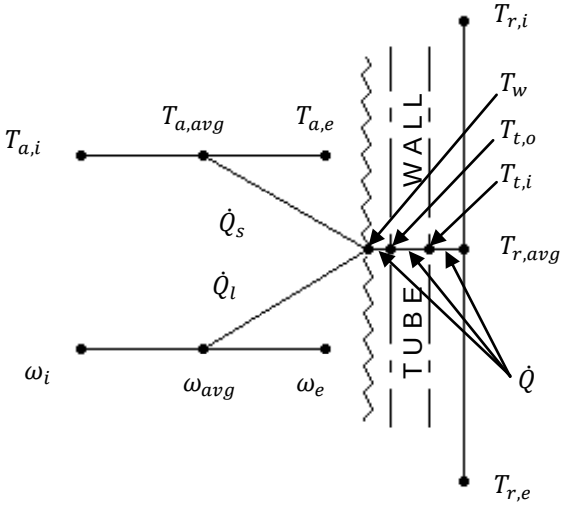

(b)

Figure 6: Schematic illustration of the two fluid streams and their interaction under (a) dry and (b) wet conditions.

Within each dry element, heat is transferred from the air ($\dot{Q}_s$) to the finned tube outer surface, thus cooling the air from inlet ($T_{a,i}$) to outlet ($T_{a,e}$). This heat ($\dot{Q}_s = \dot{Q}$) is then transferred through the tube wall (from $T_{t,o}$ to $T_{t,i}$), ultimately heating the refrigerant from inlet ($T_{r,i}$) to outlet ($T_{r,e}$).

However, within each wet element, sensible heat ($\dot{Q}_s$) as well as latent heat ($\dot{Q}_l$) are transferred from the air to the finned tube outer surface. This results in the air not only being cooled from inlet ($T_{a,i}$) to outlet ($T_{a,e}$), but also dehumidified from inlet (ω_i) to outlet (ω_e). The combined total heat ($\dot{Q}_s + \dot{Q}_l = \dot{Q}$) is then transferred through the condensate film and tube wall (from T_w to $T_{t,i}$), again heating the refrigerant from inlet ($T_{r,i}$) to outlet ($T_{r,e}$).

3.2. Airside

The theory that governs the airside consists of five aspects that are coupled to simulate the airside processes. These aspects are categorised as follows:

- Conservation equations of mass, momentum and energy.
- Fin/surface efficiency.
- Heat transfer correlations.
- Mass transfer correlation.
- Friction factor correlation.

Each of these is discussed separately under the following headings where the fundamental integral forms of the equations are given as well as the derived form, which is used in the simulation model. The coupling of these equations is also given.

3.2.1. Conservation equations

Each type of conservation equation will be discussed separately, and the equations are shown as they apply to a finite Control Volume (CV) defined by Rousseau (2012).

Conservation of mass

The conservation of mass in integral form for compressible dry air is written as follows:

$$\frac{\partial}{\partial t}\left(\iiint \rho d\forall\right) + \oiint \rho \bar{V} \cdot \overline{dA} = 0 \tag{3.1}$$

The first term on the left hand side accounts for the rate of change of mass inside the CV while the second term accounts for the net mass flow from the CV. For the application in this study, it reduces to:

$$\dot{m}_e - \dot{m}_i = 0 \tag{3.2}$$

Where:

$\dot{m}$: Air mass flow rate. $[kg/s]$

and "i", "e" refers to the control volume inlet and outlet respectively.

However, as humid air consists of both air and water, the integral form of the mass conservation equation for water also requires consideration. Water is present in the form of a condensate film as well as vapour entrained in the air. Thus, the following equation applies:

$$\frac{\partial}{\partial t}\left(\iiint \rho_w d\forall_w\right) + \oiint \rho_w \bar{V}_w \cdot \overline{dA_w} + \oiint \rho \omega \bar{V} \cdot \overline{dA} = 0 \tag{3.3}$$

Here, the first term on the left hand side represents the rate of change of water mass inside the CV. The second term represents the net water condensate mass flow rate from the CV while the third term represents the net water vapour mass flow rate from the CV. Reducing to:

$$\dot{m}_{w,e} - \dot{m}_{w,i} + \dot{m}_e\omega_e - \dot{m}_i\omega_i = 0 \tag{3.4}$$

Where:

$\dot{m}_w$	: Condensate mass flow rate.	$[kg/s]$
ω	: Air humidity ratio.	$[kg/kg]$

Because of the small amount of water present in humid air and the complexity it adds to the simulation, the conservation of water mass will not be considered. Instead, the dry air mass flow is assumed equal to the humid air mass flow and is constant. To include the effect of the condensate film on pressure drop, as well as heat and mass transfer, a wet airside correlation is used, as will be discussed in section 3.2.3.

Conservation of momentum

The conservation of momentum in integral form for both dry and wet conditions is written as follows:

$$\oiint \tau\overline{dA} + \iiint \overline{B}\rho d\forall = \frac{\partial}{\partial t}\left(\iiint \overline{V}\rho d\forall\right) + \oiint \overline{V}\left(\rho\overline{V}\cdot\overline{dA}\right) \tag{3.5}$$

The first term on the left hand side accounts for all the surface forces acting on the CV while the second term accounts for all the body forces. The first term on the right hand side accounts for the rate of change of momentum inside the CV while the second term accounts for the net momentum flow from the CV. This reduces to:

$$\frac{P}{P_0}\left(P_{0,e} - P_{0,i}\right) + \tfrac{1}{2}\rho V^2\frac{1}{T_0}\left(T_{0,e} - T_{0,i}\right) + \rho g(Z_e - Z_i) + \Delta P_{0,a} = 0 \tag{3.6}$$

Where:

$\Delta P_{0,a}$	: Difference in total air pressure.	$[Pa]$
P	: Static air pressure.	$[Pa]$
P_0	: Total air pressure.	$[Pa]$
ρ	: Air density.	$[kg/m^3]$
V	: Air velocity.	$[m/s]$
T_0	: Total air temperature.	[℃]
g	: Gravitational constant.	$[m/s^2]$
Z	: Height potential difference.	$[m]$

Where "i" or "e" is not indicated, reference is made to the average between the control volume inlet and outlet.

Since the air flows horizontally over the finned tube surface, static pressure loss due to height differences is neglected. The effect of compressibility on momentum changes are very small, compared to the frictional pressure loss and are consequently neglected. The following equation becomes appropriate where only frictional pressure loss is considered:

$$\left(P_{0,e} - P_{0,i}\right) + \Delta P_{0,a} = 0 \tag{3.7}$$

Where $\Delta P_{0,a}$ is calculated with the equation from Waltrich *et al.* (2010):

$$\Delta P_{0,a} = \frac{\dot{m}^2}{2\rho A_{ff}^2}\left[\left(1 - \left(\frac{A_{ff}}{L_{inc}H_{inc}}\right)^2\right)\left(\frac{\rho_i}{\rho_e} - 1\right) + 2f_a\frac{A_o}{A_{ff}}\left(\frac{\rho_i}{\rho_i + \rho_e}\right)\right] \tag{3.8}$$

Where:

A_{ff}	: Free flow area.	$[m^2]$
A_o	: Total outside surface area ($A_t + A_f$).	$[m^2]$
L_{inc}	: Length of an element.	$[m]$
H_{inc}	: Height of an element.	$[m]$
f_a	: Air friction factor.	[-]

The friction factor, f_a, is calculated with the correlation of Wang *et al.* (2002) which will be shown in section 3.2.5.

Conservation of energy

The conservation of energy in integral form for dry conditions is given below. Note that only sensible heat transfer is active, and no condensate film is present.

$$\dot{Q} + \dot{W} = \frac{\partial}{\partial t}\left(\iiint\left(u + \frac{1}{2}V^2 + gz\right)\rho d\forall\right) + \oiint\left(i + \frac{1}{2}V^2 + gz\right)\rho\overline{V}\cdot\overline{dA} \tag{3.9}$$

Here, the first term on the right hand side represents the rate of change of energy inside the CV while the second term represents the net flow of energy from the CV. This gives:

$$\dot{Q}_s = \dot{m}_a Cp_a(T_{a,i} - T_{a,e}) \tag{3.10}$$

Where:

Cp_a	: Air constant pressure specific heat.	$[J/(kg.K)]$
$\dot{Q}_s$	: Sensible heat transfer rate.	$[W]$
T_a	: Air dry-bulb temperature.	$[K]$

In order to calculate $\dot{Q}_s$, Newton's law of cooling is used as follows:

$$\dot{Q}_s = h_{dry}A_o\eta_o(T_{a,avg} - T_{t,o}) \tag{3.11}$$

Where:

h	: Dry airside heat transfer coefficient.	$[W/(m^2 \cdot K)]$
η_o	: Overall surface efficiency.	[-]
$T_{t,o}$	: Outer tube wall temperature.	$[K]$

The dry airside heat transfer coefficient, h_{dry}, is calculated using the correlation proposed by Wang *et al.* (2002). This correlation is discussed later in 3.2.3. The overall surface efficiency, η_o, is defined as:

$$\eta_o = 1 - \frac{A_f}{A_o}(1 - \eta) \tag{3.12}$$

Where:

A_f : Fin surface area. $[m^2]$

η : Single fin surface efficiency. [-]

Where the single fin efficiency, η, is calculated using the Schmidt (1949) approximation which is discussed next in section 3.2.2.

However, under dehumidifying conditions, a condensate film is present and must be considered. Thus, the integral form of the energy conservation equation is rewritten as:

$$\begin{aligned}\dot{Q} + \dot{W} = \frac{\partial}{\partial t}\left(\iiint \left(u_w + \frac{1}{2}{V_w}^2 + gz_w\right)\rho_w d\forall_w\right) + \oiint \left(i_w + \frac{1}{2}{V_w}^2 + gz_w\right)\rho_w \overline{V}_w \cdot \overline{dA_w} \\ + \frac{\partial}{\partial t}\left(\iiint \left(u + \frac{1}{2}V^2 + gz\right)\rho d\forall\right) + \oiint \left(i + \frac{1}{2}V^2 + gz\right)\rho \overline{V} \cdot \overline{dA}\end{aligned} \tag{3.13}$$

The first term on the right hand side represents the rate of change of energy associated with the water film inside the CV while the second term represents the net flow of energy associated with the water film from the CV. The third term represents the rate of change of energy inside the CV while the fourth term represents the net flow of energy from the CV. This reduces to:

$$\dot{Q} + \dot{W} = \dot{m}_{w,e} i_{w,e} - \dot{m}_{w,i} i_{w,i} + \dot{m}_{w,e} g z_{w,e} - \dot{m}_{w,i} g z_{w,i} + \dot{m}_e i_e - \dot{m}_i i_i + \dot{m}_e g z_e - \dot{m}_i g z_i \tag{3.14}$$

Where:

i : Enthalpy. $[J/kg]$

$\dot{W}$: Work. $[W]$

No work is done on the fluid, thus $\dot{W} = 0$. Given that the airflow is horizontal, the energy associated with elevation differences is neglected. The energy contribution of the condensate film is very small and therefore neglected.

Thus from Rousseau (2012):

$$\dot{Q}_l = \dot{m}_a i_v (\omega_i - \omega_e) \tag{3.15}$$

Where i_v, is the enthalpy of the vapour entrained in the air.

To calculate $\dot{Q}_l$, the following equation from Rousseau (2012) is used:

$$\dot{Q}_l = h_m A_o \eta_{o,wet} (\omega_w - \omega_{avg})(i_w - i_v) \tag{3.16}$$

With i_w, the enthalpy of the condensate film at the tube outer surface temperature ($T_{t,o}$). Also, ω_w is the humidity at the surface of the condensate film. The wet surface efficiency is again calculated with the Schmidt approximation, but using the wet surface heat transfer coefficient, h_{wet}. The heat transfer coefficient for wet surfaces is calculated with the correlation proposed by Kuvannarat *et al.* (2006) and will be discussed in section 3.2.3. The mass transfer coefficient, h_m, is calculated from a ratio with the wet heat transfer coefficient. Bourabaa *et al.* (2011) correlates this ratio, as will be discussed in section 3.2.4.

3.2.2.Fin/surface efficiency

The fin efficiency is calculated with the Schmidt, (1949) approximation. It is used to determine the fin efficiency for a continuous fin by approximating it as if each tube had equivalent circular fins. To determine the dry fin efficiency, the following set of equations is used:

$$\eta = \frac{\tanh(mr_o\phi)}{mr_o\phi} \tag{3.17}$$

with

$$m = \sqrt{\frac{2h_{dry}}{k_f\delta_f}} \tag{3.18}$$

and

$$\phi = \left(\frac{R_{eq}}{r_o} - 1\right)(1 + 0.35\ln\frac{R_{eq}}{r_o}) \tag{3.19}$$

with

$$\frac{R_{eq}}{r_o} = 1.27\frac{X_M}{r_o}(\frac{X_L}{X_M} - 0.3)^{0.5} \tag{3.20}$$

including

$$X_M = \frac{P_t}{2} \tag{3.21}$$

and

$$X_L = \sqrt{({X_M}^2 + {P_l}^2)}/2 \tag{3.22}$$

Where:

k	: Thermal conductivity.	$[W/(m \cdot K)]$
P_l	: Longitudinal tube spacing.	$[m]$
P_t	: Transverse tube spacing.	$[m]$
r_o	: Tube outer radius.	$[m]$
δ_f	: Fin thickness.	$[m]$

However, to determine the wet fin efficiency, m is calculated using the wet heat transfer coefficient, h_{wet}:

$$m = \sqrt{\frac{2h_{wet}}{k_f\delta_f}} \tag{3.23}$$

The wet heat transfer coefficient is calculated with the correlation of Kuvannarat *et al.* (2006) which will be discussed below in section 3.2.3.

3.2.3.Heat transfer correlations

The correlation of Wang *et al.* (2002) were used to determine the dry airside heat transfer coefficient, h_{dry}:

$$Nu = \frac{h_{dry}D_c}{k_a} = j_{dry}Re_{D_c}Pr_a^{\frac{1}{3}} \tag{3.24}$$

Where:

D_c : Collar diameter. $[m]$

j_{dry} : Colburn-j factor for heat transfer. [-]

Nu : Nusselt number. [-]

Pr : Prandl number. [-]

Re_{Dc} : Reynolds number based in the collar diameter. [-]

For $300 < Re_{Dc} < 1000$

$$j_{dry} = 0.882 {Re_{Dc}}^{J1} \left(\frac{D_c}{D_h}\right)^{J2} \left(\frac{F_s}{P_t}\right)^{J3} \left(\frac{F_s}{D_c}\right)^{-1.58} (\tanh\theta)^{-0.2} \quad (3.25)$$

Where

$$J1 = 0.0045 - 0.491 {Re_{Dc}}^{-0.0316-0.0171\ln(N\tan\theta)} \left(\frac{P_l}{P_t}\right)^{-0.109\ln(N\tan\theta)} \left(\frac{D_c}{D_h}\right)^{0.542+0.0471N} \left(\frac{F_s}{D_c}\right)^{0.984} \left(\frac{F_s}{P_t}\right)^{-0.349} \quad (3.26)$$

And

$$J2 = -2.72 + 6.84\tan\theta \quad (3.27)$$

with

$$J3 = 2.66\tan\theta \quad (3.28)$$

For $1000 \leq Re_{Dc} < 10000$

$$j_{dry} = 0.0646 {Re_{Dc}}^{J1} \left(\frac{D_c}{D_h}\right)^{J2} \left(\frac{F_s}{P_t}\right)^{-1.03} \left(\frac{P_l}{D_c}\right)^{0.432} (\tan\theta)^{-0.692} N^{-0.737} \quad (3.29)$$

Where

$$J1 = -0.0545 - 0.0538\tan\theta - 0.302 N^{-0.24} \left(\frac{F_s}{P_l}\right)^{-1.3} \left(\frac{P_l}{P_t}\right)^{0.379} \left(\frac{P_l}{D_h}\right)^{-1.35} (\tan\theta)^{-0.256} \quad (3.30)$$

and

$$J2 = -1.29 \left(\frac{P_l}{P_t}\right)^{1.77-9.43\tan\theta} \left(\frac{D_c}{D_h}\right)^{0.229-1.43\tan\theta} N^{-0.166-1.08\tan\theta} \left(\frac{F_s}{P_t}\right)^{-0.174\ln(0.5N)} \quad (3.31)$$

Where:

D_h : Hydraulic diameter. $[m]$

F_s : Fin spacing. $[m]$

N : Number of tube rows. [-]

θ : Corrugation angle. $[Deg]$

The wet surface heat transfer coefficient, h_{wet}, is calculated with the correlation proposed by Kuvannarat *et al.* (2006) as follows:

$$j_{wet} = 0.213262 {Re_{Dc}}^{-0.51507} N^{0.09891} \left(\frac{A_o}{A_t}\right)^{0.600543} \left(\frac{\delta_f}{P_l}\right)^{0.072448} \quad (3.32)$$

Where:

A_t : Tube surface area. $[m^2]$

Also, j_{dry} is replaced with j_{wet} in equation 3.24.

3.2.4.Mass transfer correlation

The mass transfer coefficient, h_m, is calculated from the Lewis number. The Lewis number represents the ability to transport heat versus the ability to transport mass. Thus:

$$Le = \frac{h_{wet}}{h_m Cp} \tag{3.33}$$

Researchers such as Bourabaa *et al.* (2011) and Pirompugd *et al.* (2007) have shown that the commonly accepted assumption of a unity Lewis number is incorrect. Pirompugd *et al.* (2007) proposed a correlation ($300 < Re_{Dc} < 5500$) for the Lewis number as follows:

$$Le = 2.28N^{0.2393}\left(\frac{F_s}{D_c}\right)^{0.0239N+0.4332}\left(\frac{A_o}{A_t}\right)^{0.0321N+0.0747} Re_{Dc}^{-0.01833N+0.194\left(\frac{F_s}{D_c}\right)-0.0026\left(\frac{P_l}{D_c}\right)-0.03012\left(\frac{P_t}{D_c}\right)+0.0418} \tag{3.34}$$

3.2.5.Friction factor correlation

The friction factor, f_a, is calculated by using the correlation proposed by Wang *et al.* (2002) as follows:

For $300 < Re_{Dc} < 1000$

$$f_a = 4.37 {Re_{Dc}}^{F1}\left(\frac{F_s}{D_h}\right)^{F2}\left(\frac{P_l}{P_t}\right)^{F3}\left(\frac{D_c}{D_h}\right)^{0.2054} N^{F4} \tag{3.35}$$

Where

$$F1 = -0.574 - 0.137(\ln(Re_{Dc}) - 5.26)^{0.245}\left(\frac{P_t}{D_c}\right)^{-0.765}\left(\frac{D_c}{D_h}\right)^{-0.243}\left(\frac{F_s}{D_h}\right)^{-0.474}(\tan\theta)^{-0.217} N^{0.035} \tag{3.36}$$

and

$$F2 = -3.05\tan\theta \tag{3.37}$$

with

$$F3 = -0.192N \tag{3.38}$$

and

$$F4 = -0.646\tan\theta \tag{3.39}$$

For $1000 \leq Re_{Dc} < 10000$

$$f_a = 0.228 {Re_{Dc}}^{F1}(\tan\theta)^{F2}\left(\frac{F_s}{P_l}\right)^{F3}\left(\frac{P_l}{D_c}\right)^{F4}\left(\frac{D_c}{D_h}\right)^{0.383}\left(\frac{P_l}{P_t}\right)^{-0.247} \tag{3.40}$$

Where

$$F1 = -0.141\left(\frac{F_s}{P_l}\right)^{0.0512}(\tan\theta)^{-0.472}\left(\frac{P_l}{P_t}\right)^{0.35}\left(\frac{P_t}{D_h}\right)^{0.449\tan\theta} N^{-0.049+0.237\tan\theta} \tag{3.41}$$

and

$$F2 = -0.562(\ln(Re_{Dc}))^{-0.0923} N^{0.013} \tag{3.42}$$

With

$$F3 = 0.302\, Re_{Dc}{}^{0.03} \left(\frac{P_t}{D_c}\right)^{0.026} \tag{3.43}$$

and

$$F4 = -0.306 + 3.63 \tan\theta \tag{3.44}$$

3.3. Tube wall

The heat transferred through the tube wall is defined as pure conduction and is calculated with Rousseau (2012) and Incropera *et al.* (2007):

$$\dot{Q} = \frac{2\pi k_t L_{inc}}{\ln\left(\frac{r_o}{r_i}\right)} \left(T_{t,o} - T_{t,i}\right) \tag{3.45}$$

Where:

r_i	: Inner tube radius.	$[m]$
$T_{t,i}$	: Inner tube wall temperature.	$[K]$

3.4. Refrigerant side

The CO_2 enters as a two-phase mixture and goes through flow boiling to reach saturation. After saturation is reached, single-phase convection occurs. The theory describing the refrigerant side consists of four aspects:

- Conservation equations of mass, momentum and energy.
- Two-phase heat transfer and pressure drop correlations.
- Single-phase heat transfer and pressure drop correlations.

3.4.1. Conservation equations

The conservation equations are applied to a finite control volume as defined by Rousseau (2012).

Conservation of mass

For both the two-phase and single-phase zones, the integral form of the conservation of mass equation is the same as equation 3.1 for dry air, and similarly reduces to:

$$\dot{m}_e - \dot{m}_i = 0 \tag{3.46}$$

Conservation of momentum

The integral form of the conservation of momentum is the same as equation 3.5, however, since both gas and liquid are present during two-phase flow; neither the assumption of compressibility nor incompressibility is valid. The following equation is therefore used:

$$(P_{0e} - P_{0i}) - \tfrac{1}{2} V_i V_e (\rho_e - \rho_i) + \rho g (Z_e - Z_i) + \Delta P_r = 0 \tag{3.47}$$

Where:

ΔP_r	: Difference in refrigerant pressure.	$[Pa]$
V	: Refrigerant velocity.	$[m^2]$

Since the refrigerant flow is horizontal through the tubes, static pressure loss due to elevation differences is neglected. The effect of phase change acceleration, on momentum changes are very

small compared to frictional pressure loss and are consequently neglected. The following equation becomes appropriate where only frictional pressure loss is considered:

$$(P_{0e} - P_{0i}) + \Delta P_r = 0 \tag{3.48}$$

Where ΔP_r in the two-phase zone is calculated using the correlation of Cheng *et al.* (2008a), in the superheated zone, Filonenko, 1954 is used. These correlations will be discussed in sections 3.4.2 and 3.4.3.

Conservation of energy

The integral form of the energy conservation equation is the same as equation 3.9 for dry air. It reduces similarly to:

$$\dot{Q} = \dot{m}_r(i_e - i_i) \tag{3.49}$$

Newton's law of cooling is used to determine the heat transferred:

$$\dot{Q} = h_r A_i (T_{t,i} - T_{r,avg}) \tag{3.50}$$

Where:

A_i : Tube inside surface area. $[m^2]$

The two-phase heat transfer coefficient, h_r, is calculated from the correlation proposed by Cheng *et al.* (2008b). As for the single-phase heat transfer coefficient, the correlation proposed by Gnielinski (Venter, 2010) is used. These will be discussed below in sections 3.4.2 and 3.4.3.

3.4.2.Two-phase correlations

Cheng *et al.* (2008b) and Cheng *et al.* (2008a), respectively correlate the heat transfer coefficients as well as the pressure drop for this zone. As these correlations are phenomenon based, they are compounded for simplicity.

These correlations are based on a phenomenological model where distinct flow patterns are encountered and the heat transfer coefficients as well as the pressure drop are correlated for each pattern. The boundaries where transition from one pattern to another occurs are defined in terms of critical quality and mass flux values.

The following flow patterns are covered by these correlations:

- Slug.
- Stratified-wavy.
- Combination of slug and stratified-wavy.
- Bubbly.
- Intermittent.
- Annular.
- Dryout.
- Mist.

Various researchers, such as Wang *et al.* (2012), have reported that typical mass flux values for industrial CO_2 finned coil evaporators, only entitle the last four flow patterns. Thus, only these flow patterns are included in the discussion below.

Boundary equations (Cheng *et al.* (2008b) and Cheng *et al.* (2008a)):

The critical vapour quality value for the transition between intermittent and annular flow are determined with:

$$x_{IA} = \left[1.8^{1/0.875}\left(\frac{\rho_v}{\rho_l}\right)^{-1/1.75}\left(\frac{\mu_l}{\mu_v}\right)^{-1/7} + 1\right]^{-1} \tag{3.51}$$

Where:

μ : Dynamic viscosity. $[kg/(m \cdot s)]$

The value where the transition between annular and dryout occurs is called the dryout inception vapour quality and is calculated as follows:

$$x_{di} = 0.58e^{[0.52-0.236We_v^{0.17}Fr_{v,Mori}^{0.17}(\rho_v/\rho_l)^{0.25}(q/q_{crit})^{0.27}]} \tag{3.52}$$

Where We_v is the vapour Weber number calculated with:

$$We_v = \frac{G^2 D_i}{\rho_v \sigma} \tag{3.53}$$

Where:

D_i : Inner tube diameter. $[m]$

G : Mass flux. $[kg/m^2]$

σ : Surface tension. $[N/m]$

And $Fr_{v,Mori}$ the vapour Froude number as defined by:

$$Fr_{v,Mori} = \frac{G^2}{\rho_v(\rho_l - \rho_v)gD_i} \tag{3.54}$$

Also the critical heat flux, q_{crit}, is calculated with:

$$q_{crit} = 0.131\rho_v^{0.5}h_{lv}[g\sigma(\rho_l - \rho_v)]^{0.25} \tag{3.55}$$

Where:

h_{lv} : Latent heat of vaporisation. $[J/kg]$

q : Heat flux. $[W/m^2]$

The value, at which the transition from dryout to mist flow occurs, is called the dryout completion vapour quality and is calculated with:

$$x_{de} = 0.61e^{[0.57-0.502We_v^{0.16}Fr_{v,Mori}^{0.15}(\rho_v/\rho_l)^{-0.09}(q/q_{crit})^{0.72}]} \tag{3.56}$$

Intermittent flow

Intermittent flow is present when $x \leq x_{IA}$.

Where: x : Vapour quality. [-]

- *Heat transfer coefficient:*

The local two-phase flow boiling heat transfer coefficient is calculated with the general Kattan-Thome-Favrat (Kattan *et al.*, 1998) equation:

$$h_r = \frac{\theta_{dry} h_v + \left(2\pi - \theta_{dry}\right) h_{wet}}{2\pi} \tag{3.57}$$

Where

θ_{dry} : The angle of the dry perimeter. $[rad]$

However, no slug, stratified-wavy or combination thereof is present, thus $\theta_{dry} = 0$.

The heat transfer for the vapour phase h_v, is calculated with the Dittus-Boelter equation (Incropera *et al.*, 2007) as follows:

$$h_v = 0.023 Re_v^{0.8} Pr_v^{0.4} \frac{k_v}{D_i} \tag{3.58}$$

Where Re_v is the vapour phase Reynolds number defined as:

$$Re_v = \frac{GxD_i}{\mu_v \varepsilon} \tag{3.59}$$

and the void fraction, ε, is calculated with:

$$\varepsilon = \frac{x}{\rho_v}\left[\left(1 + 0.12(1-x)\right)\left(\frac{x}{\rho_v} + \frac{1-x}{\rho_l}\right) + \frac{1.18(1-x)[g\sigma(\rho_l - \rho_v)]^{1/4}}{G\rho_l^{1/2}}\right]^{-1} \tag{3.60}$$

also, Pr_v is the vapour phase Prandl number:

$$Pr_v = \frac{Cp_v \mu_v}{k_v} \tag{3.61}$$

The heat transfer coefficient present on the wetted perimeter, h_{wet}, is calculated with an asymptotic model combining the two mechanisms, nucleate and convective boiling. As follows:

$$h_{wet} = [(Sh_{nb})^3 + h_{cb}^3]^{1/3} \tag{3.62}$$

Where the suppression factor (S) for nucleate boiling due to the thinning of the liquid film is set equal to one for this flow pattern.

The nucleate boiling heat transfer coefficient, h_{nb}, is calculated by the modified Cooper correlation:

$$h_{nb} = 131 p_r^{-0.0063} (-log_{10} p_r)^{-0.55} M^{-0.5} q^{0.58} \tag{3.63}$$

Where:

p_r : Reduced pressure ($p_r = P/P_{crit}$). [-]

M : Molecular weight. $[kg/kmol]$

The convective boiling heat transfer coefficient is calculated with:

$$h_{cb} = 0.0133 Re_\delta^{0.69} Pr_l^{0.4} \frac{k_l}{\delta_r} \tag{3.64}$$

Where, δ_r : Thickness of the liquid film. $[m]$

With Re_δ the liquid film Reynolds number:

$$Re_\delta = \frac{4G(1-x)\delta_r}{\mu_l(1-\varepsilon)} \tag{3.65}$$

Where δ_r is the thickness of the liquid film and is calculated by:

$$\delta_r = \frac{D_{eq}}{2} - \sqrt{\left(\frac{D_{eq}}{2}\right)^2 - \frac{2A_l}{2\pi - \theta_{dry}}} \tag{3.66}$$

Where:

D_{eq} : Equivalent tube inner diameter. $[m]$

A_l : Liquid phase cross-sectional area. $[m^2]$

If $D_{eq} > 7.53\text{mm}$ (in the present study $D_{eq} = D_i = 9.28\text{mm}$), then set $D_{eq} = 7.53\text{mm}$. A_l is the cross-sectional area occupied by the liquid-phase:

$$A_l = A_{ff,r}(1-\varepsilon) \tag{3.67}$$

Whenever the liquid occupies more than one-half of the cross-section, equation 3.66 would yield $\delta_r > \frac{D_{eq}}{2}$ which is not possible, thus $\delta_r = \frac{D_{eq}}{2}$.

and Pr_l is the liquid film Prandl number:

$$Pr_l = \frac{Cp_l\mu_l}{k_l} \tag{3.68}$$

- *Pressure drop:*

The pressure drop for the intermittent flow region is defined as:

$$\Delta P_I = \Delta P\left(1 - \frac{\varepsilon}{\varepsilon_{IA}}\right) + \Delta P_A\left(\frac{\varepsilon}{\varepsilon_{IA}}\right) \tag{3.69}$$

Where Δp_A is calculated with equation 3.74 and the single-phase frictional pressure drop, considering the total two-phase flow as a liquid flow, is calculated with:

$$\Delta P = 4f_{LO}\frac{L_{inc}}{D_i}\frac{G^2}{2\rho_l} \tag{3.70}$$

With the Blasius friction factor calculated as:

$$f_{LO} = \frac{0.079}{Re_{LO}^{0.25}} \tag{3.71}$$

And the Reynolds number defined as:

$$Re_{LO} = \frac{GD_i}{\mu_l} \tag{3.72}$$

Annular

Annular flow is present when $x_{IA} < x \leq x_{di}$.

- *Heat transfer coefficient:*

The same equation for two-phase local heat transfer coefficient (3.56) is used. However, the nucleate boiling suppression factor that was set equal to one for intermittent flow is now defined by:

$$S = 1 - 1.14\left(\frac{D_{eq}}{0.00753}\right)^2\left(1 - \frac{\delta_r}{\delta_{r,IA}}\right)^{2.2} \tag{3.73}$$

Where D_{eq} and δ_r are calculated in the same manner although, $\delta_{r,IA}$ is evaluated at the intermittent to annular transition quality with equation 3.51.

- *Pressure drop:*

The pressure drop is calculated with:

$$\Delta P_A = 4 f_A \frac{L_{inc}}{D_i}\frac{\rho_v V_{avg,v}^2}{2} \tag{3.74}$$

The average vapour velocity is calculated by:

$$V_{avg,v} = \frac{Gx}{\rho_v \varepsilon} \tag{3.75}$$

and the annular friction factor is correlated by:

$$f_A = 3.128 Re_v^{-0.454} We_l^{-0.0308} \tag{3.76}$$

Where the vapour phase Reynolds number is again calculated with equation 3.59 and the liquid phase Weber number with:

$$We_l = \frac{\rho_l V_{avg,l}^2 D_i}{\sigma} \tag{3.77}$$

With the average liquid velocity calculated by:

$$V_{avg,l} = \frac{G(1-x)}{\rho_l(1-\varepsilon)} \tag{3.78}$$

Dryout

Dryout occurs when $x_{di} < x \leq x_{de}$.

- *Heat transfer coefficient:*

In the dryout region, the heat transfer coefficient is calculated with a linear interpolation proposed by Wojtan *et al.* (2005):

$$h_D = h_{tp}(x_{di}) - \frac{x - x_{di}}{x_{de} - x_{di}}\left[h_{tp}(x_{di}) - h_M(x_{de})\right] \tag{3.79}$$

Where $h_{tp}(x_{di})$ is the heat transfer coefficient calculated with equation 3.57 at the dryout inception quality, x_{di}, and $h_M(x_{de})$ is the mist flow heat transfer coefficient calculated with equation 3.81 at the dryout completion quality, x_{de}. If $x_{de}$is not defined for a condition it is set equal to 0.999.

- *Pressure drop:*

A linear interpolation is proposed for the frictional pressure drop as:

$$\Delta P_D = \Delta P_A(x_{di}) - \frac{x - x_{di}}{x_{de} - x_{di}}[\Delta P_A(x_{di}) - \Delta P_M(x_{de})] \quad (3.80)$$

Where $\Delta p_A(x_{di})$ is the frictional pressure drop calculated with equation 3.74 at the dryout inception quality, x_{di}, and $\Delta p_M(x_{de})$ is the frictional pressure drop calculated with equation 3.84 at the dryout completion quality, x_{de}. Again, if x_{de} is not defined for a condition it is set equal to 0.999.

Mist

Mist flow is present when $x \leq x_{de}$.

- *Heat transfer coefficient:*

The heat transfer coefficient is calculated with the modified Groeneveld correlation (Groeneveld, 1973):

$$h_M = 2 \times 10^{-8} Re_H^{1.97} Pr_v^{1.06} Y^{-1.83} \frac{k_v}{D_i} \quad (3.81)$$

Where the homogeneous Reynolds number is defined as:

$$Re_H = \frac{GD_{eq}}{\mu_v}\left[x + \frac{\rho_v}{\rho_l}(1 - x)\right] \quad (3.82)$$

and the correction factor as:

$$Y = 1 - 0.1\left[\left(\frac{\rho_l}{\rho_v} - 1\right)(1 - x)\right]^{0.4} \quad (3.83)$$

- *Pressure drop:*

The frictional pressure drop is calculated with:

$$\Delta P_M = 4 f_M \frac{L_{inc}}{D_i} \frac{G^2}{2\rho_H} \quad (3.84)$$

Where the homogeneous density is calculated with:

$$\rho_H = \rho_l(1 - \varepsilon_H) + \rho_v \varepsilon_H \quad (3.85)$$

And the homogenous void fraction is calculated as:

$$\varepsilon_H = \left(1 + \frac{(1 - x)}{x}\frac{\rho_v}{\rho_l}\right)^{-1} \quad (3.86)$$

The friction factor for mist flow is correlated as:

$$f_M = \frac{91.2}{Re_M^{0.832}} \quad (3.87)$$

And the Reynolds number is defined as

$$Re_M = \frac{GD_i}{\mu_H} \quad (3.88)$$

With the homogenous dynamic viscosity calculated as proposed by Ciccitti *et al.* (1960):

$$\mu_H = \mu_l(1 - x) + \mu_v x \quad (3.89)$$

3.4.3. Single-phase correlations

- *Heat transfer coefficient:*

The heat transfer coefficient is calculated with the Gnielinski, 1976 correlation:

$$Nu = \frac{h_{sh} D_i}{k_r} = \frac{f_{sh}}{8}(Re - 1000)Pr\left[1.07 + 12.7\sqrt{\frac{f}{8}}\left(Pr^{2/3} - 1\right)\right]^{-1} \quad (3.90)$$

Where f_{sh} is calculated with the Filonenko friction factor correlation (Venter, 2010):

$$f_{sh} = (1.82 \log Re - 1.64)^{-2} \quad (3.91)$$

and Re is the Reynolds number calculated as:

$$Re = \left|\frac{\dot{m}_r D_i}{\mu_r A_{ff,r}}\right| \quad (3.92)$$

The Prandl number is calculated as:

$$Pr = \frac{Cp\ \mu}{k} \quad (3.93)$$

- *Pressure drop:*

The superheated zone pressure drop is calculated by:

$$\Delta P_{sh} = f_{sh} \frac{L_{inc}}{D_i} \frac{V_r^2}{2g} \rho g \quad (3.94)$$

Where f_{sh} is calculated with equation 3.91.

3.5. Summary

This chapter describes the theory governing the heat transfer and pressure drop processes. The fundamental equations and simplifying assumptions were briefly discussed. The next chapter, implements these equations to develop the simulation model for the present study.

CHAPTER 4:
Simulation Model

This chapter describes the detail of the simulation model developed for this study. A detailed discussion of the wavy-finned CO_2 coil simulation model will be done under the following headings:

- Overview of heat exchanger configuration.
- Heat exchanger discretisation.
- Heat exchanger geometry.
- Refrigerant inlet.
- Air inlet.
- Program execution.
- Output.

4.1. Overview of heat exchanger configuration

It is worth noting here, that the present model was developed to simulate the finned coil evaporator used in the upgrade of the test facility, as shown in Figure 7 below. Thus, the fixed geometry of this coil was a characteristic according to which the model was developed and evaluated.

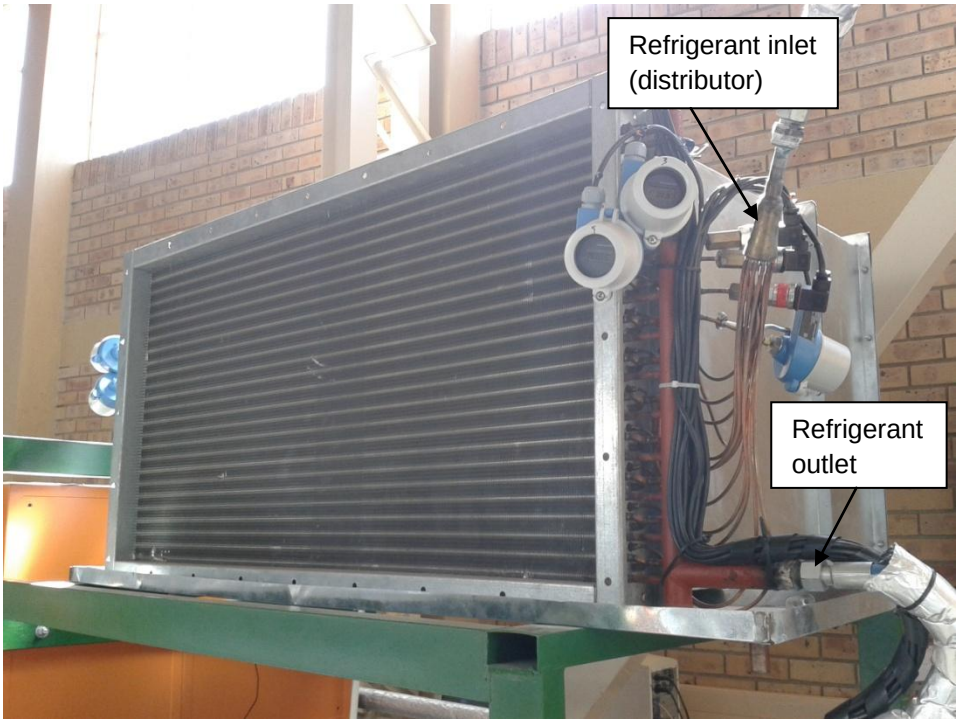

Figure 7: Photo of the already installed finned coil evaporator to be simulated.

Under the assumption that the inlet distributor divides the refrigerant mass flow equally between all twelve circuits, it was thus assumed that their thermo-physical behaviour is identical. It was then decided to only simulate one circuit of the finned coil and the total finned coil values derived from this. In the simplified schematic below (Figure 8) (the fins and support frame is not drawn), the finned coil is shown with the simulated circuit indicated.

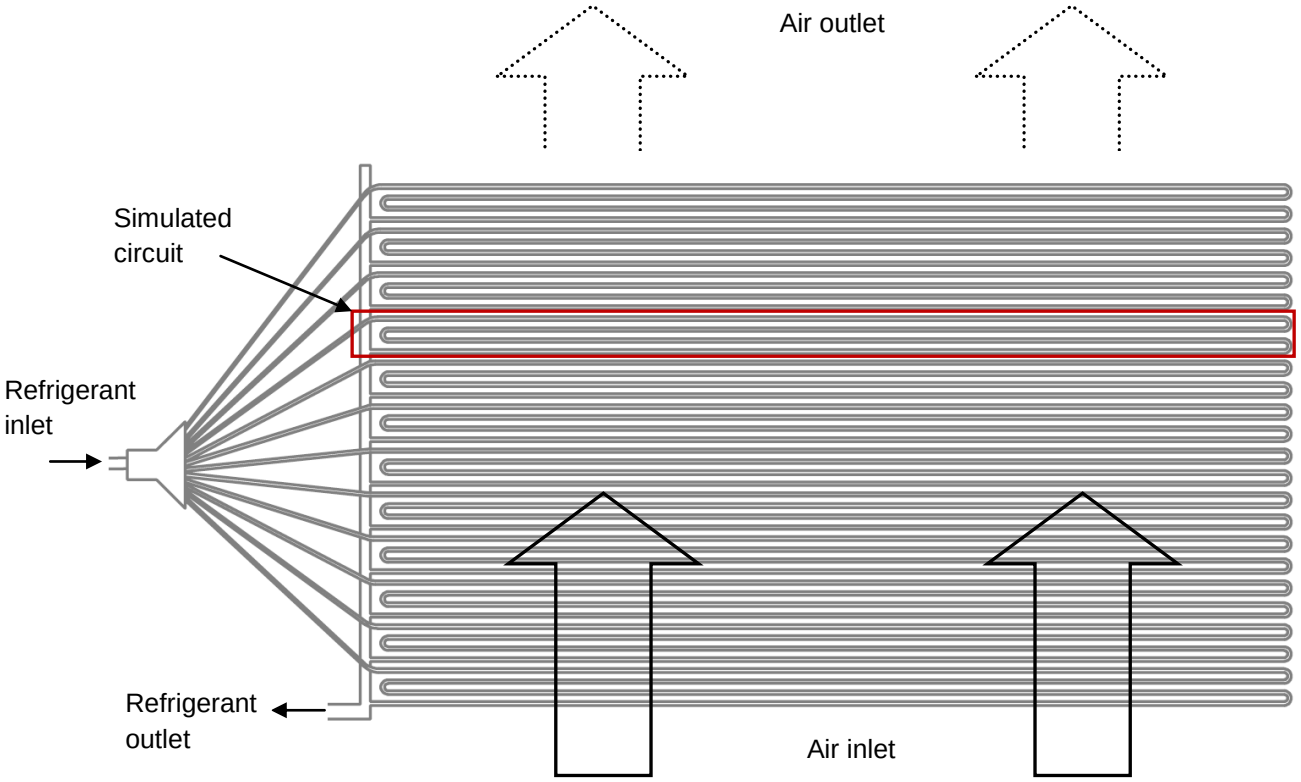

Figure 8: Schematic frontal view of the finned coil indicating the simulated circuit.

A three dimensional view of the circuit is given in Figure 9 where the fins were again omitted to simplify the figure. Also shown are the inlets and outlets of the two fluid streams.

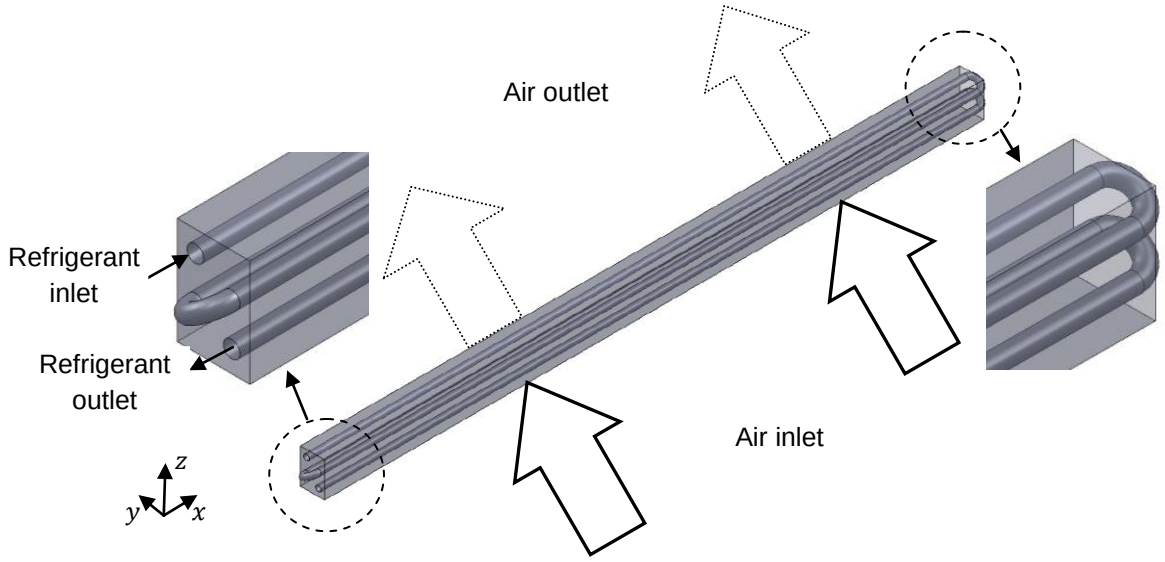

Figure 9: Isometric view of the simulated circuit showing the air and refrigerant inlets and outlets.

Upon closer inspection of Figure 9, it is clear that the refrigerant flows from one end of a tube to the other in the x-direction, perpendicular to the airflow which is in the y-direction. This type of configuration is therefore accurately termed cross flow. In addition, closer inspection of the tube bends on the far side shows that the refrigerant predominantly flows from the back of the circuit to the front, in a $-y$ direction. Thus a counter flow configuration with respect to the airflow, also applies.

This cross-counter flow configuration is used in industry because since a better heat transfer is realised due to the counter flow characteristic.

4.2. Heat exchanger discretisation

To capture the different refrigerant flow patterns and heat transfer zones, as well as to simulate partially wet conditions by using only wet or dry correlations, the circuit is discretised with respect to length. Thus, each $1.2m$ tube is divided into eight equal length elements. Each of these elements is modelled as a separate heat exchanger (Figure 11) with its own fluid inlets and outlets, which are then linked to the adjacent elements. Thus as shown in Figure 10, the refrigerant outlet of one element is seen as the inlet of the next. The tube bends are not simulated since they are not finned and are not exposed to the main airflow. Figure 10 shows each element with its associated control volume.

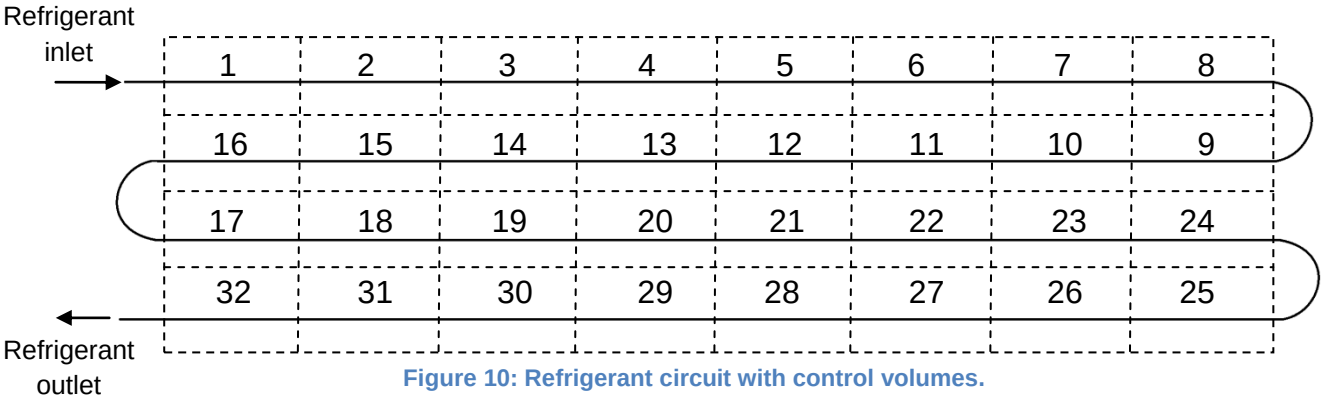

Figure 10: Refrigerant circuit with control volumes.

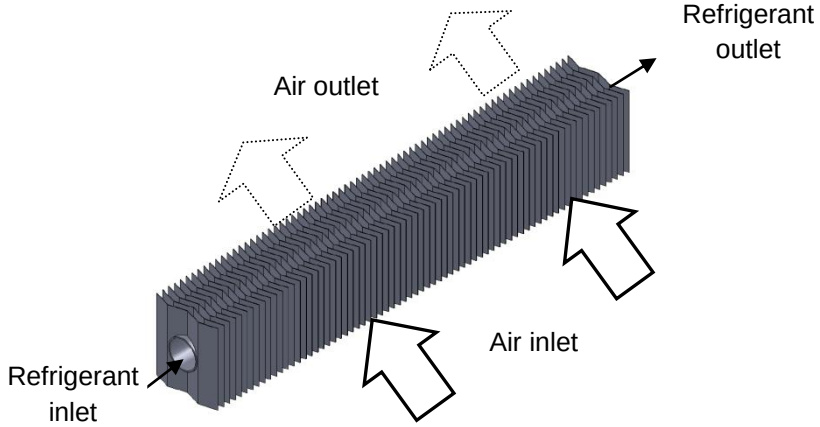

Figure 11: Isometric view of a single element showing inlets and outlets.

This equates to an element length, L_{inc}, of $0.15m$.

Figure 12 shows a side view in the direction of the positive x-axis as indicated in Figure 9. In Figure 12, a cross represents a refrigerant flow direction into the page and a circle represents a flow direction outwards from the page. It is clear that since the tubes have a staggered counter flow arrangement, the air links are not as simple. The second and fourth tubes are situated in front of the first and third tubes as shown in Figure 12. Consequently, only the elements on the tubes that are in front (two and four), receive air at ambient conditions as inlet. The elements on the tubes behind (one and three), receive a mixture of outlets from the elements on the tubes that are in front. Thus, their inlets are taken as the average of the two element outlets, preceding that element.

An assumption is made that the outlet of these elements are thoroughly mixed and in equilibrium. Since all the circuits are assumed thermo-physically identical, it can be assumed that the element inlets of tube one also consists of the outlets of the elements of tubes two and four.

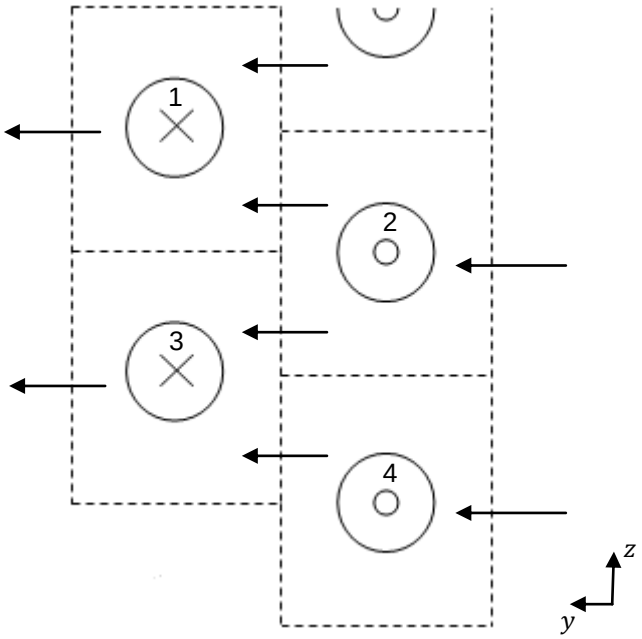

Figure 12: Schematic showing the airside interaction between the elements.

Fluid properties, per element, are commonly calculated at the average between their inlet and outlet values. In this study, to achieve better calculation time and stability, the fluid properties are evaluated at the inlet of the elements, which is referred to as an upwind discretisation. This discretisation is valid for small variations within an element, as is the case with the present study simulation.

Since the present simulation makes use of extensive correlations, the following assumptions were made in order to simplify calculations:

- *Negligible heat transfer to the environment* - Thus, it was assumed that no heat is transferred to the environment through the tube bends, fin tips, side panels, distributor and connecting tubes.
- *Steady state conditions* - Thermal and fluid equilibrium is reached and no variations with time are present.
- *No tube-axial conduction* - There are no thermal conduction from one element to another, through the copper tubes.
- *No fin conduction from one element to another* - No thermal conduction from one element to another, through the aluminium fins
- *Equal fin temperature from tip to base* - There are no temperature gradients present in the fin sheets, thus the fin temperature is always equal to the fin base or collar temperature.
- *No partially wet condition within an element* - Since it was assumed that there are no temperature gradients within a fin, only fully dry or fully wet conditions are handled within an element. However, since the circuit was made up of several dry or wet elements, partially wet circuit conditions are simulated.
- *Uniform airflow distribution* - It was assumed that the air entering the heat exchanger is at uniform temperature, pressure, relative humidity and velocity.

4.3. Heat exchanger geometry

Table 7 lists the various geometric parameters of the wavy finned staggered CO_2 evaporator. The simulation model uses these values.

Table 7: Heat exchanger geometry.

Symbol	Name	Value	Unit
$A_{f,inc}$	Total fin area within an element	0.069973	m^2
$A_{t,inc}$	Total tube area within an element	0.004805	m^2
$A_{o,inc}$	Total outside surface area of an element ($A_{f,inc} + A_{t,inc}$)	0.074436	m^2
$A_{ff,inc,a}$	The free flow area between the fins of an element	0.002028	m^2
D_i	Inner tube diameter	0.00928	m
D_o	Outer tube diameter	0.0101	m
F_p	Fin pitch	0.0021166	m
H_{inc}	Height of an element transverse to airflow	0.0254	m
N	Number of tube rows	2	–
P_t	Transverse tube pitch	0.0254	m
P_l	Longitudinal tube pitch	0.022	m
W_e	Width of evaporator in the airflow direction	0.044	m
W_{inc}	Width of an element in the airflow direction	0.022	m
θ	Wave angle of fins	16	Deg
δ_f	Fin thickness	0.00014	m

SolidWorks 2010 (Dassault Systemes, 2010) was used to create a 3D model of an element in order to extract the four areas tabulated above. The following parameters were received from the manufacturer of the evaporator (HC Heat Exchangers, 2013):D_i, D_o, F_p,N, P_t, P_l and δ_f. Also, the wave angle, θ, had to be derived from fin cut sheets given by the supplier at special request. These specifications are given in Appendix B. In order to measure the width of the heat exchanger, a vernier plunger was inserted between the fins until its tip reached the back end of the fins while the linear displacement of the plunger was recorded. The height and width (H_{inc},W_{inc}) of an element is chosen equal to the transverse and longitudinal tube pitches (P_t,P_l) respectively, to generate symmetrical elements.

To calculate total outside surface area for the whole evaporator, the elemental area, $A_{o,inc}$, is multiplied by the number of elements and the number of circuits. However, to calculate the total free flow area, the elemental free flow area, $A_{ff,inc,a}$, is multiplied by the total number of elements in the first row.

The surface area on the inside of the tube and the inside free flow area is calculated as follows:

$$A_{inc,r} = 2\pi r_i L_{inc} \tag{4.1}$$

and

$$A_{ff,inc,r} = \pi r_i^2 \tag{4.2}$$

Where:

$A_{inc,r}$: Incremental refrigerant heat transfer area. $[m^2]$

$A_{ff,inc,r}$: Incremental refrigerant free flow area. $[m^2]$

L_{inc} : Incremental tube length. $[m]$

The hydraulic diameter is calculated from Wang *et al.* (2002) as:

$$D_h = \frac{4A_{ff,inc,a}W_e}{A_o} \tag{4.3}$$

Where:

$A_{ff,inc,a}$: Incremental air free flow area. $[m^2]$

A_o : Total incremental outside surface area. $[m^2]$

W_e : Width of the finned coil. $[m]$

Conductivity of both the aluminium fins and the copper tube is fixed at 236 $W/m\,K$ and 401.2 $W/m\,K$ respectively.

4.4. Refrigerant inlet

The boundary conditions given in Table 8 are required to fix the two-phase ($0 < x_i \leq 0.999$) refrigerant inlet state.

Table 8: Refrigerant inlet boundary conditions.

Symbol	Name	Unit
$\dot{m}_{r,Tot}$	Total refrigerant mass flow for the twelve circuits	kg/s
$T_{r,i}$	Refrigerant inlet temperature	K
x_i	Refrigerant inlet vapour quality	$-$

The model then calculates the following thermal fluid properties, corresponding to the inlet conditions, with the built-in EES property functions:

- Enthalpy ($i_{r,i}$).
- Entropy ($s_{r,i}$).
- Pressure ($P_{r,i}$).
- Density ($\rho_{r,i}$).
- Thermal conductivity ($k_{r,i}$).
- Specific heat ($Cp_{r,i}$).
- Viscosity ($\mu_{r,i}$).

Where the refrigerant mass flow rate per circuit is calculated as:

$$\dot{m}_r = \frac{\dot{m}_{r,Tot}}{12} \tag{4.4}$$

and the refrigerant mass flux as:

$$G_r = \frac{\dot{m}_r}{A_{ff,inc,r}} \tag{4.5}$$

4.5. Air inlet

The boundary conditions required to fix the air inlet state are given in Table 9.

Table 9: Air inlet boundary conditions.

Symbol	Name	Unit
$P_{a,i}$	Inlet air pressure	Pa
RH_i	Inlet relative humidity	%
$T_{a,i}$	Inlet dry-bulb temperature	K
V_a	Inlet air velocity	m/s

Again, the following thermal fluid properties, corresponding to the inlet conditions, are calculated with the built-in EES property functions:

- Humidity ratio ($\omega_{a,i}$).
- Enthalpy ($i_{a,i}$).
- Density ($\rho_{a,i}$).
- Thermal conductivity ($k_{a,i}$).
- Specific heat ($Cp_{a,i}$).
- Viscosity ($\mu_{a,i}$).

The air mass flow rate, per element, is then calculated as:

$$\dot{m}_a = V_a H_{inc} L_{inc} \rho_{a,i} \tag{4.6}$$

Where, H_{inc} : Height of an element. $[m]$

and the air mass flux as:

$$G_a = \frac{\dot{m}_a}{A_{ff,inc,a}} \tag{4.7}$$

4.6. Program execution

The simulation environment combines all the equations for the pre-calculations, element calculations and post calculations together, and solves them iteratively. The description below presents the logic of the simulation program.

Once all the inputs have been fixed, the pre-calculations are executed. These include the air wet and dry heat transfer coefficients, mass transfer coefficient and friction factors. Following the fin efficiency calculations, the element loop is initialized which iteratively solves the heat transfer and outlet properties for each element. These heat transfer rates are summed to obtain the total circuit and evaporator heat transfer rates. Figure 13 gives a summary of the simulation program logic.

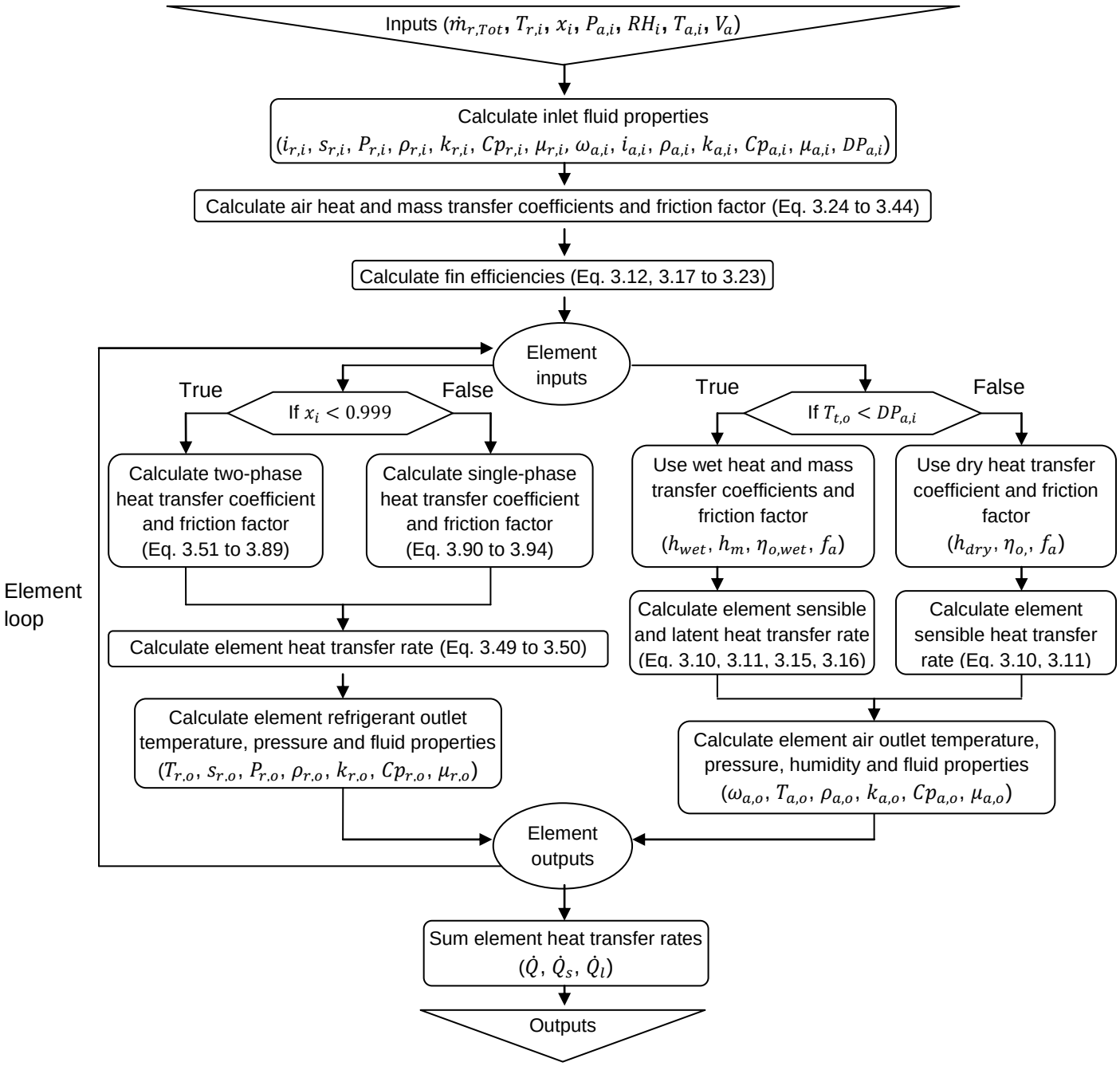

Figure 13: Schematic of the simulation model logic.

4.7. Output

The output of the simulation model includes the outlet refrigerant properties, outlet air properties and the total heat transfer rates. It also gives the air temperature and humidity distribution throughout the circuit as well as the refrigerant temperature and pressure distribution. In order to obtain the heat transfer rates for the total circuit, the heat transfer rates for the individual elements are added together. In addition, to obtain the refrigerant side circuit and consequently the evaporator outlet, the outlet refrigerant temperature and pressure of element 32 are taken. Since elements 1 to 8 and 16 to 24 are situated at the back of the circuit, their outlet air temperatures, relative humidities and pressures are averaged to obtain the airside circuit and consequently the evaporator air outlet.

4.8. Summary

All the aspects of the simulation model were discussed. The geometry of the simulated heat exchanger was given as well as the inputs and outputs of the simulation model. In order to simulate the conditions for the verification and validation, as discussed in Chapter 6, only the refrigerant and air inlet boundary values are changed.

In the next chapter, the experimental aspects are discussed along with the gathering of experimental data. This data is then used in Chapter 6 to validate the simulation model.

CHAPTER 5:
Experimental Study

This chapter discusses the experimental component of the study, which was used for the validation of the simulation model. The discussion will be divided into the following topics:

- History of the test facility.
- Upgrade of test facility.
- Experimental procedure.
- Energy balance and outlet air adjustment.
- Uncertainty analysis.

5.1. History of the test facility

The test bench was built in 2010 at the NWU to undertake studies regarding CO_2 as refrigerant. A tube-in-tube heat exchanger was used as the condenser to transfer energy from the CO_2 to water. The evaporator was also a tube-in-tube heat exchanger using water as the heat source. A compressor and expansion valve completed the vapour compression cycle. Twenty temperature sensors measuring on both of the watersides and the CO_2 side were installed throughout the cycle. Digital sensors as well as analogue gauges, on both sides of the expansion valve, were used to measure the gas cooler outlet and evaporator inlet CO_2 pressures respectively.

In 2011, the test bench was upgraded to accommodate research on CO_2 correlations, both in the evaporator and gas cooler respectively. A Coriolis mass flow meter was installed to measure the CO_2 mass flow rate entering the expansion valve. Two electromagnetic volume flow meters were added to the watersides of both the condenser and evaporator. The temperature sensors installed during 2010 were moved to only measure on the watersides at an increased number of points along the cycle. Sensors, that are more accurate, were added to measure the CO_2 temperatures throughout, as well as the water inlet and outlet temperatures of each heat exchanger. In addition, five high- and low-pressure sensors were installed to measure CO_2 pressure at various points in the gas cooler and evaporator.

In addition, a data acquisition system, to record the various sensor values and to deliver a time-based data export was installed. A variable speed drive was also installed to control the compressor by varying its frequency and thus altering its speed. This was included to accurately control the CO_2 mass flow rate. Three sight glasses were installed, positioned at the outlet of the gas cooler, inlet of the evaporator and at the inlet of the compressor to visually verify the phase of the CO_2 refrigerant.

These components can be seen in Figure 14.

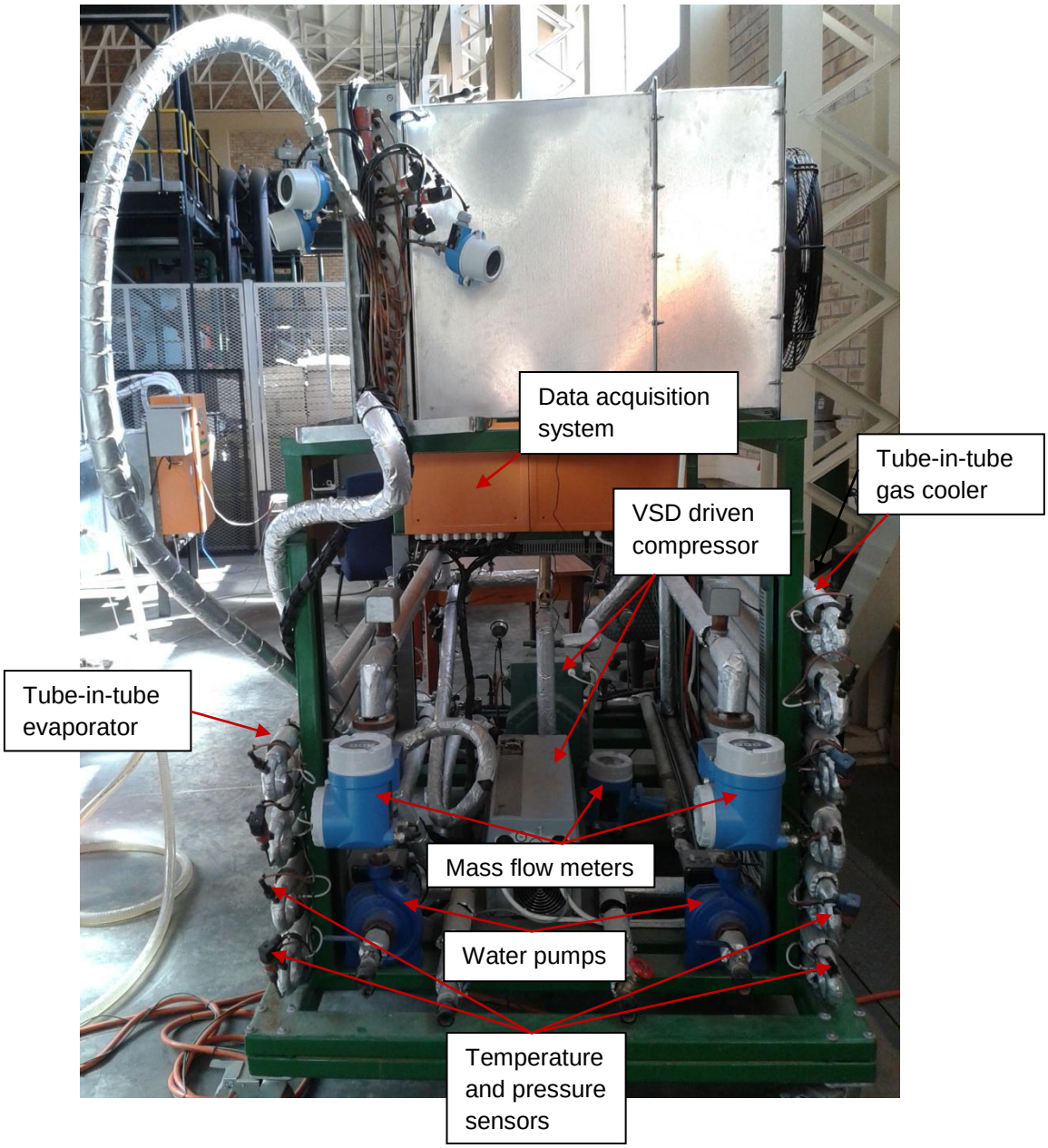

Figure 14: Photo of the test bench showing various components.

5.2. Upgrade of test facility

As mentioned in Chapter 1, the test bench had to be upgraded to include air-to-CO_2 capabilities. To achieve this, a finned coil evaporator was designed to match the cooling capacity of the already installed compressor and physical dimensions of the wind tunnel, described in paragraph 5.2.2. The compressor chart showing the capacity of 32kW is given in Appendix A. Specifications of the finned coil can be found in Appendix B. The finned coil and instrumentation used for the present study is shown in Figure 15.

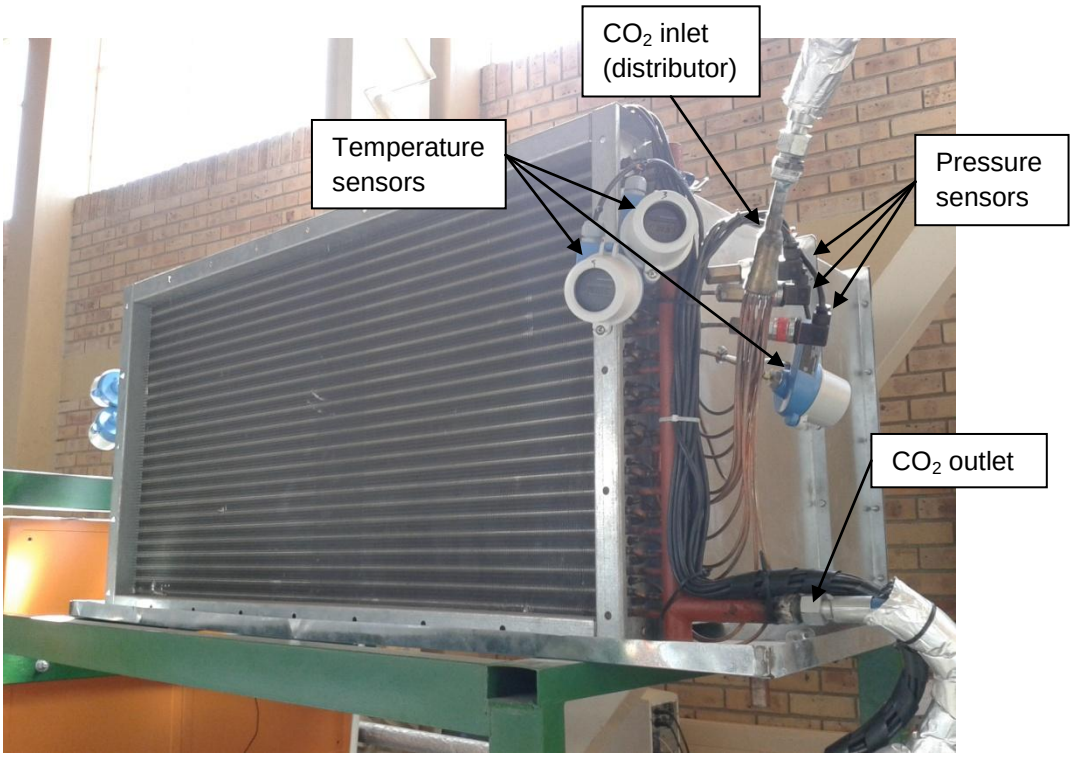

Figure 15: Photo of the installed finned coil evaporator.

5.2.1. Heat pump test facility instrumentation

As mentioned in Chapter 4, only one circuit of the finned coil was fitted with five high accuracy RTD (resistance temperature detector) temperature sensors and five differential pressure sensors. The $5mm$ measuring element is located in the tip of the RTD probe. In an attempt to ensure accurate measurement, the probe is installed with the measuring tip positioned inside the bulk of the CO_2 flow stream. A pressure tapping point was made for the pressure sensors to measure static gauge pressure. Figure 16 shows an illustration of the two ways in which sensors were installed. A schematic layout that indicates the positions of various sensors along the cycle is shown in Figure 17.

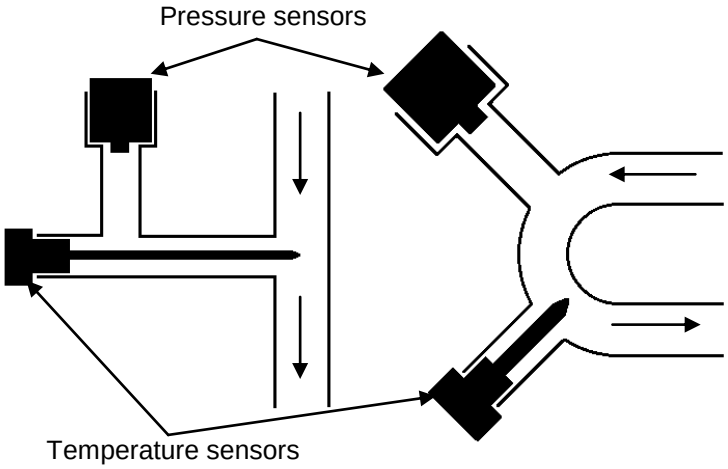

Figure 16: Sensor installation.

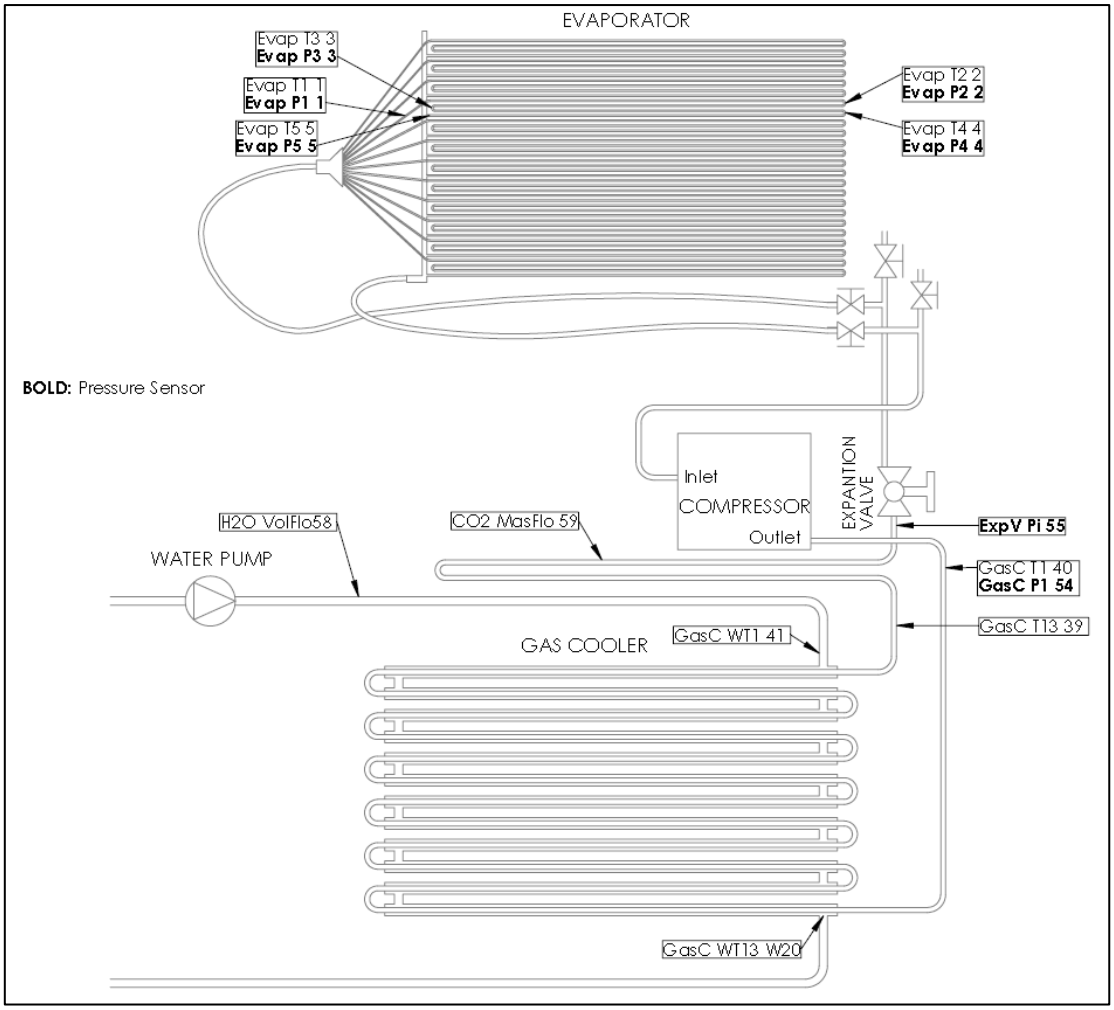

Figure 17: Schematic of the test bench layout indicating various sensor positions.

To obtain the properties of CO_2 at the evaporator inlet, the inlet temperature and vapour quality are needed. However, a temperature and pressure measurement in the two-phase region cannot be used to fix the thermodynamic state since they are singular functions of each other in this region. Therefore, the temperature (GasC T13 39) and pressure (ExpV Pi 55) measurement at the expansion valve inlet (single-phase CO_2 gas) was used to determine the expansion valve inlet enthalpy. With the assumption of constant enthalpy during the expansion process, the temperature measurement at the inlet of the evaporator (Evap T1 1) circuit was used along with the enthalpy to determine the vapour quality. In addition, it was assumed that no significant pressure drop and heat transfer took place through the insulated hydraulic hoses that connect the heat pump test bench to the finned coil evaporator.

The rest of the temperature sensors (Evap T2 2 to Evap T5 5) are used to measure the flow boiling trend up to the evaporator outlet temperature. Also, the five pressure sensors (Evap P1 1 to Evap P5 5) measure the experimental pressure drop from evaporator inlet to outlet.

5.2.2.Wind tunnel instrumentation

As part of another research study at the NWU a wind tunnel was constructed for testing finned coils. The tunnel air flow rate is varied by four fans and includes a return duct to precondition the supply air temperature. Accurate control of air properties are allowed with pre-air heating and cooling capabilities, together with ASHRAE standard pressure, temperature, relative humidity and velocity measurement. An air straightener and diffusers are also installed to ensure a uniform velocity profile across the face area. Figure 18 shows photos of the tunnel layout.

Figure 18: Photos of the coil-testing tunnel at the NWU.

The various air properties are measured before and after the finned coil and the values logged on a separate data logging system. Velocity measurements are done on the principle of a pitot tube with a differential pressure sensor measuring dynamic pressure. This pressure is then converted to velocity as follows (Munson *et al.*, 2010):

$$P_{dyn} = \frac{1}{2}\rho V^2 \tag{5.1}$$

Where, P_{dyn} : Dynamic pressure. $[Pa]$

The air mass flow rate is calculated as:

$$\dot{m} = \rho V A_{ff} \tag{5.2}$$

The air density is evaluated at the inlet air properties.

By connecting the flexible hoses of the pressure sensor to the static pressure ports, the air pressure drop over the finned coil is measured. A Pt 100 RTD element combined with a relative humidity probe is used to measure the air temperature and relative humidity respectively.

Figure 19 gives a schematic that shows the wind tunnel layout.

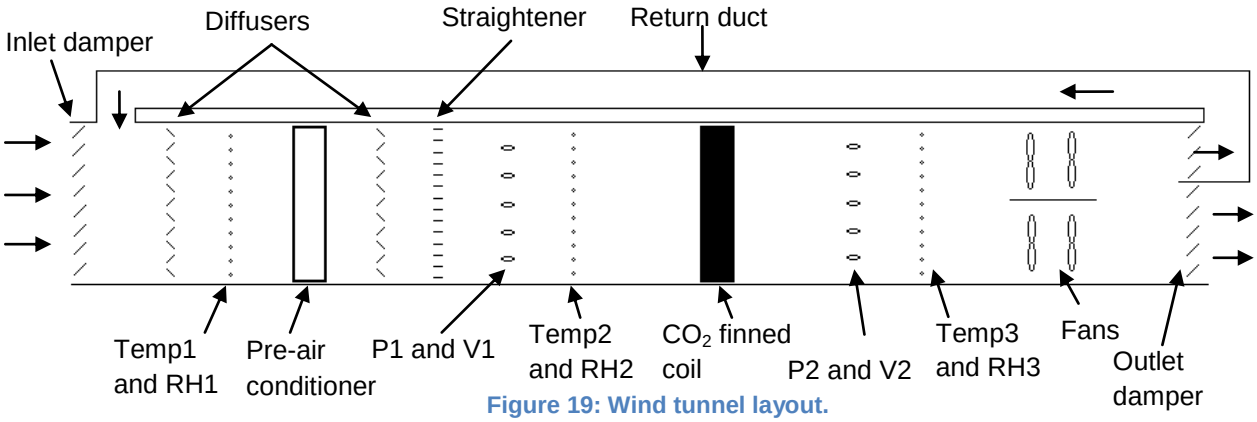

Figure 19: Wind tunnel layout.

To install the evaporator of the heat pump test bench in the wind tunnel, the test bench is equipped with two insulated hydraulic hoses of $3m$ in length. The hoses were selected based on their operating temperature and pressure as well as their compatibility with CO_2. Permeation of CO_2 through the hoses was evaluated and it was found that the amount of CO_2 lost to the environment (less than 100 g per year), within a test period, is negligibly small. The test setup with the hydraulic hoses indicated is given in Figure 20.

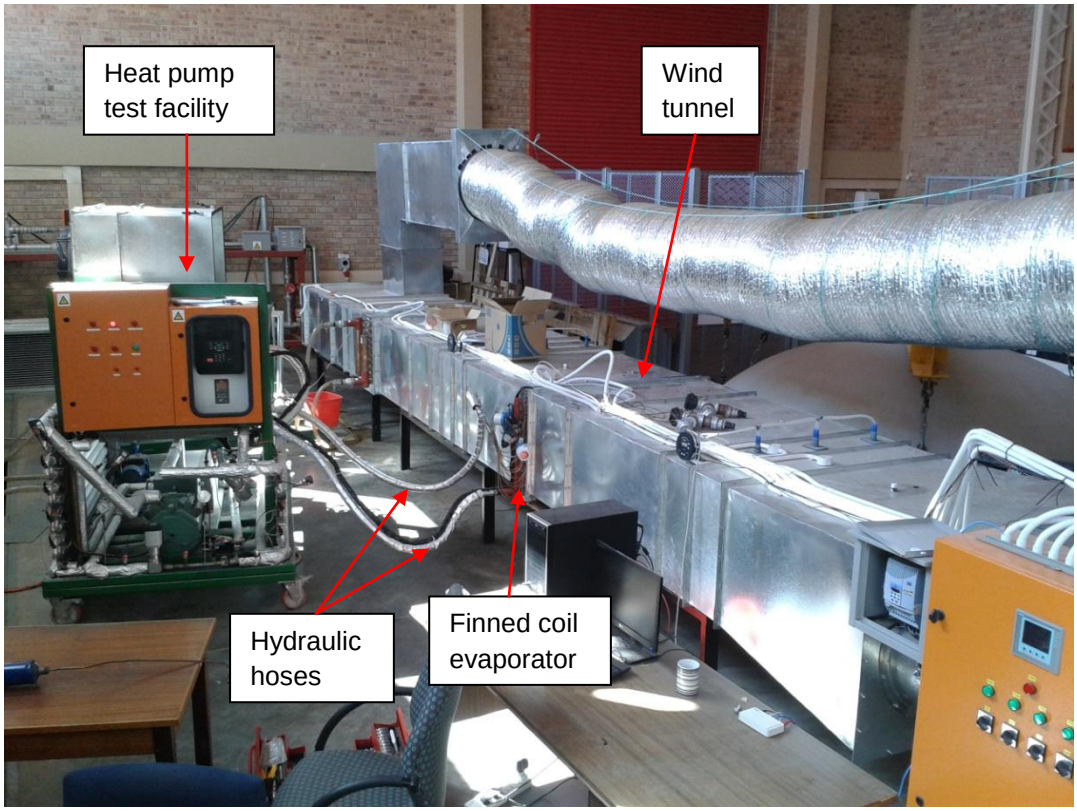

Figure 20: Experimental setup showing the heat pump and finned coil installed inside the wind tunnel.

5.3. Experimental procedure

By controlling various parameters, and systematically checking the evaporating temperature (Evap T1 1) manually, a desired test condition was reached. Once steady state has been observed for at least

three minutes, the next condition was set. After all the conditions have been reached, the data logging system is deactivated and the system shut down. By averaging (obtaining the arithmetic mean) the steady state data, experimental values were obtained. Figure 21 shows the evaporating temperature with the steady state conditions indicated with rectangles.

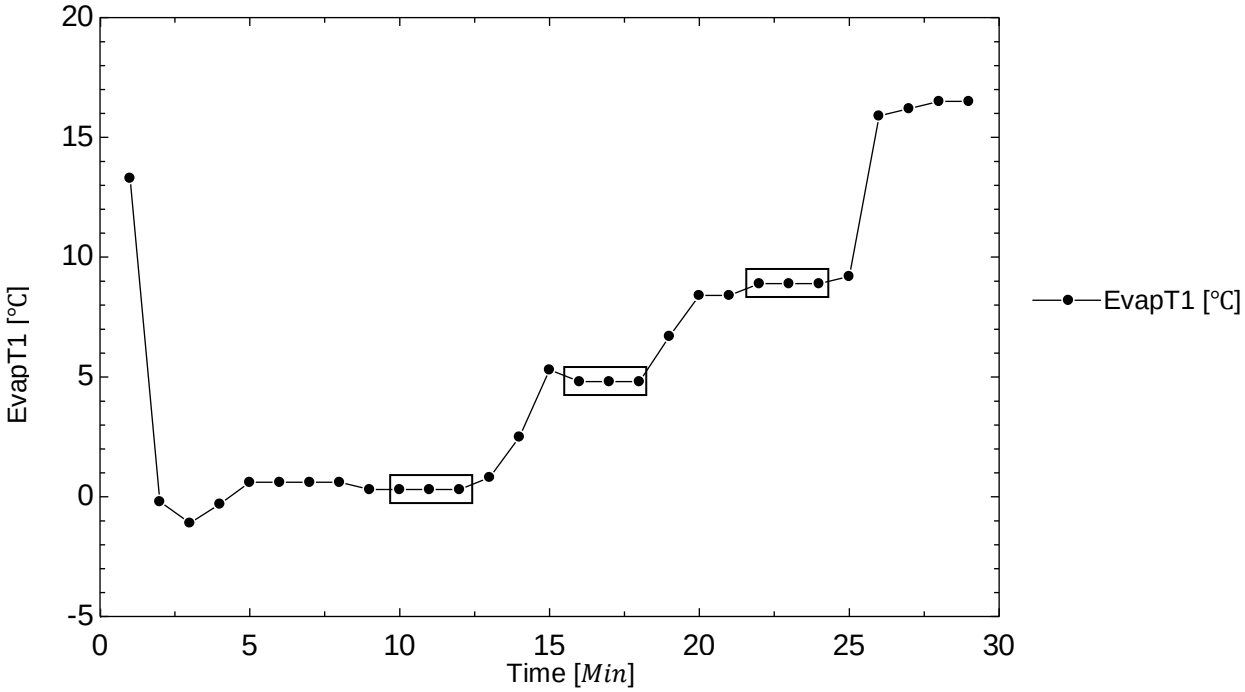

Figure 21: An example of steady state for three test conditions.

5.4. Energy balance and outlet air adjustment

In order to verify the integrity of the experimental setup and the results obtained from it, an energy balance was done for a number of conditions. As can be seen in the fourth column of Table 10, the heat transfer rates on the evaporator's airside, calculated from the measured air properties, are unrealistic.

Table 10: Heat transfer rates and compressor work for three test conditions.

Condition		Gas cooler refrigerant heat transfer rate [W]	Evaporator refrigerant heat transfer rate [W]	Evaporator air heat transfer rate [W]	Compressor work [W]
T_e [°C]	x_i [-]				
0.3	0.8234	15072	8977	67402	6095
4.8	0.8387	15879	9438	79798	6441
8.9	0.928	13645	7137	57733	6508

The compressor is not powerful enough, for the system to deliver the amount of cooling measured on the airside. Therefore, this value is not valid. The difference in gas cooler and evaporator heat transfer rates, gives the compressor work, which correlates satisfactorily with the compressor charts. It was found that the most likely cause was improper measurement by the downstream air sensors (Temp3 and RH3), being wetted by moisture. During the system start-up procedure, a very low evaporating temperature (-10 to -5°C) prevails where dehumidification occurs, during which condensate wets the outlet sensors. Since the simulation model values compared well with EVAP-COND (as discussed in Chapter 6), and the measured values differed from both predictions, it was decided to adjust the outlet dry-bulb temperature.

This was done by using the measured refrigerant heat transfer rate (as it is the most accurate), together with the measured outlet relative humidity, to calculate the outlet dry-bulb temperature. These adjusted values are then used as the experimental outlet air dry-bulb temperatures to compare against the simulation predictions, as will be shown in Chapter 6. The results of the adjustment for three conditions are given in Table 11.

Table 11: Measured and calculated outlet dry-bulb temperature values.

Measured inlet dry-bulb temperature [°C]	Measured outlet dry-bulb temperature [°C]	Calculated outlet dry-bulb temperature [°C]
16.5	4.3	13.1
15.5	8.4	14.2
15.7	11.0	15.3

5.5. Uncertainty analysis

Any experimental measurement contains a degree of uncertainty, as no measurement technique is free of inaccuracies. In order to gain better insight into the integrity of the measured parameters, an uncertainty analysis was done. Only where relevant, the worst-case uncertainty was evaluated. Uncertainties due to the following effects had to be considered (Rousseau *et al.*, 2012):

- Drift.
- Statistical.
- Instrument.

Drift uncertainty is the change in the error made by the measuring instrument, over a long period. Usually, drift uncertainty is specified as a quantity per year.

Statistical uncertainty relates to the precision or repeatability of multiple observations of a measured value. Since the measurement error in each observation falls in an uncertainty band, the statistical probability of the error value has to be considered.

Instrument uncertainty is due to the error made by the measuring principle of the instrument.

The total uncertainty associated with a measured parameter is calculated by combining these three types of uncertainties as follows (Rousseau *et al.*, 2012):

$$u_{tot} = \sqrt{\left(u_{drift}\right)^2 + (u_{stat})^2 + (u_{instr})^2} \tag{5.3}$$

Where:

u_{tot} : Total measurement uncertainty.

u_{drift} : Uncertainty due to drift.

u_{stat} : Uncertainty due to statistical probability of multiple observations.

u_{instr} : Uncertainty due to measurement principle.

Given that the experimental data were logged within an hour, drift uncertainty is neglected. Instrument uncertainty is gathered from the device specification and calibration certificates. These uncertainties are explained later in this chapter. Since the measured values over a time period is averaged to determine a mean experimental value, uncertainty due to statistical probability must be evaluated. The standard uncertainty of the mean was calculated as (Bell, 2001):

$$u_{Stat} = \frac{\sigma}{\sqrt{n}} \tag{5.4}$$

Where:

n : Number of measurements within the averaged time period.

σ : Standard deviation of the measured values.

u_{Stat} : Standard uncertainty of the mean.

The standard deviation of a set of measurement values was calculated as follows (Bell, 2001):

$$\sigma = \sqrt{\frac{\sum_{i=1}^{n}(x_i - \bar{x})^2}{(n-1)}} \tag{5.5}$$

Where:

x_i : ith measurement value.

$\bar{x}$: Arithmetic mean of n measurements.

The experimental heat transfer as well as the inlet vapour quality was derived from the measured temperature, pressure and mass flow rate values; hence, the total measurement uncertainty propagates through the calculation. Thus, in order to determine the uncertainty of the derived parameters the following uncertainty propagation is used (Rousseau *et al.*, 2012):

$$u\big(y(x_1, x_2, \dots, x_n)\big) = \sqrt{\sum_{i=1}^{n}\big(c_{xi}u_{tot}(x_i)\big)^2} \tag{5.6}$$

Where:

$c_{xi} = \frac{\partial y}{\partial xi}$: Sensitivity factor.

y : Derived parameter.

$(x_1, x_2, \dots, x_n)$: Measured parameters.

EES has a built-in uncertainty propagation function, which is used to determine the various uncertainty values for the derived parameters. An uncertainty propagation for the refrigerant heat transfer rate, measured in condition one (see section 6.1), was done by hand in appendix C to confirm the accuracy of the EES uncertainty results. A standard uncertainty of ±759.65W was calculated by hand while the EES calculation gives ±759.655W. Hence, the error made by using the EES function is in the order of 0.005W (±0.000658%).

5.5.1. Refrigerant side instrumentation

The temperature sensors from Figure 17, Evap T1 1 to Evap T5 5, have a measuring element with a known temperature-resistance (electrical) relationship. Measuring this resistance, is a transmitter head that converts the resistance into a 4-20mA signal in an active loop containing a 250Ω resistor. The data logging system measures the electrical potential difference over the resistor and determines the temperature value with a user specified linear relationship.

The temperature sensor from Figure 17, GasC T13 39, also has a measuring element with a known temperature-resistance (electrical) relationship. However, the data logging system directly measures this resistance and determines the temperature value with a user specified linear relationship.

A potential difference is measured by the data logging system from the ratio metric pressure sensors in Figure 17, Evap P1 1 to Evap P5 5 and ExpV Pi 55. The ratio of the measured value to the input value determines the pressure value.

The controlled generation of Coriolis forces and a measurement of phase shift, caused by mass flow through the gas flow meter, are used to generate a 4-20mA signal in a passive loop containing a 250 Ω resistor. As mentioned above, the data logging system measures the electrical potential difference over the resistor and determines the mass flow rate value with a user specified linear relationship.

In all cases, the data logging system resolution rounds the measured value to one decimal point. Given that the uncertainty for any device is based on a certain confidence limit, all uncertainties have to be converted to a standard uncertainty (equal to one standard deviation) before combining with statistical uncertainty, as described above. Where the coverage factor or distribution is not known, a rectangular distribution is assumed and the reported uncertainty divided by $\sqrt{3}$. The results of this, is given in column four of Table 12.

Table 12: Refrigerant side device uncertainties converted to standard uncertainties.

Device	Uncertainty (±)	Divisor	Standard uncertainty (±)
Pt 100 RTD With transmitter head (Evap T1 1 to Evap T5 5)	0.025°C	2	0.012°C
Pt 100 RTD Transmitter head signal output	2μA	$\sqrt{3}$	1.15μA
250Ω Resistor (For temperature measurement)	0.025Ω	2	0.012Ω
250Ω Resistor (For mass flow measurement)	2.5Ω	2	1.25Ω
Pt 1000 RTD (DIN EN 60751 Class B) (GasC T13 39)	(0.3+0.005*T)[a]	$\sqrt{3}$	(0.17+0.002*T)[a]
Ratiometric pressure sensor (Evap P1 1 to Evap P5 5)	0.8Bar	$\sqrt{3}$	0.46Bar
Ratiometric pressure sensor (ExpV Pi 55)	1.28Bar	$\sqrt{3}$	0.73Bar
Coriolis flow meter (CO2 MasFlo 59)	0.15%o.r.[b]	2	0.075%o.r.[b]
Coriolis flow meter output signal	0.5μA	$\sqrt{3}$	0.28μA
Logging system potential difference measurement	4mV	$\sqrt{3}$	2.3mV
Logging system resistance measurement	0.4Ω	$\sqrt{3}$	0.23Ω
Logging system temperature resolution	0.05°C	$\sqrt{3}$	0.028°C
Logging system pressure resolution	0.05Bar	$\sqrt{3}$	0.028Bar
Logging system mass flow rate resolution	0.00005kg/s	$\sqrt{3}$	0.000028kg/s

a - T is the measured temperature value in °C
b - o.r. is the mass flow reading in kg/s

5.5.2. Airside instrumentation

Air dry-bulb temperature measurement, Temp1 to Temp3, also have a measuring element with a known temperature-resistance (electrical) relationship. This resistance is measured by the air data logging system and converted to a temperature with a manufacturer specified linear relationship.

The relative humidity probe contains a Hygrosmart sensor, which measures the dielectric constant of a material as it varies with humidity. This measurement is then converted to a 0-10V signal by the probe. Again the logging system calculates a relative humidity value with a user specified linear relationship.

A pressure differential measurement is converted to a 4-20mA signal in an active loop with a 510Ω resistor. Again, the logging system measures the potential difference over the resistor and uses a user specified linear relationship to determine the pressure differential value. All airside device uncertainties are given in Table 13.

Table 13: Airside device uncertainties converted to standard uncertainty.

Device	Uncertainty (±)	Divisor	Standard uncertainty (±)
Hygrosmart relative humidity sensor/converter (RH1 to RH3)	2%	$\sqrt{3}$	1.15%
Pt 100 RTD element (DIN EN 60751 Class A) (Temp1 to Temp3)	0.2°C	$\sqrt{3}$	0.11°C
Differential pressure sensor (P1 and P2)	0.6Pa	$\sqrt{3}$	0.34Pa
510Ω Resistor	25.5Ω	2	12.75Ω
Logging system potential difference measurement	0.1%	$\sqrt{3}$	0.057%
Logging system resistance/temperature measurement	0.5°C	$\sqrt{3}$	0.28°C
Logging system temperature resolution	0.05°C	$\sqrt{3}$	0.028°C
Logging system relative humidity resolution	0.05%	$\sqrt{3}$	0.028%
Logging system pressure resolution	0.05Pa	$\sqrt{3}$	0.028Pa

Since not all the relations mentioned above are known, uniformity in propagation of uncertainty from measuring element to the logged value is very hard to achieve. To simplify the uncertainty analysis process, whenever the measuring element uncertainty is smaller than the logging system resolution uncertainty, the later will be taken as the instrument uncertainty, u_{instr}, and vice versa.

It should be noted that all the airside instrumentation as well as the evaporator temperature sensors have been calibrated to their individual standards, therefore confidence in the reported instrument uncertainties are established.

5.6. Summary

The experimental facility was described along with the testing procedures. An uncertainty analysis of all the sensors was done.

The next chapter discusses the results of the above experimental work and uncertainty analysis. These experimental results were also used to validate the simulation model, along with verification with EVAP-COND.

CHAPTER 6:
Results and Comparisons

In this chapter, a comparison of the simulation model's predictions with those from EVAP-COND is used to verify the model. Furthermore, simulation model predictions are compared with experimental data in order to validate the model. This chapter will discuss the results in detail under the following headings:

- Verification and validation.
- Predictions at higher inlet relative humidity values.

In order to determine an acceptable margin of comparison, the accuracies of the correlations used by the present simulation model were considered. Wang *et al.* (2002) reported that their correlation is able to predict 91% of the heat transfer data they evaluated, to within ±15% and 85% of their pressure drop data to within ±15%. Cheng *et al.* (2008a&b) reported that their correlation is able to predict 71.4% of the heat transfer data they evaluated, within ±30%, while 81.5% of the pressure drop data could be predicted to within ±30%. Both authors termed these margins as good agreement. In the light of this, a margin of ±20% difference between the present simulation and EVAP-COND values, as well as between the present simulation and the experimental data, for all data points, was adopted.

6.1. Verification and validation

Through the execution of the experimental procedure, described in the previous chapter, data for six experimental conditions were obtained. These conditions were then simulated in the present model as well as the simulation package EVAP-COND.

EVAP-COND is a software package, developed by NIST that is used to simulate finned coil evaporators and condensers (NIST, 2003). The option, to specify the refrigerant evaporation heat transfer correlation from either Jung & Didion, 1989 or Thome, 2005 was used to select the latter, since it was the most recent. The available air correlations are those developed by C.C. Wang from 1999 to 2001. For wavy fins, the Wang, 1999 correlation was used (Domanski, 1999).

As mentioned previously, in the present simulation model, Cheng *et al.* (2008a&b) were used as refrigerant correlations which uses an updated flow pattern map from the Thome, 2005 correlation with a considerable amount of additional experimental work and data. Most of these updates were specific to the range of operating conditions typically found in finned coil evaporators. In addition, on the airside, the correlation by Wang *et al.* (2002), as used in the present model, is a refinement of the correlation proposed by Wang, 1999.

The comparison of the results from the present simulation, EVAP-COND and the experimental measurements verifies and validates the developed simulation model. In all cases, the simulation model is discussed when firstly compared to EVAP-COND and secondly to the experimental values.

On the refrigerant side, heat flux is one of the most prominent properties that influence the heat transfer coefficient. It was decided to vary both the evaporating and inlet dry-bulb temperatures within the limitations of the test bench and wind tunnel test facility. This resulted in different heat transfer rates and consequently heat flux values. However, heat exchanger geometry mostly influences the heat transfer coefficient on the airside, which does not vary within the scope of this study. Thus, it was decided to vary the air velocity, thereby changing the air mass flow rate. The wind tunnel test facility was not equipped to vary inlet relative humidity. The variations that did exist, originated from the change in ambient air relative humidity during the test period. Table 14 gives the six experimental conditions.

Table 14: Experimental conditions with their associated uncertainties.

Case	Refrigerant inlet conditions			Air inlet conditions		
	$T_{r,i}$ [℃]	x_i [-]	$\dot{m}_r$ $[kg/s]$	$T_{a,i}$ [℃]	RH_i [%]	V_a $[m/s]$
1	0.3±0.028	0.823±0.0230	0.1435±0.00011	16.5±0.11	34.8±1.15	5.25±0.064
2	4.8±0.028	0.838±0.0210	0.1705±0.00013	15.6±0.11	35.8±1.15	9.71±0.035
3	8.9±0.028	0.928±0.0190	0.2204±0.00017	15.7±0.11	35.3±1.15	9.61±0.035
4	0.0±0.028	0.429±0.0110	0.1662±0.00013	29.1±0.11	30.1±1.15	8.95±0.044
5	5.0±0.028	0.429±0.0091	0.2039±0.00015	29.4±0.11	30.4±1.15	8.94±0.042
6	9.1±0.028	0.482±0.0120	0.2489±0.00019	29.8±0.11	26.9±1.15	10.64±0.038

6.1.1. Overall heat transfer rate

The experimental heat transfer rates were calculated from the experimental values measured on the CO_2 side as discussed in the previous chapter. These values with their uncertainties are compared to the simulated heat transfer rate values of both models for the six conditions in Figure 22.

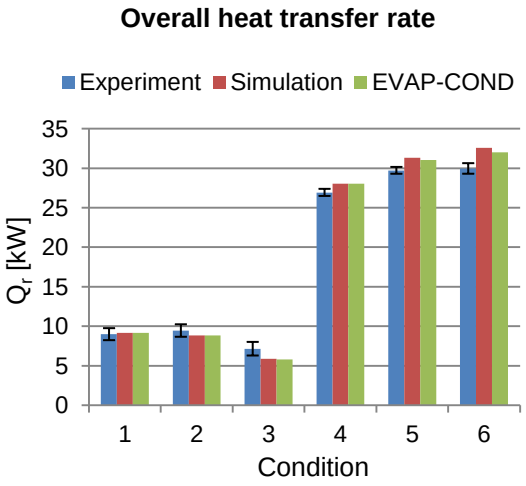

Figure 22: Experimental and simulated heat transfer rates for the six conditions.

— Comparison with EVAP-COND.

Figure 22, shows that the heat transfer rate of the present simulation compares well with that from EVAP-COND. The largest difference occurred in condition six where the present simulation predicted a value 1.7% higher than EVAP-COND (using EVAP-COND as reference). This was attributed to the present simulation using an updated refrigerant two-phase heat transfer coefficient correlation as mentioned above. Some of the favourable attributes of CO_2 have not yet been fully correlated. By adding to the original base data of the correlation (specifically in the regions typically found in finned coil evaporators), the correlation could be updated to more accurately predict heat transfer coefficients in the same range. These coefficients are in general higher than that predicted by the previous correlation, which follows the trend in CO_2 heat transfer coefficient correlations as found in literature.

It should be noted here that in conditions five and six, EVAP-COND did predict heat transfer rate values closer to the experimental value. The general trend in literature shows that an increase in accuracy usually results in the prediction of a higher value, which could explain this observation.

However, the experimental value were influenced by lubricant that degraded the experimental heat transfer coefficient and will be discussed shortly. Neither EVAP-COND nor the developed simulation includes the effect of lubricant. Thus, it is coincidental that a lower prediction in heat transfer coefficient by EVAP-COND (because of the correlation) predicted heat transfer rates closer to the experimental. A more detailed investigation in section 6.1.2, will show that the correlation used in the present simulation is in fact more accurate for these conditions than the one used by EVAP-COND.

Hence, the slightly higher heat transfer rate predictions were attributed to the higher two-phase heat transfer coefficients used in the present simulation model. The largest influence was seen in the condition where the largest two-phase region was present (from Figure 24 below, condition six has 2.4m of two-phase flow).

— Comparison with experimental.

In both conditions one and two, the simulated heat transfer rate fell within the experimental uncertainty bands, while in condition three; the simulation slightly under predicted the experimental value. This may be caused by an increased wetted area inside the tubes due to lubricant foam, which will be discussed later. Much lower vapour qualities (0.429 to 0.482) were present in conditions four, five and six, than in conditions one, two and three (0.823 to 0.928). Hence, a larger two-phase region was present. In these conditions, the simulated heat transfer rates were over predicted. The largest over prediction of 8.7% occurred in condition six. This may be attributed to the following:

- *Refrigerant correlation range*: As mentioned in Chapter 2, the accuracy of heat transfer and pressure drop correlations degrades significantly when applied to conditions outside the range of their base data. Thus, the experimental conditions might fall outside the range of the correlation by Cheng *et al.* (2008a&b), used in the present simulation.
- *Lubricant affecting two-phase heat transfer*: Also discussed in Chapter 2, lubricant in the system might affect the heat transfer processes in the evaporator, which may increase or decrease heat transfer coefficients.
- *Lubricant foam through sudden expansion*: It is possible, that large quantities of lubricant will foam due to a rapid expansion at high pressure ratios, resulting in the degradation of heat transfer in the two-phase or superheat region.

Considering these possibilities, it can also be stated that the present simulation may simply just over predict the heat transfer rates in these conditions.

Despite the discrepancies, the present simulation model was still able to satisfactorily predict all the measured refrigerant temperatures throughout the finned coil for all conditions. Figure 23 compares the experimental and simulated refrigerant temperature values.

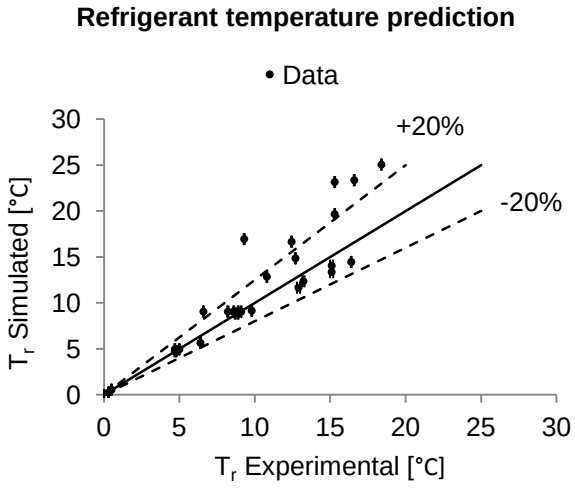

Figure 23: Experimental refrigerant temperature versus simulated refrigerant temperature.

The simulation model predicted 70% of the measured experimental refrigerant temperature data within ±20%.

6.1.2. Refrigerant temperature trend

In vapour compression heat pump cycles, the saturation point is very important in the design of finned coil evaporators. Therefore, the trend in refrigerant temperatures with respect to distance from the evaporator inlet, are given for all conditions in Figure 24. Since two-phase evaporation takes place at constant temperature, the saturation point is identified as the instance where the first increase in temperature occurs. For the EVAP-COND and experimental data, the saturation point lies somewhere between the last point of constant temperature and the first point above that temperature, as it is not a clearly indicated output from the software and since only the inlet and outlet temperatures of each tube are measured.

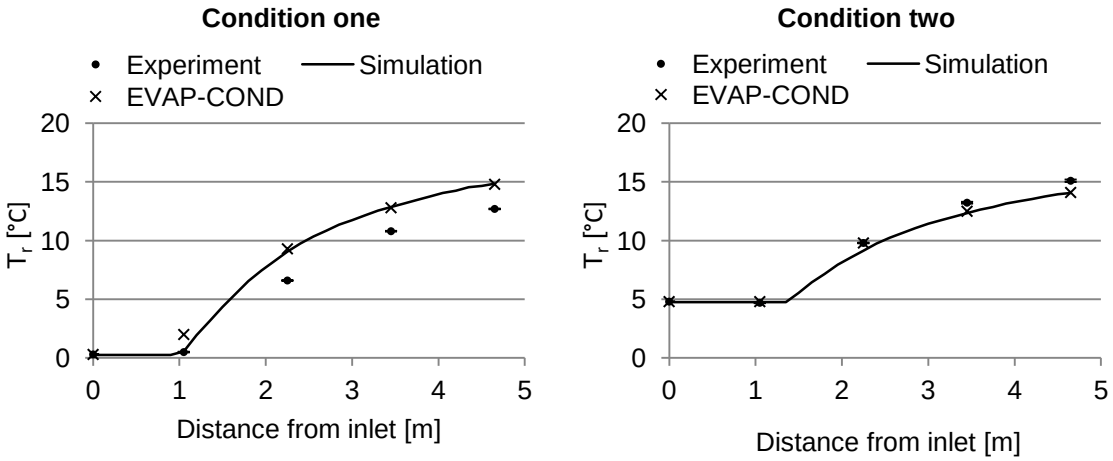

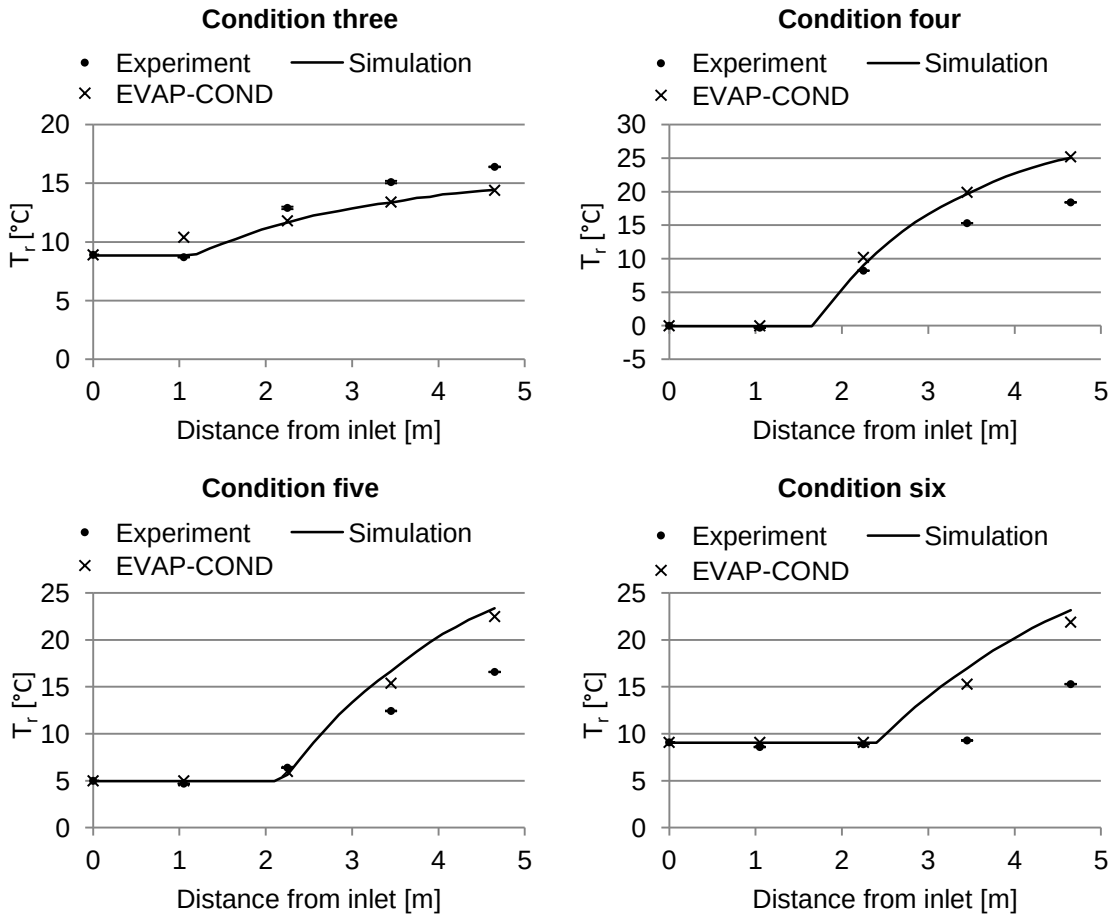

Figure 24: Refrigerant temperature trends simulated by the present simulation and EVAP-COND.

— Comparison with EVAP-COND.

In conditions one and three, the present simulation more accurately predicted the saturation point than EVAP-COND. This is because some of the main updates done by Cheng *et al.* (2008b) were in the dryout and mist flow regions, since these regimes are typically dominant in finned coil evaporators. Again, it is clear that a larger two-phase region constitutes a higher heat transfer rate, which results in higher refrigerant temperatures.

— Comparison with experimental.

As can be seen from Figure 24, the superheat region's temperatures, and consequently heat transfer coefficients, were over predicted by the simulation in conditions four, five and six, if the experimental values are taken as the reference. The largest over prediction in outlet refrigerant temperature was 51% in condition six (which corresponds to a 3.5% difference in outlet refrigerant enthalpy). This was attributed to lubricant foam degrading heat transfer coefficient to be discussed in the following section. Thus, the discrepancy of 51% is due to the experimental measurements and not the inaccuracy of the simulation. However, with the exception of condition six, the saturation point was accurately predicted for all conditions to occur in the same tube as derived from the measurements.

6.1.3. Discussion of heat transfer rate over prediction

Firstly, as reported in Chapter 2 the Cheng *et al.* (2008b) correlation ranged from 1800 to 46000W/m^2 compared to the average heat flux in the six experimental conditions ranging from 6852 to 33096 W/m^2. It is clear that the correlation range is applicable. The correlation mass flux range of 50 to 1500kg/m^2 , also covered the experimental range from 176 to 306kg/m^2. However, only three

of the thirteen data sets correlated by Cheng *et al.* (2008b), made use of an inner tube diameter of larger than 3mm. The closest of which was that of Knudsen & Jensen at 10.06mm, where most of their data were gathered at very low saturation temperatures as well as low heat and mass flux values.

Thus, because the correlated data had been largely based on smaller tube diameters, the two-phase heat transfer coefficient prediction for the larger diameter of the present study may have been inaccurate. The correlation used for the superheat region was general and have been extensively proven for the experimental ranges of the present study. It is however evident, from the temperature trend graphs, that whenever a larger two-phase region was present, the heat transfer coefficients in the superheated region were over predicted.

Not only CO_2 but also compressor lubricant was present in the system. The heat transfer processes and flow regimes in the two-phase region are influenced by the presence of lubricant. As mentioned in Chapter 2, the presence of lubricant can increase or decrease the heat transfer coefficient and the effects are very complex to simulate. It has however been reported that a lubricant foam forms at the interface between the liquid and gas phases at high heat fluxes and lubricant concentrations (Wang *et al.*, 2012). This foam increases the wetted area of the heat transfer surface, and therefore can increase the two-phase heat transfer coefficient (Shen & Groll, 2005).

In addition, the compressor manufacturer reported that a sudden drop in pressure, such as through the expansion valve, may cause the POE lubricant to foam (Bitzer, 2011). After completion of the experimental study it was determined that the compressor used had been over-filled with lubricant according to the manufacturer's specifications. This contributed to the high concentration of lubricant in the system.

Compounded by the fact that higher pressure ratios and average two-phase heat flux values (average of all the simulated two-phase elements - Table 15) were present in conditions four, five and six, it can be concluded that the formation of lubricant foam in these conditions was highly probable.

Table 15: Expansion valve pressure ratios and average two-phase heat flux values.

Condition	Pressure ratio [-]	Average two-phase Heat flux [W/m^2]
1	2.18	14027
2	1.96	10762
3	1.69	6852
4	2.39	33096
5	2.36	30150
6	2.25	28187

In condition six, the simulated saturation point occurred in a tube earlier than in the experimental measurement. It is possible that the lubricant foam influenced the fourth temperature measurement, which was still at the lower evaporating temperature. The two-phase refrigerant temperature trend was therefore adequately simulated. However, as also mentioned above, the superheated region had a lower heat transfer coefficient than that was simulated, which resulted in lower refrigerant temperatures.

During testing, white foam was periodically observed through a sight glass just before the compressor inlet. It can therefore be concluded that the expansion together with the flow boiling regimes in the two-phase region, created lubricant foam that was transported throughout the superheated region of the evaporator. This foam had degraded the heat transfer coefficient in the superheat region. The effect was much less pronounced in the higher quality data because a very small two-phase region and pressure ratio were present, thus very little or no lubricant foam had been generated.

Different methods of handling lubricant in heat transfer simulations have been proposed in the open literature. The simplest of which is to use a degradation factor (Zhao & Bansal, 2009) applied to the heat transfer coefficient. A modified simulation model, implementing a degradation factor was created and used to simulate conditions four, five and six, which will be discussed below.

6.1.4.Modified simulation

A degradation factor to account for the effects of lubricant foam was calculated for each one of the three conditions mentioned above, so that their outlet refrigerant temperature falls within one percentage of the experimental value. The average of these factors was calculated to be 0.36. Thus the heat transfer coefficient value, may be reduced to around 36% of the value predicted by the correlation. This factor was implemented in a modified simulation model to simulate the three conditions as shown in Figure 25.

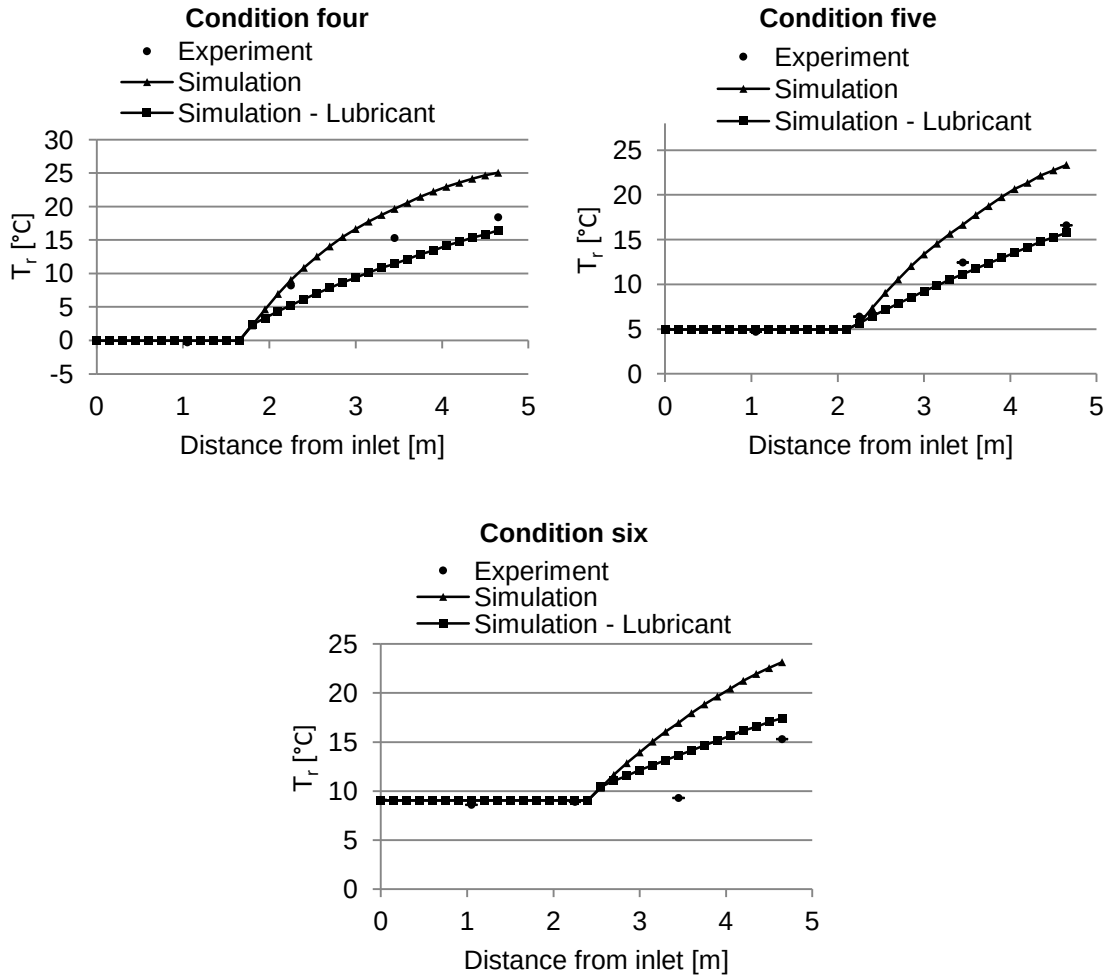

Figure 25: Refrigerant temperature trend predicted by the modified simulation.

Figure 25, demonstrates that the influence of lubricant foam is complex and cannot be accurately modelled by applying a universal constant degradation factor such as the one proposed. However, the accuracy of outlet refrigerant temperature prediction was increased considerably. The difference in the new predicted outlet values to those measured were 11%, 5% and 14% for the respective conditions.

The inclusion of lubricant in the system should be modelled by defining new CO_2-lubricant mixtures. Thus, as a recommendation for future studies, new empirical heat transfer coefficient and pressure drop correlations must be developed.

6.1.5. Refrigerant Pressure trend

Since the two-phase evaporation process occurs at a constant temperature, and the fact that temperature and pressure are singular functions of each other, in this region, a significant pressure drop may influence the heat transfer process.

For example, instrumentation on most industrial systems only measure inlet and outlet refrigerant properties. Thus, in some conditions, a large two-phase pressure drop and large superheat may have nearly the same outlet measurement as a small two-phase pressure drop and small superheat. Hence, the accurate simulation of the pressure trend is important.

Because of the large uncertainties in the pressure measurements, the very small pressure drop values could not be adequately evaluated. Hence, the trend in simulated pressure values were compared with the experimentally measured absolute pressure values throughout the circuit as well as the predictions by EVAP-COND. Figure 26 shows that the simulated pressure trend in the first three conditions, passed through all the measurement uncertainty bands. However, in conditions four, five and six, the simulated trend passed over the uncertainty band of the second sensor, positioned 1.05m from the inlet.

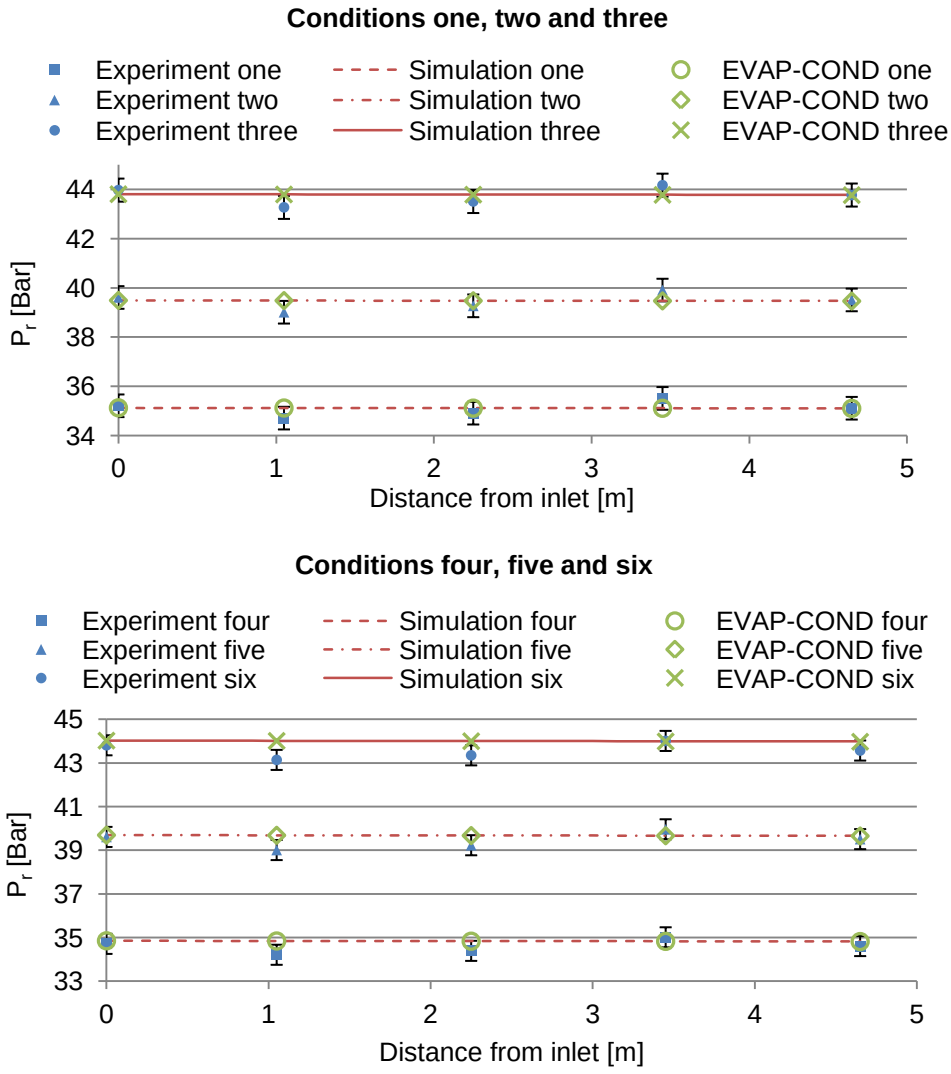

Figure 26: Experimental and simulated refrigerant pressure trends.

— Comparison with EVAP-COND.

The simulated pressure trend closely matched that of EVAP-COND where early on in the two-phase region; the simulation predicted slightly lower pressure values while later on, in the superheat region, slightly higher pressure values. This observation holds true for all conditions. Figure 27 serves as a better illustration with a more detailed view of condition one. The experimental data were left out in order to magnify the pressure axis to ensure that the differences can easily be seen.

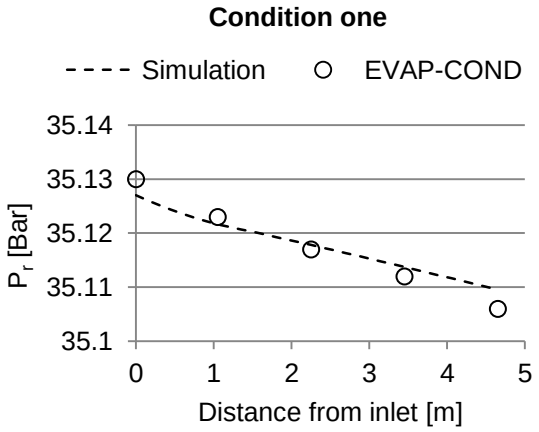

Figure 27: Simulated refrigerant pressure trends for condition one.

As mentioned, the favourable aspects of CO_2, including very low pressure drops, had not yet been very accurately correlated by the correlation used in EVAP-COND. The larger pressure values in the superheat region were accredited to the Filonenko, 1954 correlation, predicting higher friction factors than the Petukov correlation.

— Comparison with experimental.

Closer inspection of Figure 26 shows that the inlet pressure of the simulation and the first sensor (at $0m$) were not exactly equal. This is because the simulation used the temperature and vapour quality, as given in Table 14, to determine the pressure with the built-in fluid property data in EES. Thus, the measured absolute pressure may have differed. In the first three conditions, the inlet simulation pressure were lower than the measured pressure by $0.086Bar$, $0.227Bar$ and $0.167Bar$ respectively, while in the last three conditions, the inlet simulation pressure were higher than the measured pressure by $0.137Bar$, $0.08Bar$ and $0.212Bar$ respectively.

The variation in measured pressure values for a single condition followed the same trend as for the other conditions. This suggests that the variation was not caused by the experimental condition but rather by a constant sensor property throughout the experimental conditions. The calibration of the zero point may also have differed between the five sensors, which with consideration of the sensor uncertainty, were quite good.

In spite of the above-mentioned aspects, the pressure trend was adequately simulated with the largest difference being 2.02%.

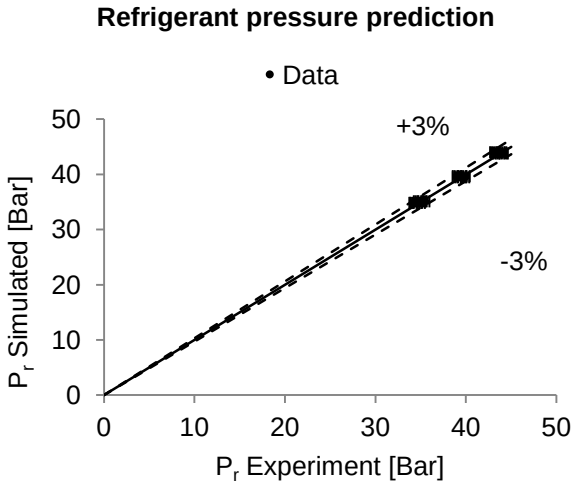

Figure 28: Experimental refrigerant pressure versus simulated refrigerant pressure.

From Figure 28, it is clear that the simulation model was able to predict 100% of the experimental refrigerant pressure data to within ±3%.

6.1.6. Sensible and latent heat transfer rates

Since the experimental sensible and latent heat transfer rates were determined from the airside measurements, their values may have been inaccurate due to improper outlet air measurements. As discussed in Chapter 5, it is possible that condensate droplets did wet the outlet sensors, and an adjustment was made to the outlet dry-bulb temperature measurement. However, this adjustment still included the original relative humidity measurement.

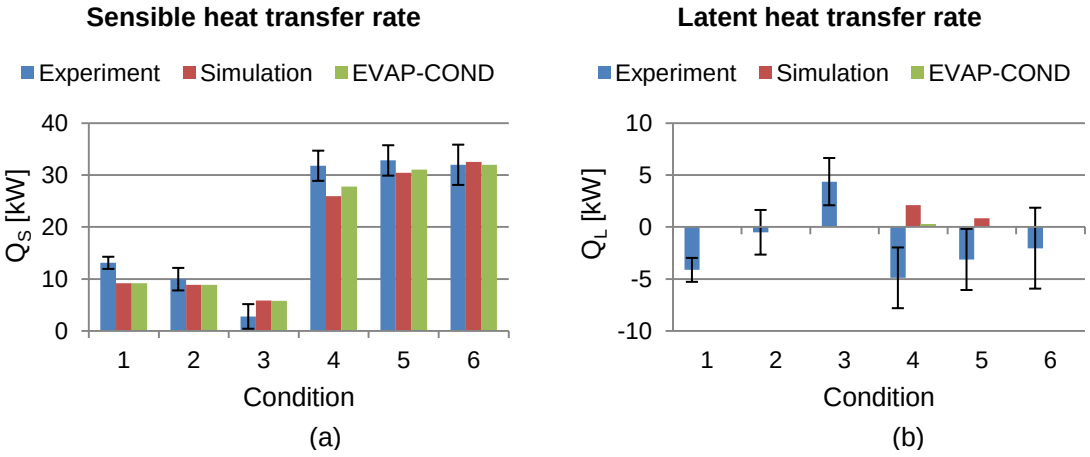

Figure 29: Experimental (a) sensible and (b) latent heat transfer rates, compared to the present model and EVAP-COND.

— Comparison with EVAP-COND.

The largest difference in sensible heat transfer rate was found in condition four (6.5%). This condition also had the largest latent heat transfer rate and consequently mass transfer coefficient, which was calculated using the Lewis number. The difference was attributed to the fact that EVAP-COND uses a constant value for the Lewis number where the present simulation model uses a correlation, as mentioned in section 3.2.4.

Comparison with experimental.

Figure 29a illustrates that in conditions two, five and six, the sensible heat transfer rate was simulated to within the experimental uncertainty bands. Conditions one and four were under predicted (30% and 18% respectively) while condition three had been over predicted (112%). Thus the value predicted by the present simulation is 112% (of the absolute experimental value) higher than the absolute experimental value. This percentage would seem extremely high but considering the very small absolute values, the relative difference is not that extreme.

Also, Figure 29b shows a negative latent heat transfer component for most of the experimental conditions, which is unrealistic. This further suggests that the, still present, outlet relative humidity measurement skewed the airside heat transfer rate results. However, considering the relatively small latent heat transfer values and the large associated experimental uncertainties, the latent heat transfer data was disregarded. Also, no further effort was made to correct this measurement, although a recommendation is given in Chapter 7.

It is clear that the outlet air measurements were flawed by condensation and considering the large uncertainties in the latent heat transfer rate, no clear conclusion concerning the latent heat transfer predictive performance of the simulation model can be made. However, the sensible heat transfer rates were more relevant, due to the dry-bulb temperature adjustment discussed in Chapter 5. Hence, as seen from Figure 30, the simulation model was able to predict 66% of the experimental sensible heat transfer rates to within ±20%.

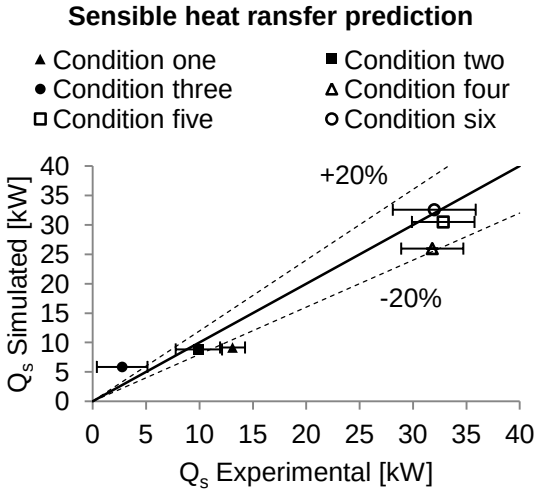

Figure 30: Experimental sensible heat transfer rate versus simulated sensible heat transfer rate.

6.1.7. Air outlet properties

In order to support the adjustments made in section 5.4, the airside outlet property predictions needed to be verified. In addition, the predictive ability of the present simulation must be evaluated. Since the experimental setup only measured the total air outlet properties, only these property values can be compared.

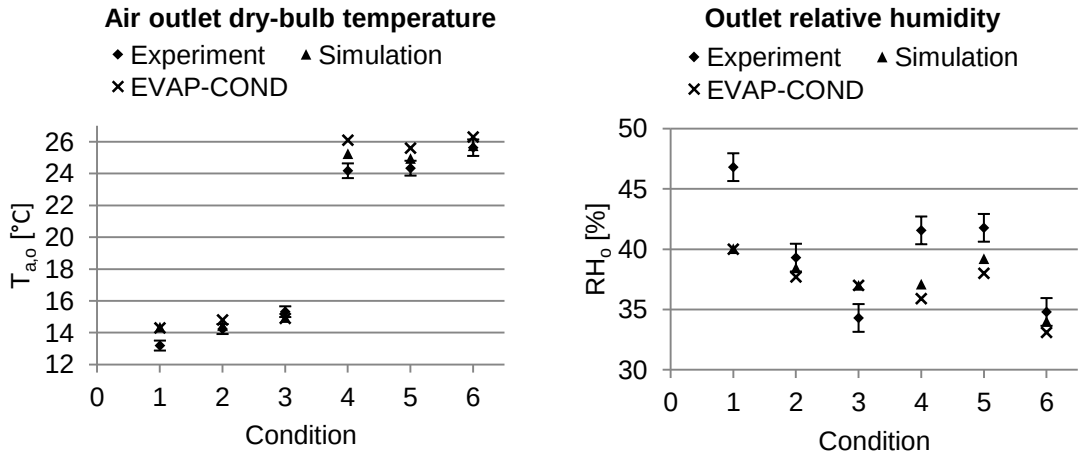

Figure 31: Experimental outlet air dry-bulb temperature and relative humidity, predicted by the present simulation and EVAP-COND.

— Comparison with EVAP-COND.

It can be seen from Figure 31 that the largest difference in values occurred in condition four where the simulated outlet dry-bulb temperature was slightly lower (3.3%) than that by EVAP-COND. Also, the simulated outlet relative humidity was slightly higher (3.4%) than that by EVAP-COND for this condition. As mentioned earlier, this condition had the highest latent heat transfer. Since a higher latent heat transfer rate entails a higher outlet relative humidity and a lower sensible heat transfer rate entails a lower outlet dry bulb temperature, the differences in values are expected. This serves as verification of the outlet air predictions of the present simulation.

— Comparison with experimental.

In conditions two and six, the simulated outlet dry-bulb temperature fell within the experimental uncertainty bands while in condition three the value was slightly under predicted by only 2.4% and in conditions one, four and five slightly over predicted (8.8%, 4.4% and 2.5% respectively).

From Figure 29 and Figure 31, it is illustrated that an over prediction in sensible heat transfer rate results in an under prediction in outlet dry-bulb temperature and vice versa. This is expected since the more heat is removed from the air, the more air cooling occurs resulting in a lower outlet dry-bulb temperature. However, good agreement between the simulated and experimental values were achieved, therefore the adjustments discussed in Chapter 5 are adequate.

Again, only in conditions two and six did the simulated air outlet relative humidity fall within the experimental uncertainty bands, while in condition three the outlet was over predicted by 7.9% and in conditions one, four and five, under predicted (14.4%, 10.7% and 6.1% respectively). As mentioned earlier, it was suspected that the outlet relative humidity sensor had been wetted by moisture. It is however clear from Figure 31 that the simulation also predicted the trend in the experimental values, between the six conditions.

From Figure 32, it is clear that the simulation was able to predict all of the air outlet properties to within ±20%.

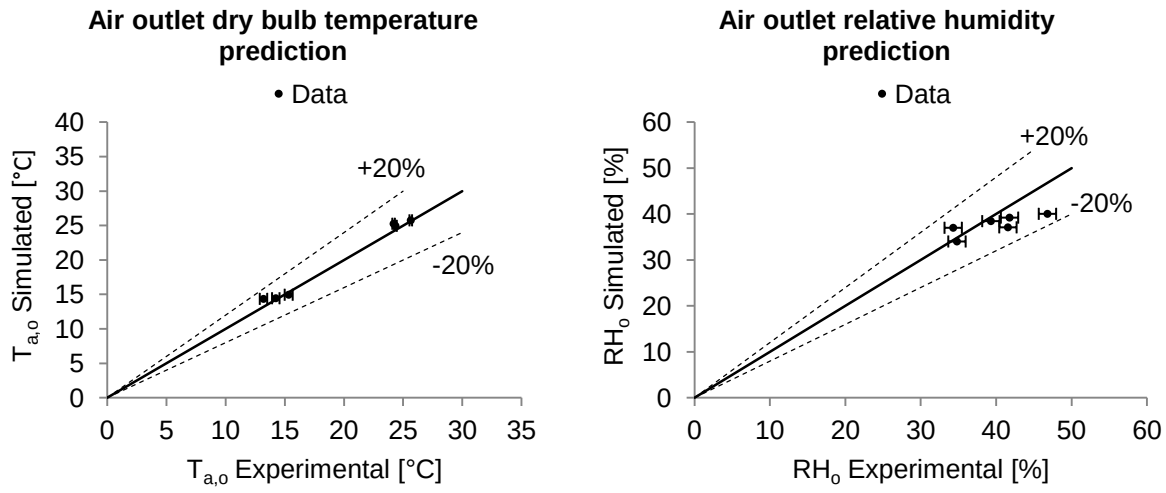

Figure 32: Experimental versus simulated outlet air dry-bulb temperature as well as experimental versus simulated outlet relative humidity.

6.1.8. Air pressure drop

The differential pressure sensor installed in the finned coil-testing tunnel can measure pressure drops in the range of 0 to 62Pa. However, in all the experimental conditions, the pressure drops through the coil were higher than 62Pa. Also, EVAP-COND does not simulate air pressure drop. Hence, the experimental pressure drop data and EVAP-COND could not be used to verify or validate the pressure drop prediction of the simulation model and will consequently be disregarded.

6.2. Predictions at higher inlet relative humidity values

Since no conclusion regarding the latent heat transfer rate predictive performance of the simulation could be reached, an investigation into the latent heat transfer rate modelling of the simulation compared to EVAP-COND was done. In only two of the previous experimental conditions (condition four and five) were dehumidification probable. In addition, the wind tunnel test facility cannot vary the inlet relative humidity (RH) in order to achieve larger experimental latent heat transfer rates.

Hence, five extra RH conditions were selected to cover a higher range. These conditions consisted of the same input values as condition five in the previous section, except only the inlet relative humidity was increased from 40% to 80% in 10% increments. It was expected that a higher inlet relative humidity would increase the latent heat transfer rate.

Figure 33 shows the overall and latent heat transfer rate predictions of the simulation model compared to EVAP-COND with an increase in inlet relative humidity.

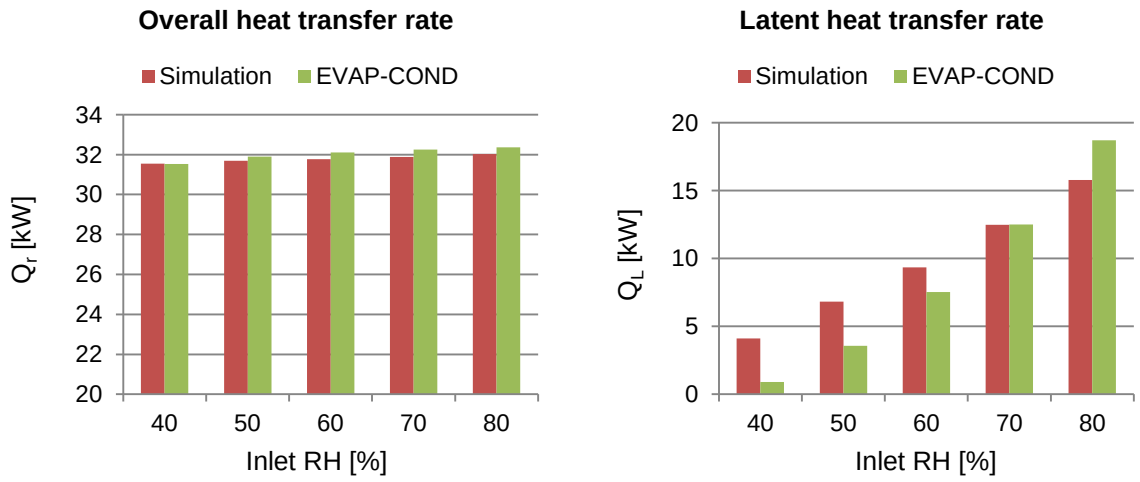

Figure 33: Overall (a) and latent (b) heat transfer rates for five RH conditions.

Figure 33a shows that at high inlet relative humidities (high latent heat transfer rate), the present simulation predicted slightly lower overall heat transfer rates with the largest difference of 1.1% in the 80% RH condition. It should again be noted that EVAP-COND uses a constant Lewis number while the present simulation adopts a correlation as stated in Chapter 3. Both simulations predicted an increase in overall heat transfer rate with an increase in relative humidity as reported by Chen & Wang (2008). Thus, the present simulation agrees with the reported trend of overall heat transfer rate at high inlet relative humidity values. Also, Figure 33b shows that the latent heat transfer rate increased with an increase in inlet relative humidity. Huzayyin *et al.* (2007) have also reported this, where the mass flow rate of water condensate increased with an increase in relative humidity.

Figure 34 shows the difference in dry-bulb temperature over the heat exchanger. From this figure, it can be concluded that both simulations agree with the reported negative trend of a declining temperature difference, with an increase in relative humidity, as reported by Huzayyin *et al.* (2007).

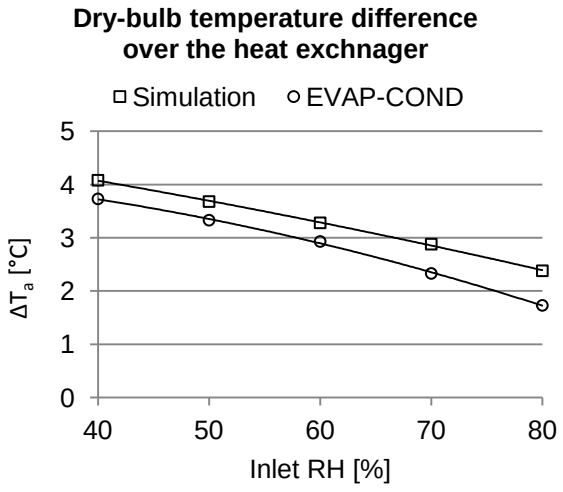

Figure 34: Dry-bulb temperature difference between the inlet and outlet of the heat exchanger.

6.3. Summary

This chapter discusses the successful verification and validation of the simulation model with respect to the commercial finned coil simulation package, EVAP-COND, and experimental data that has been generated as part of this study.

The present simulation model was able to predict 92.6% of the EVAP-COND data to within ±20%. The discrepancies were attributed to more recent correlations being used in the present simulation model that consists of updated versions of those used in EVAP-COND. Hence, the favourable aspects of CO_2 were more accurately correlated and in general higher. The differences in latent heat transfer rates seemed large but considering their relatively small magnitude, compared to for instance total heat transfer rates, predictions of such small values are very sensitive to very small inaccuracies. In addition, the difference in modelling mass transfer with a constant Lewis number (EVAP-COND) as opposed to the use of a correlation (present simulation) resulted in different mass transfer predictions. However, the present simulation model successfully identified dehumidifying conditions.

For the experimental comparison, even though the outlet air properties had been predicted well within the margin, the air latent heat transfer rate data was neglected. Thus, the model was able to predict 82% of the experimental data to within ±20%. The discrepancies were attributed to the presence of lubricant foam degrading the superheat region's heat transfer coefficient. A proposed degradation factor was evaluated with some success. In addition, the saturation point was accurately simulated to within the same tube as in the experiments.

In order to evaluate the present simulation at higher inlet relative humidity values, five extra RH conditions were simulated. It was found that the present simulation and EVAP-COND predicted the same trends as found in literature.

In the next chapter, conclusions are drawn to the aims of this study and the correlations used. Also, recommended future study topics are outlined.

CHAPTER 7:
Conclusion

In this chapter, conclusions are drawn with regard to the aims of this study and recommendations for future studies are outlined. The chapter layout will consist of:

- Conclusions of this study.
- Recommendations.

7.1. Conclusions of this study

- Literature survey

A comprehensive literature survey was done that not only discussed the various refrigerant and airflow phenomena, but also identified applicable correlations for both air and CO_2. The correlation by Wang *et al*, (2002) has shown very good predictive ability for the tested conditions. The correlations of Cheng *et al.* (2008a&b) have also shown good predictive ability. The effect of lubricant interfered with the heat transfer processes, as was predicted from the literature survey and discused in Chapter 6. Hence the lubricant does have a profound effect on the heat transfer within a CO_2 finned coil evaporator and will have to be included in a future simulation model. The selection of the simulation strategy to use fundamental discretised elements with fully wet or dry surface conditions was deemed successfull.

- Test facility upgrade

A CO_2 finned coil evaporator was designed to match the already existing heat pump facility and was procured from a finned coil manufacturing company. Also, adequate instrumentation were sourced and installed on the finned coil to measure CO_2 temperatures and pressures throughout the coil. A wind tunnel was utilised to measure and control the airside properties for experimental testing.

- Simulation model

A simulation model implementing the identified correlations was successfully developed for the specific geometry of the finned coil upgrade. The discretised model simulates both two-phase and superheat regions as well as wet and dry surface conditions.

- Model verification and validation

The developed simulation model is accurately verified with a similar software package, EVAP-COND (NIST, 2003), where 92.6% of the EVAP-COND data were predicted by the simulation to within ±20%. The discrepancies are attributed to the accuracy of the correlations used, especially the improved accuracy with the correlations used in this study. Also, the simulation model is accurately validated over the test conditions where 82% of the experimental data was predicted to within ±20%. However, since the simulation model does not include the effect of lubricant, discrepancies with the experimental data were found. A degradation factor that accounts for lubricant foam in the two-phase region was proposed and implemented in a modified simulation model with fair results.

7.2. Recommendations

The following recommendations are made with respect to future studies regarding CO_2 finned coil evaporators at the NWU:

- Airside instrumentation

The measurement of finned coil outlet air properties, especially under dehumidifying conditions, has always been difficult to accurately achieve. Considering the difficulty expressed in the present study especially with the determination of the latent heat transfer rates, better airside measurement techniques are required within the wind tunnel. A flow nozzle velocity measurement technique may be easier to accurately implement than the pitot technique. Also, a shroud for the already equipped temperature sensor may be installed to adequately eliminate any direct contact with the moist air stream inside the tunnel. The same shroud is recommended for the relative humidity sensor.

- Refrigerant side instrumentation

Since the CO_2 pressure drop is much lower than expected, the installed pressure sensors are of inadequate accuracy. Also, their factory calibration was done at a too high tolerance. Therefore, it is recommended that only one pressure sensor is used to establish the inlet pressure with respect to ambient and differential pressure sensors to measure the difference in pressure between the various points in the tube, such as high strength manometers or digital differential pressure gauges.

- Lubricant

Zhao & Bansal (2009), amoung others, has also reported that further research into CO_2-lubricant mixtures are necessary. Since lubricant has a great effect on the flow boiling phenomena of CO_2 and the complexities associated with lubricant foam, these effects must be further investigated and incorporated in future CO_2 finned coil evaporators.

Detailed experimental testing of the heat transfer characteristics of CO_2-lubricant mixtures should be conducted over a wide range of conditions and micro as well as macro tube diameters. Lubricants typically used in trans-critical applications should be considered. From this, new fluid property data or accurate corrections from that of pure CO_2 must be developed. Correlations incorporating this data as well as the weight percentage of lubricant can then be constructed. These correlations should follow a phenomenological approach to accurately describe the mixture during two-phase flow and the heat transfer processes.

- Generic model

Along with the addition of lubricant in the simulation model, the model may be extended to not only simulate a finned coil with the geometry of the finned coil upgrade, but also various other geometries for different applications. This would include aspects such as a junction tube connectivity matrix and a user interface.

- Validation range

Since only a few experimental conditions were used, extensive testing over a wide range of conditions is of interest. Different mass fluxes ($300 kg/m^2$ to $1300 kg/m^2$) as well as different geometry (P_t: 26 mm to 38mm, P_l: 13 mm to 33mm and F_s: 3 mm to 6mm) and relative humidity (40% to 90%) ranges may be tested. Also, lower evaporating temperatures of 0℃ to -30℃ and air mass flow rates of $1 kg/s$ to $8 kg/s$ are of interest.

Bibliography

AIDOUN, Z & OUZZANE, M. 2009. A model application to study circuiting and operation in CO2 refrigeration coils. *Applied Thermal Engineering*, 29(11-12):2544-2553.

AUSTIN, BT & SUMATHY, K. 2011. Transcritical carbon dioxide heat pump systems: A review. *Renewable and Sustainable Energy Reviews*, 15(8):4013-4029.

BELL, S. 2001. *A beginner's guide to uncertainty of measurement*. Teddington, Middlesex, United Kingdom.

BENDAOUD, A, OUZZANE, M, AIDOUN, Z & GALANIS, N. 2010. A new modeling approach for the study of finned coils with CO2. *International Journal of Thermal Sciences*, 49(9):1702-1711.

BITZER. 2011. *Operating instructions - Semi-hermetic reciprocating compressors for trans-critical CO2 applications, kb-130-2*.

BOURABAA, A, SAIGHI, M & BELAL, I. 2011. The Influence of the Inlet Conditions on the Air side Heat Transfer Performance of Plain Finned Evaporator. *World Academy of Science, Engineering and Technology*, 59:28-31.

CALM, JM. 2008. The next generation of refrigerants – Historical review, considerations, and outlook. *International Journal of Refrigeration*, 31:1123-1133.

CAWTE, H, SANDERS, D & POLAND, G. 1996. Effect of lubricating oil contamination on evaporation in refrigerants R12 and R22. *International Journal of Energy Research*, 20:663-679.

CHENG, L, RIBATSKI, G, QUIBEN, JM & THOME, JR. 2008a. New prediction methods for CO2 evaporation inside tubes: Part I - a two-phase flow pattern map and a flow pattern based phenomenological model for two-phase flow frictional pressure drops. *International Journal of Heat and Mass Transfer*, 51:111-124.

CHENG, L, RIBATSKI, G & THOME, JR. 2008b. New prediction methods for CO 2 evaporation inside tubes : Part II — An updated general flow boiling heat transfer model based on flow patterns. *International Journal of Heat and Mass Transfer*, 51:125-135.

CHENG, L, RIBATSKI, G, WOJTAN, L & THOME, JR. 2006. New flow boiling heat transfer model and flow pattern map for carbon dioxide evaporating inside horizontal tubes. *International Journal of Heat and Mass transfer*, 49:4082-4094.

CHEN, H & WANG, H. 2008. Estimation of heat-transfer charateristics on a fin under wet conditions. *International Journal of Heat and Mass Transfer*, 51(9-10):2123-2138.

CICCITTI, A, LOMBARDI, C, SILVESTRI, M, SOLDAINI, G & ZAVATTARELLI, R. 1960. Two-phase cooling experiments-pressure drop, heat transfer and burnout measurements. *Energia Nucleare*, 7(6):407-425.

DANG, C, HARAGUCHI, N, YAMADA, T, LI, M & HIHARA, E. 2012. Effect of lubricating oil on flow boiling heat transfer of carbon dioxide. *International Journal of Refrigeration*, 6(1):136-144.

DASSAULT SYSTEMES. 2010. *SolidWorks Office Premium*. http://www.solidworks.com/.

DAZHANG, Y, JING, L, ZHEBIN, H & XIUZHI, H. 2009. Simulation and Analysis of fin-tube Evaporator for Carbon dioxide heat pump. (*In* International Conference on Energy and Environment Technology. p. 0-3.)

DOMANSKI, PA. 1999. Finned-Tube evaporator model with a visual interface. (*In* International Congress of Refrigeration. Sydney. p. 1-7.)

ENEX-REF. 2013. http://www.enex-ref.com/Default.aspx Date of access: 24 Sep 2013.

FRIEDEL, L. 1979. Improved friction drop correlations for horizontal and vertical two-phase pipe flow. (*In* European Two-phase Flow Group Meeting. Ispra. p. Paper E2.)

GRAY, DL & WEBB, RL. 1986. Heat transfer and friction correlations for plate fin-and-tube heat exchangers having plain fins. (*In* 8th International Heat Transfer Conference. San Francisco. p. 2745-2750.)

GROENEVELD, DC. 1973. Post dry-out heat transfer at reactor operating conditions. (*In* ANS Topical Meeting on Water Reactor Safety. Salt Lake City.)

HARE, B. 1998. *Guide to the Kyoto protocol*. Greenpeace International.

HC HEAT EXCHANGERS. 2013. HC Heat Exchangers. http://www.hcaircon.com/

HUAI, X, KOYAMA, S, ZHAO, TS, SHINMURA, E, HIDEHIKO, K & MASAKI, M. 2004. An experimental study of flow boiling characteristics of carbon dioxide in multiport mini channels. *Applied Thermal Engineering*, 24:1443-1463.

HUZAYYIN, AS, NADA, SA & ELATTAR, HF. 2007. Air-side performance of a wavy-finned-tube direct expansion cooling and dehumidifying air coil. *International Journal of Refrigeration*, 30:230-244.

INCROPERA, DEWITT, BERGMAN & LAVINE. 2007. Fundamentals of Heat and Mass Transfer. John Wiley & Sons.

JIANG, H, AUTE, V & RADERMACHER, R. 2006. CoilDesigner: a general-purpose simulation and design tool for air-to-refrigerant heat exchangers. *International Journal of Refrigeration*, 29(4):601-610.

KATTAN, N, THOME, JR & FAVRAT, D. 1998. Flow boiling in horizontal tubes. Part 1: Development of a diabatic two- phase flow pattern map. *Journal of Heat and Mass Transfer*, 120(140-147)

KHUDHEYER, AF. 2011. Experimental study for heat and mass transfer from moist air flowing over moving water film. *ARPN Journal of Engineering and Applied Sciences*, 6(7):110-117.

KIM, M, PETTERSEN, J & BULLARD, CW. 2004. Fundamental process and system design issues in CO2 vapor compression systems. *Progress in Energy and Combustion Science*, 30:119-174.

KIM, NH, YOUN, B & WEBB, RL. 1999. Air-side heat transfer and friction correlations for plain fin-and-tube heat exchangers with staggered tube arrangements. *Journal of Heat Transfer*, 121:662-667.

KLEIN, S & ALVARADO, F. 2012. *Engineering Equation Solver*. Middleton, WI: F-Chart software.

KUVANNARAT, T, WANG, C & WONGWISES, S. 2006. Effect of fin thickness on the air-side performance of wavy fin-and-tube heat exchangers under dehumidifying conditions. *International Journal of Heat and Mass Transfer*, 49:2587-2596.

MA, X, DING, G, ZHANG, Y & WANG, K. 2009. Airside characteristics of heat, mass transfer and pressure drop for heat exchangers of tube-in hydrophilic coating wavy fin under dehumidifying conditions. *International Journal of Heat and Mass Transfer*, 52(19-20):4358-4370.

MASTRULLO, R, MAURO, AW, ROSATO, A & VANOLI, GP. 2010. Carbon dioxide heat transfer coefficients and pressure drops during flow boiling: Assessment of predictive methods. *International Journal of Refrigeration*, 33(6):1068-1085.

MIDGELY, Jr.T & HENNE, AL. 1930. Organic fluorides as refrigerants. *Industrial and Engineering Chemistry*, 22:542–545.

MINETTO, S. 2011. Theoretical and experimental analysis of a CO2 heat pump for domestic hot water. *International Journal of Refrigeration*, 34(3):742-751.

MIRTH, DR & RAMADHYANI, S. 1994. Correlations for predicting the air-side Nusselt numbers and friction factors in chilled-water cooling coils. *Experimental Heat Transfer*, 7:143-162.

MOLINA, MJ & ROWLAND, FS. 1974. Chlorine atom-catalysed destruction of ozone. *Nature*:810-812.

MUNSON, BR, YOUNG, DF, OKIISHI, TH & HUEBSCH, WW. 2010. Fundamentals of Fluid Mechanics. John Wiley & Sons.

NIST. 2003. *Simulation models for finned-tube heat exchangers - EVAP-COND.* Gaithersburg: National Institute of Standards and Technology.

OLIET, C, PEREZ-SEGARRA, CD, CASTRO, J & OLIVA, A. 2010. Modelling of fin-and-tube evaporators considering non-uniform in-tube heat transfer. *International Journal of Thermal Sciences*, 49:692-701.

OUZZANE, M & AIDOUN, Z. 2008. A Numerical Study of a Wavy Fin and Tube CO2 Evaporator Coil. *Heat Transfer Engineering*, 29(12):1008-1017.

PEARSON, A. 2005. Carbon dioxide - new uses for an old refrigerant. *International Journal of Refrigeration*, 28:1140–1148.

PETTERSEN, J, HAFNER, A, SKAUGEN, G & REKSTAD, H. 1998. Development of compact heat exchangers for CO2 air-conditioning systems. *International Journal of Refrigeration*, 21(3):180-193.

PIROMPUGD, W, WANG, C & WONGWISES, S. 2007. Finite circular fin method for heat and mass transfer charateristics for plain fin-and-tube heat exchangers under fully and partially wet surface conditions. *International Journal of Heat and Mass Transfer*, 30(3-4):552-565.

PIROMPUGD, W, WONGWISES, S & WANG, C. 2006. Simultaneous heat and mass transfer characteristics for wavy fin-and-tube heat exchangers under dehumidifying conditions. *International Journal of Heat and Mass Transfer*, 49:132-143.

ROBINSON, DM & GROLL, EA. 1998. Heat Transfer Analysis of Air-to-Carbon Dioxide Two-Phase heat absorption and supercritical heat rejection. *HVAC&R Research*, 4(4):327-345.

ROUSSEAU, PG. 2012. *Thermal-Fluid Systems Modelling 2 - Course Notes*. Potchefstroom: North-West University.

ROUSSEAU, PG, DU TOIT, CG, VAN ANTWERPEN, W & VAN ANTWERPEN, HJ. 2012. Seperate effects tests to determine the effective thermal conductivity in the PBMR HTTU test facility. (*In* HTR. Tokyo, Japan.)

SARKAR, J, BHATTACHARYYA, S & RAM GOPAL, M. 2006. Simulation of a transcritical CO2 heat pump cycle for simultaneous cooling and heating applications. *International Journal of Refrigeration*, 29(5):735-743.

SAWANT, NN, KIM, MS, PAYNE, VW, DOMANSKI, PA & HWANG, YW. 2003. A study of in-tube evaporation heat transfer of carbon dioxide. (*In* International Congress of Refrigeration. Washington D.C. p. 1-8.)

SCHMIDT, TE. 1949. Heat transfer calculations for extended surfaces. *Journal of the American Society of Refrigerating Engineers*, 57:351-357.

SHEN, B & GROLL, EA. 2005. Review Article: A Critical Review of the Influence of Lubricants on the Heat Transfer and Pressure Drop of Refrigerants, Part 1: Lubricant Influence on Pool and Flow Boiling. *HVAC&R Research*, 11(3):341-359.

SINGH, V, AUTE, V & RADERMACHER, R. 2008. Numerical approach for modeling air-to-refrigerant fin-and-tube heat exchanger with tube-to-tube heat transfer. *International Journal of Refrigeration*, 31(8):1414-1425.

TAO, Y B, HE, Y L, HUANG, J, WU, Z G & TAO, W Q. 2007. Numerical study of local heat transfer coefficient and fin efficiency of wavy fin-and-tube heat exchangers. *International Journal of Thermal Sciences*, 46:768-778.

THOME, JR & HAJAL, JE. 2004. Flow boiling heat transfer to carbon dioxide : general prediction method. *International Journal of Refrigeration*, 27:294-301.

UNITED NATIONS. 1987. *Montreal Protocol on Substances That Deplete the Ozone Layer*.

UNITED NATIONS. 1998. *Kyoto Protocol to the United Nations Framework Convention on Climate Change*.

UNITED NATIONS. 2009. Framework Convention on Climate Change, Conference Of the Parties 15'th Session. (Copenhagen.)

VENTER, P. 2010. *A supercritical R-744 heat transfer simulation implementing various Nusselt number correlations*. Potchefstroom.

WALTRICH, M, HERMES, CJL, GONCALVES, JM & MELO, C. 2010. A first-principles simulation model for the thermo-hydraulic performance of fan supplied tube-fin heat exchangers. *Applied Thermal Engineering*, 30(14-15):2011-2018.

WANG, CC & CHI, KY. 2000. Heat transfer and friction characteristics of plain fin-and-tube heat exchangers, part I: new experimental data. *International Journal of Heat and Mass Transfer*, 43(15):2681-2691.

WANG, C, CHI, K & CHANG, C. 2000a. Heat transfer and friction characteristics of plain fin-and-tube heat exchangers, part II: Correlation. *International Journal of Heat and Mass Transfer*, 43(15):2693-2700.

WANG, CC, FU, WL & CHANG, CT. 1997. Heat transfer and friction characteristics of typical wavy fin-and-tube heat exchangers. *Experimental Thermal and Fluid Science*, 14(2):174-186.

WANG, CC, HAFNER, A, KUO, C & HSIEH, W. 2012. An overview of the effect of lubricant on the heat transfer performance on conventional refrigerants and natural refrigerant R-744. *Renewable and Sustainable Energy Reviews*, 16(7):5071-5086.

WANG, C, HWANG, Y & LIN, Y. 2002. Empirical correlations for heat transfer and flow friction characteristics of herringbone wavy fin-and-tube heat exchangers. *International Journal of Refrigeration*, 25:673-680.

WANG, C & LIAW, J. 2012. Air-side performance of herringbone wavy fin-and-tube heat exchangers under dehumidifying condition – Data with larger diameter tube. *International Journal of Heat and Mass Transfer*, 55(11-12):3054-3060.

WANG, CC, LIN, YT & LEE, CJ. 2000c. An airside correlation for plain fin-and-tube heat exchangers in wet conditions. *International Journal of Heat and Mass Transfer*, 43(10):1869-1872.

WANG, S, TUO, H, CAO, F & XING, Z. 2012. Experimental investigation on air-source transcritical CO2 heat pump water heater system at a fixed water inlet temperature. *International Journal of Refrigeration*:1-16.

WANG, CC, WEBB, RL & CHI, KY. 2000b. Data reduction for air-side performance of fin-and-tube heat exchangers. *Experimental Thermal and Fluid Sciences*, 21(4):218-226.

WOJTAN, L, URSENBACKER, T & THOME, JR. 2005. Investigation of flow boiling in horizontal tubes: Part II – Development of a new heat transfer model for stratified-wavy, dryout and mist flow regimes. *International Journal of Heat and Mass Transfer*, 48:2970–2985.

WONGWISES, S & CHOKEMAN, Y. 2005. Effect of fin pitch and number of tube rows on the air side performance of herringbone wavy fin and tube heat exchangers. *Energy Conversion and Management*, 46:2216-2231.

YUN, R & KIM, Y. 2009. Post-dryout heat transfer characteristics in horizontal mini-tubes and a prediction method for flow boiling of CO2. *International Journal of Refrigeration*, 32(5):1085-1091.

YUN, R, KIM, Y, KIM, MS & CHOI, Y. 2003. Boiling heat transfer and dryout phenomenon of CO2 in a horizontal smooth tube. *International Journal of Heat and Mass Transfer*, 46:2353-2361.

ZHAO, X & BANSAL, P. 2009. Critical review of flow boiling heat transfer of CO2 – lubricant mixtures. *International Journal of Heat and Mass Transfer*, 52(3-4):870-879.

ZHAO, Y, MOLKI, M, OHADI, M, FRANCA, FHR & RADERMACHER, R. 2002. Flow boiling of CO2 with miscible oil in microchannels. *ASHRAE Trans.*, 108:135–144.

ZILIO, C, CECCHINATO, L, CORRADI, M & SCHIOCHET, G. 2007. An assessment of heat transfer through fins in a fin-and-tube gas cooler for transcritical carbon dioxide cycles. *HVAC&R Research*, 3(13):457-469.

Appendix A
Compressor Chart

Verdichtertyp Compressor type Type de compresseur	Gaskühleraustritts-Temperatur Gas cooler outlet temperature Température à sortie de refroidisseur de gaz [°C]	Hochdruck High pressure Haute pression [bar]		Kälteleistung Cooling capacity Puissance frigorifique Q_o [Watt] — Verdampfungstemperatur °C / Evaporating temperature °C / Température d'évaporation °C							
				10 ①	5 ①	0	-5	-10	-15	-20
4MTC-7K	15	75	Q_o			27650	23100	19090	15440	12310
			P_e			6,41	6,47	6,43	6,28	6,01
	25	75	Q_o			23550	19690	16220	13160	10490
			P_e			6,41	6,47	6,43	6,28	6,01
	30	75	Q_o			20150	16880	13920	11290	9000
			P_e			6,41	6,47	6,43	6,28	6,01
	35	90	Q_o			18000	14970	12240	9830	7740
			P_e			7,77	7,61	7,37	7,05	6,61
	40	100	Q_o			15650	12960	10530	8390	
			P_e			8,55	8,26	7,91	7,47	
4KTC-10K	15	75	Q_o			41400	34700	28700	23450	18960
			P_e			9,32	9,49	9,46	9,24	8,85
	25	75	Q_o			35200	29550	24450	19980	16160
			P_e			9,32	9,49	9,46	9,24	8,85
	30	75	Q_o			30200	25350	21000	17150	13860
			P_e			9,32	9,49	9,46	9,24	8,85
	35	90	Q_o			26850	22450	18510	15090	12010
			P_e			11,42	11,29	10,97	10,48	9,83
	40	100	Q_o			23200	19380	15940	12870	
			P_e			12,66	12,33	11,84	11,18	
4JTC-10K 4JTC-15K ①	15	75	Q_o	59500	49900	40700	33550	27550	22450	17920
			P_e	8,61	8,94	9,17	9,29	9,27	9,09	8,73
	25	75	Q_o	50500	41900	34650	28600	23450	19110	15270
			P_e	8,61	8,94	9,17	9,29	9,27	9,09	8,73
	30	75	Q_o	43100	35850	29700	24500	20150	16400	13100
			P_e	8,61	8,94	9,17	9,29	9,27	9,09	8,73
	35	90	Q_o	38900	32250	26650	21950	17960	14570	11570
			P_e	11,07	11,10	11,05	10,89	10,61	10,19	9,60
	40	100	Q_o	33900	28150	23250	19110	15630	12660	
			P_e	12,49	12,34	12,12	11,81	11,38	10,82	
4HTC-15K 4HTC-20K ①	15	75	Q_o	72000	61500	51900	43200	35600	28900	23150
			P_e	11,00	11,42	11,70	11,83	11,78	11,53	11,05
	25	75	Q_o	61100	52200	44200	36850	30300	24650	19750
			P_e	11,00	11,42	11,70	11,83	11,78	11,53	11,05
	30	75	Q_o	52200	44700	37850	31600	26000	21150	16950
			P_e	11,00	11,42	11,70	11,83	11,78	11,53	11,05
	35	90	Q_o	46900	40200	33950	28250	23200	18790	14870
			P_e	14,17	14,20	14,11	13,88	13,49	12,92	12,14
	40	100	Q_o	40800	35000	29600	24600	20150	16200	
			P_e	16,03	15,82	15,50	15,06	14,46	13,70	
4FTC-20K	15	75	Q_o			79400	66200	55100	45400	36850
			P_e			18,02	18,15	17,99	17,55	16,85
	25	75	Q_o			67500	56400	46900	38700	31400
			P_e			18,02	18,15	17,99	17,55	16,85
	30	75	Q_o			57900	48400	40300	33200	26950
			P_e			18,02	18,15	17,99	17,55	16,85
	35	90	Q_o			52000	43300	35950	29550	23850
			P_e			21,80	21,50	20,90	20,00	18,87
	40	100	Q_o			46300	37650	31150	25550	
			P_e			24,10	23,50	22,60	21,40	

Figure 35: Compressor chart from the manufacturer (Bitzer, 2011).

Appendix B
Finned coil specification

---------- EVAPORATOR CALCULATOR REPORT ----------

04/07/2012

PDX-4A-24x1200x2Rx12F-12C

3 DXC - 24.0 x 1200 x 2R x 12.00F x 12.00C - Cu/Al

COIL DESIGN

Tubing	10.1 x 0.41 mm
Height	24 in.
Length	1200 mm.
Tube rows	2
Fin spacing	12 fpi
Circuits	12

BAROMETER

Atmospheric pressure	85.00 kPa
Altitude	1457.37 m

AIR

Entering temperature	25.00/13.68 C
Leaving temperature	9.17/6.45 C
RH ON	30.00 %
RH OFF	70.31 %
Enthalpy ON	42.98 kJ/kg
Enthalpy OFF	24.36 kJ/kg
Inlet dew point	6.25 C
Inlet HR	7.01 gw/kga
Dehumidification rate	6.25 kg/hr
Mass flow	1.780 kg/s
Volume flow	1.800 m3/s
Face velocity	2.461 m/s
Pressure drop	47.98 Pa

REFRIGERANT (CO2)

Evaporating temperature	-4.00 C
Superheat	0.00 K
Mass flow	0.171 kg/s
Charge	0.89 kg
Pressure drop	5.77 kPa

DUTY

Total duty	33.149 kW
Sensible duty	28.680 kW
SHR	0.865
Coil condition	DRY/WET

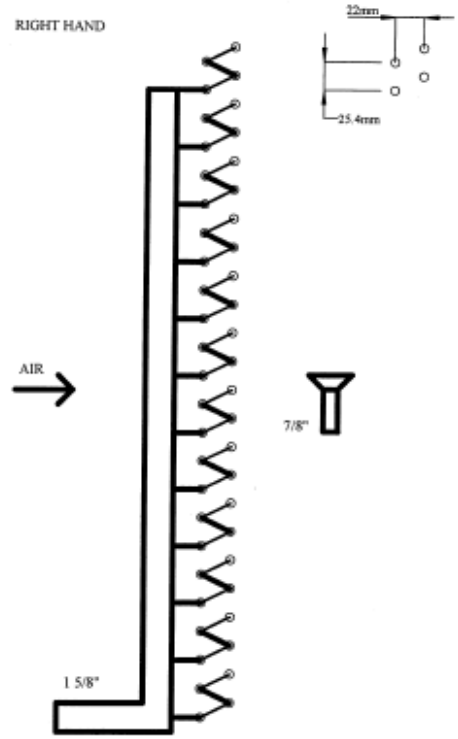

MODEL	
▬ ▬ X X R X F X C	
CONNECTIONS	WORKS ORDER

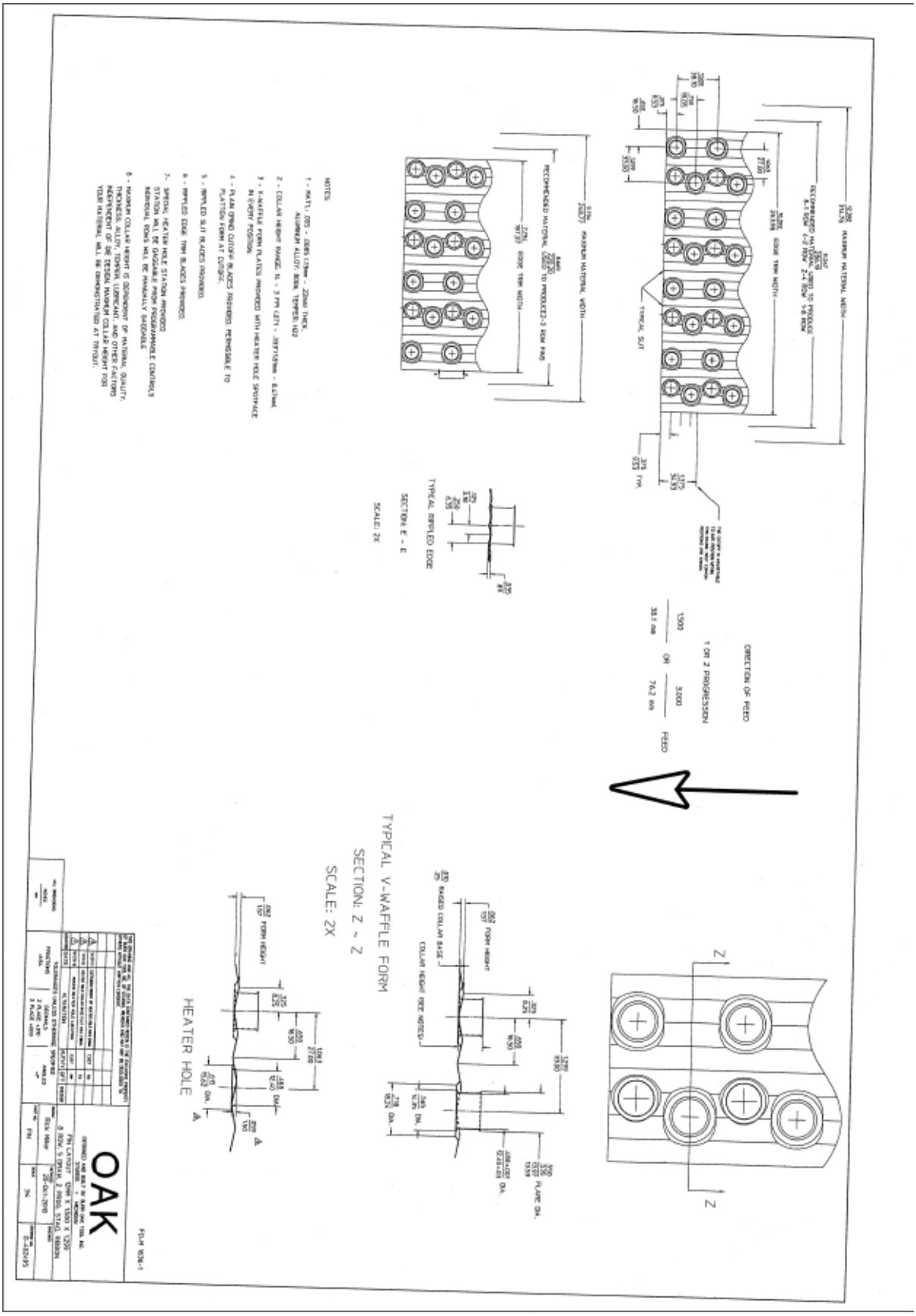

Figure 36: Finned coil specification and fin sheet from which fin properties were derived (HC Heat Exchangers, 2013).

Appendix C
Hand uncertainty propagation

Uncertainty propagation calculated by hand for the heat transfer rate in the evaporator at the experimental condition one using the measured CO_2 properties:

$T_{gc,o}$: 33.4 ± 0.2368 ℃ (GasC T13 39)

$P_{gc,o}$: 7440000 ± 73000 Pa (ExpV Pi 55)

$T_{e,o}$: 12.7 ± 0.028 ℃ (Evap T5 5)

$P_{e,o}$: 3410000 ± 46000 Pa (Evap P5 5)

$\dot{m}_r$: 0.1435 ± 0.0001076 kg/s (CO2 MasFlo 59)

Equations used to calculate the experimental heat transfer rate:

$$Q = \dot{m}_r \Delta i \tag{C-1}$$

And

$$\Delta i = (i_e - i_i) \tag{C-2}$$

Applying equation 5.6 to C-2, the uncertainty in the calculation of Δi, denoted as $u(\Delta i)$ is as follows:

$$u(\Delta i) = \sqrt{\left[\frac{\partial \Delta i}{\partial i_e} u(i_e)\right]^2 + \left[\frac{\partial \Delta i}{\partial i_i} u(i_i)\right]^2} \tag{C-3}$$

Where i_e and $u(i_e)$ as well as i_i and $u(i_i)$ is calculated from the respective temperature and pressure values using EES, since the hand propagation for the built-in property function is very complex.

Hence: $i_e = -54127 \pm 804.7\, j/kg.K$ $i_i = -116681 \pm 5232\, j/kg.K$

Thus:

$$\begin{aligned} u(\Delta i) &= \sqrt{\big(1(804.7)\big)^2 + \big(-1(5232)\big)^2} = \sqrt{647542.09 + 27373824} = \sqrt{28021366.09} \\ &= 5293.521143\, j/kg.K \end{aligned} \tag{C-4}$$

Then, by now applying equation 5.6 to C-1, the uncertainty in the calculation of Q, denoted as $u(Q)$, is calculated as follows:

$$\begin{aligned} u(Q) &= \sqrt{\left[\frac{\partial Q}{\partial \dot{m}_r} u(\dot{m}_r)\right]^2 + \left[\frac{\partial Q}{\partial \Delta i} u(\Delta i)\right]^2} \\ &= \sqrt{\Big(\big(-54127 - (-116681)\big)0.0001076\Big)^2 + \big(0.1435(5293.521143)\big)^2} \\ &= \sqrt{45.303808 + 577022.9759} = \sqrt{577068.2797} = 759.650103W \end{aligned} \tag{C-5}$$

Where EES calculates: $u(Q) = 759.655487W$

This gives a negligible difference of $0.005384W$.

Appendix D
EES code

```
"----------------------------------------------------------------------------Procedures----------------------------------------------------------------------------"
"Outlet refrigerant properties"
Procedure Specificheat_out (x_o,Pr_o,hr_o:Cpr_o)
if (x_o<=0) then
      Cpr_o=Cp(R744,P=Pr_o,h=hr_o)
endif

if (x_o>0) and (x_o<1) then
      Cp_f=Cp(R744,P=Pr_o,x=0)
      Cp_g=Cp(R744,P=Pr_o,x=1)
      Cpr_o=Cp_g*x_o+Cp_f*(1-x_o)
endif

if (x_o>=1) then
      Cpr_o=Cp(R744,P=Pr_o,h=hr_o)
endif
END

Procedure Densityrho_out (x_o,Pr_o,hr_o:rho_r_o)
if (x_o<=0) then
      rho_r_o=Density(R744,P=Pr_o,h=hr_o)
endif

if (x_o>0) and (x_o<1) then
      rho_f=Density(R744,P=Pr_o,x=0)
      rho_g=Density(R744,P=Pr_o,x=1)
      rho_r_o=rho_g*x_o+rho_f*(1-x_o)
endif

if (x_o>=1) then
      rho_r_o=Density(R744,P=Pr_o,h=hr_o)
endif
END

Procedure Viscosity_out (x_o,Pr_o,hr_o:mu_r_o)
if (x_o<=0) then
      mu_r_o=Viscosity(R744,P=Pr_o,h=hr_o)
endif

if (x_o>0) and (x_o<1) then
      mu_f=Viscosity(R744,P=Pr_o,x=0)
      mu_g=Viscosity(R744,P=Pr_o,x=1)
      mu_r_o=mu_g*x_o+mu_f*(1-x_o)
endif

if (x_o>=1) then
      mu_r_o=Viscosity(R744,P=Pr_o,h=hr_o)
endif
END

Procedure Conductivity_out (x_o,Pr_o,hr_o:k_r_o)
if (x_o<=0) then
      k_r_o=Conductivity(R744,P=Pr_o,h=hr_o)
endif

if (x_o>0) and (x_o<1) then
      k_f=Conductivity(R744,P=Pr_o,x=0)
      k_g=Conductivity(R744,P=Pr_o,x=1)
      k_r_o=k_g*x_o+k_f*(1-x_o)
endif

if (x_o>=1) then
      k_r_o=Conductivity(R744,P=Pr_o,h=hr_o)
endif
END

"Refrigerant two-phase heat transfer coefficient and pressure drop"
Procedure RefrigerantFlowMap (G,Tr_i,hr_i,x_i,D_i,Aff_ref,A_inc_ref,L_inc,gra,m_dot_r,Pr_i,Q_flux:h_tp,h$,DELTAP_r)
      D_eq=D_i

If x_i<0.999 then
      theta_dry=0
      Pcrit=P_crit(R744)
      pr=Pr_i/Pcrit
      M=MolarMass(R744)

"Fluid properties"
      rho_l=Density(R744,T=Tr_i,x=0)
      rho_v=Density(R744,T=Tr_i,x=1)
      mu_l=Viscosity(R744,T=Tr_i,x=0)
      mu_v=Viscosity(R744,T=Tr_i,x=1)
```

```
k_v=Conductivity(R744,T=Tr_i,x=1)
k_l=Conductivity(R744,T=Tr_i,x=0)
Cp_v=SpecHeat(R744,T=Tr_i,x=1)
Cp_l=SpecHeat(R744,T=Tr_i,x=0)
sigma=SurfaceTension(R744,T=Tr_i)
h_vap=Enthalpy(R744,T=Tr_i,x=1)
h_liq=Enthalpy(R744,T=Tr_i,x=0)
h_LV=h_vap-h_liq

We_l=(G^2*D_eq)/(rho_l*sigma)
We_v=(G^2*D_eq)/(rho_v*sigma)
Fr_v_mori=G^2/(rho_v*(rho_l-rho_v)*gra*D_eq)
qcrit=0.131*rho_v^0.5*h_LV*(gra*sigma*(rho_l-rho_v))^0.25

x_IA=1/(1.8^(1/0.875)*(rho_v/rho_l)^(-1/1.75)*(mu_l/mu_v)^(-1/7)+1)
x_di=0.58*exp(0.52-0.236*We_v^0.17*Fr_v_mori^0.17*(rho_v/rho_l)^0.25*(Q_flux/qcrit)^0.27)
x_de=0.61*exp(0.57-0.502*We_v^0.16*Fr_v_Mori^0.15*(Q_flux/qcrit)^0.72*(rho_v/rho_l)^(-0.09))

epsilon_x_IA=x_IA/(rho_v*((1+0.12*(1-x_IA))*(x_IA/rho_v+(1-x_IA)/rho_l)+(1.18*(1-x_IA)*((gra*sigma*(rho_l-rho_v))^(1/4)))/(G*rho_l^0.5)))
epsilon=x_i/(rho_v*((1+0.12*(1-x_i))*(x_i/rho_v+(1-x_i)/rho_l)+(1.18*(1-x_i)*((gra*sigma*(rho_l-rho_v))^(1/4)))/(G*rho_l^0.5)))

A_l=Aff_ref*(1-epsilon)
A_l_x_IA=Aff_ref*(1-epsilon_x_IA)

"!Flow regimes"

"Intermittent flow"
if x_i<x_IA then
    deltadelta=D_eq/2-sqrt((D_eq/2)^2-(2*A_l)/(2*3.1415-theta_dry))
    delta=if(deltadelta,(D_eq/2),deltadelta,deltadelta,(D_eq/2))
    delta_IA=D_eq/2-sqrt(((D_eq/2)^2-(2*A_l_x_IA)/(2*3.1415-theta_dry)))

    Re_delta=(4*G*(1-x_i)*delta)/(mu_l*(1-epsilon))
    Re_v=(G*x_i*D_eq)/(mu_v*epsilon)
    Prandl_l=(Cp_l*mu_l)/k_l
    Prandl_v=(Cp_v*mu_v)/k_v
    S=1

    h_cb=0.0133*Re_delta^0.69*Prandl_l^0.4*(k_l/delta)
    h_nb=131*Q_flux^0.58*pr^(-0.0063)*(-log10(pr))^(-0.55)*M^(-0.5)
    h_wet=((S*h_nb)^3+h_cb^3)^(1/3)
    h_v=0.023*Re_v^0.8*Prandl_v^0.4*(k_v/D_eq)
    h_tp=(theta_dry*h_v+(2*3.1415-theta_dry)*h_wet)/(2*3.1415)
    h$='Intermittent'

    u_v=(G*x_i)/(rho_v*epsilon)
    f_A=3.128*Re_v^(-0.454)*We_l^(-0.0308)
    DELTAP_A=4*f_A*(L_inc/D_eq)*((rho_v*u_v^2)/2)

    Re_LO=(G*D_eq)/mu_l
    f_LO=0.079/Re_LO^0.25
    DELTAP_LO=4*f_LO*(L_inc/D_eq)*(G^2/(2*rho_l))
    DELTAP_r=DELTAP_LO*(1-epsilon/epsilon_x_IA)*DELTAP_A*(epsilon/epsilon_x_IA)
else

"Annular flow"
if (x_i>x_IA) AND (x_i<x_di) then
    deltadelta=D_eq/2-sqrt((D_eq/2)^2-(2*A_l)/(2*3.1415-theta_dry))
    delta=if(deltadelta,(D_eq/2),deltadelta,deltadelta,(D_eq/2))
    delta_IA=D_eq/2-sqrt(((D_eq/2)^2-(2*A_l_x_IA)/(2*3.1415-theta_dry)))

    Re_delta=(4*G*(1-x_i)*delta)/(mu_l*(1-epsilon))
    Re_v=(G*x_i*D_eq)/(mu_v*epsilon)
    Prandl_l=(Cp_l*mu_l)/k_l
    Prandl_v=(Cp_v*mu_v)/k_v
    S=1-1.14*(1-delta/delta_IA)^2.2

    h_cb=0.0133*Re_delta^0.69*Prandl_l^0.4*(k_l/delta)
    h_nb=131*(Q_flux)^0.58*pr^(-0.0063)*(-log10(pr))^(-0.55)*M^(-0.5)
    h_wet=((S*h_nb)^3+h_cb^3)^(1/3)
    h_v=0.023*Re_v^0.8*Prandl_v^0.4*(k_v/D_eq)
    h_tp=(theta_dry*h_v+(2*3.1415-theta_dry)*h_wet)/(2*3.1415)
    h$='Annular'

    u_v=(G*x_i)/(rho_v*epsilon)
    f_A=3.128*Re_v^(-0.454)*We_l^(-0.0308)
    DELTAP_r=4*f_A*(L_inc/D_eq)*((rho_v*u_v^2)/2)
else

"Dryout"
if (x_i>x_di) AND (x_i<x_de) then
    A_l_x_di=Aff_ref*(1-x_di)
    epsilon_x_di=x_di/(rho_v*((1+0.12*(1-x_di))*(x_di/rho_v+(1-x_di)/rho_l)+(1.18*(1-x_di)*((gra*sigma*(rho_l-
    ...rho_v))^(1/4)))/(G*rho_l^0.5)))

    deltadelta=D_eq/2-sqrt((D_eq/2)^2-(2*A_l)/(2*3.1415-theta_dry))
```

```
            delta=if(deltadelta,(D_eq/2),deltadelta,deltadelta,(D_eq/2))
            deltadelta_x_di=D_eq/2-sqrt((D_eq/2)^2-(2*A_l_x_di)/(2*3.1415-theta_dry))
            delta_x_di=if(deltadelta_x_di,(D_eq/2),deltadelta_x_di,deltadelta_x_di,(D_eq/2))
            delta_IA=D_eq/2-sqrt(((D_eq/2)^2-(2*A_l_x_IA)/(2*3.1415-theta_dry)))
            Re_delta_x_di=(4*G*(1-x_di)*delta)/(mu_l*(1-epsilon_x_di))
            Re_v_x_di=(G*x_di*D_eq)/(mu_v*epsilon_x_di)
            Re_H_x_de=((G*D_eq)/mu_v)*(x_de+(rho_v/rho_l)*(1-x_de))
            Prandl_l=(Cp_l*mu_l)/k_l
            Prandl_v=(Cp_v*mu_v)/k_v

            Y_x_de=1-0.1*((rho_l/rho_v-1)*(1-x_de))^0.4
            SS_x_di=1-1.14*(1-delta_x_di/delta_IA)^2.2
            S_x_di=if(x_di,x_IA,1,SS_x_di,SS_x_di)

            h_cb_x_di=0.0133*Re_delta_x_di^0.69*Prandl_l^0.4*(k_l/delta)
            h_v_x_di=0.023*Re_v_x_di^0.8*Prandl_v^0.4*(k_v/D_eq)
            h_nb=131*Q_flux^0.58*pr^(-0.0063)*(-log10(pr))^(-0.55)*M^(-0.5)
            h_wet_x_di=((S_x_di*h_nb)^3+h_cb_x_di^3)^(1/3)
            h_m_x_de=(0.00000002*Re_H_x_de^1.97*Prandl_v^1.06*Y_x_de^(-1.83)*(k_v/D_eq))
            h_tp_x_di=(theta_dry*h_v_x_di+(2*3.1415-theta_dry)*h_wet_x_di)/(2*3.1415)
            h_tp=h_tp_x_di-((x_i-x_di)/(x_de-x_di))*(h_tp_x_di-h_m_x_de)
            h$='Dryout'

            u_v_x_di=(G*x_di)/(rho_v*epsilon_x_di)
            f_A_x_di=3.128*Re_v_x_di^(-0.454)*We_l^(-0.0308)
            DELTAP_tp_x_di=4*f_A_x_di*(L_inc/D_eq)*((rho_v*u_v_x_di^2)/2)
            epsilon_H_x_de=(1+((1-x_de)/x_de)*(rho_v/rho_l))^(-1)
            rho_H_x_de=rho_l*(1-epsilon_H_x_de)+rho_v*epsilon_H_x_de
            mu_H_x_de=mu_l*(1-x_de)+mu_v*x_de
            Re_m_x_de=(G*D_eq)/mu_H_x_de
            f_m_x_de=91.2/(Re_m_x_de^0.832)
            DELTAP_m_x_de=4*f_m_x_de*(L_inc/D_eq)*(G^2/(2*rho_H_x_de))
            DELTAP_r=DELTAP_tp_x_di-((x_i-x_di)/(x_de-x_di))*(DELTAP_tp_x_di-DELTAP_m_x_de)
        else

        "Mist"
        if (x_i>x_de) then
            Re_H=((G*D_eq)/mu_v)*(x_i+(rho_v/rho_l)*(1-x_i))
            Prandl_v=(Cp_v*mu_v)/k_v
            Y=1-0.1*((rho_l/rho_v-1)*(1-x_i))^0.4
            h_tp=(0.00000002*Re_H^1.97*Prandl_v^1.06*Y^(-1.83)*(k_v/D_eq))
            h$='Mist'

            mu_H=mu_l*(1-x_i)+mu_v*x_i
            Re_m=(G*D_eq)/mu_H
            f_m=91.2/(Re_m^0.832)
            epsilon_H=(1+((1-x_i)/x_i)*(rho_v/rho_l))^(-1)
            rho_H=rho_l*(1-epsilon_H)+rho_v*epsilon_H
            DELTAP_r=4*f_m*(L_inc/D_eq)*(G^2/(2*rho_H))
        endif
        endif
        endif
        endif

else
        h_tp=1
        h$='Superheat'

        mu_SH=Viscosity(R744,h=hr_i,P=Pr_i)
        rho_SH=Density(R744,h=hr_i,P=Pr_i)
        Re_SH=ABS((m_dot_r*D_i)/(mu_SH*Aff_ref))
        V_r=m_dot_r/(rho_SH*Aff_ref)
        f_SH=(1.82*log10(Re_SH)-1.64)^(-2)
        DELTAP_r=f_SH* (L_inc/D_eq)* (V_r^2/(2*gra))*(rho_SH*gra)
endif
END

Procedure AirHeatTransferCoefficient (Re_Dc,Dc,Dh_air,Fs,Pt,theta,Ntr,Pl:j_dry,f_a)
If Re_Dc<1000 then
        J1=0.0045-0.491*Re_Dc^(-0.0316-0.0171*ln(Ntr*tan(theta)))*(Pl/Pt)^(-
        ...0.109*ln(Ntr*tan(theta)))*(Dc/Dh_air)^(0.542+0.0471*Ntr)*(Fs/Dc)^0.984*(Fs/Pt)^(-0.349)
        J2=-2.72+6.84*tan(theta)
        J3=2.66*tan(theta)

        j_dry=0.882*Re_Dc^J1*(Dc/Dh_air)^J2*(Fs/Pt)^J3*(Fs/Dc)^(-1.58)*tan(theta)^(-0.2)

        F1=-0.574-0.137*(ln(Re_Dc)-5.26)^0.245*(Pt/Dc)^(-0.765)*(Dc/Dh_air)^(-0.243)*(Fs/Dh_air)^(-0.474)*tan(theta)^(-0.217)*Ntr^0.035
        F2=-3.05*tan(theta)
        F3=-0.192*Ntr
        F4=-0.646*tan(theta)

        f_a=4.37*Re_dc^F1*(Fs/Dh_air)^F2*(Pl/Pt)^F3*(Dc/Dh_air)^0.2054*Ntr^F4
else
        J1=-0.0545-0.0538*tan(theta)-0.302*Ntr^(-0.24)*(Fs/Pl)^(-1.3)*(Pl/Pt)^0.379*(Pl/Dh_air)^(-1.35)*tan(theta)^(-0.256)
        J2=-1.29*(Pl/Pt)^(1.77-9.43*tan(theta))*(Dc/Dh_air)^(0.229-1.43*tan(theta))*Ntr^(-0.166-1.08*tan(theta))*(Fs/Pt)^(-0.174*ln(0.5*Ntr))
        J3=1
```

```
    j_dry=0.0646*Re_Dc^J1*(Dc/Dh_air)^J2*(Fs/Pt)^(-1.03)*(Pl/Dc)^0.432*tan(theta)^(-0.692)*Ntr^(-0.737)

    F1=-0.141*(Fs/Pl)^0.0512*tan(theta)^(-0.472)*(Pl/Pt)^0.35*(Pt/Dh_air)^(0.449*tan(theta))*Ntr^(-0.049+0.237*tan(theta))
    F2=-0.562*(ln(Re_Dc))^(-0.0923)*Ntr^0.013
    F3=0.302*Re_Dc^0.03*(Pt/Dc)^0.026
    F4=-0.306+3.63*tan(theta)

    f_a=0.228*Re_Dc^F1*tan(theta)^F2*(Fs/Pl)^F3*(Pl/Dc)^F4*(Dc/Dh_air)^0.383*(Pl/Pt)^(-0.247)
endif
END

"-----------------------------------------------------------------------------------------------------------------------------------------------------------------------"
"Constants"
gra=9.81
k_fin=k_ ('Aluminum', 298)
k_t=k_ ('Copper', 298)

"Tube geometry"
D_o=0.0101
Dc=D_o+2*Fin_th
r_o=Dc/2
D_i=D_o-0.00041*2
r_i=D_i/2

"Increment geometry"
W_inc=0.022
H_inc=0.0254
L_inc=4.8/n
N_f_inc=L_inc/Fs
A_f_inc=0.069973
A_t_inc=0.004805
A_inc_air=0.074436
A_inc_ref=2*Pl*r_i*L_inc
Aff_ref=Pl*r_i^2
Aff_air=0.002028
Vol_inc=H_inc*L_inc*W_inc

"Evaporator geometry"
W_e=0.044
Fin_th=0.00014
Fin_H=0.026069
Fs=0.00211666-Fin_th
Pt=0.0254
Pl=0.022
theta=(16*PI)/180
Ntr=2
Aff_air_total=Aff_air*n*6
A_air_total=A_inc_air*n*12
sigma_geo=Aff_air_total/0.7308
alpha_geo=A_inc_air/Vol_inc
Dh_air=((4*Aff_air_total*W_e)/(A_air_total))

"Air properties"
Cp_a=Cp(AirH2O,T=Ta_i,R=R,P=Pa_i)
rho_a=Density(AirH2O,T=Ta_i,R=R,P=Pa_i)
mu_a=Viscosity(AirH2O,T=Ta_i,R=R,P=Pa_i)
k_a=Conductivity(AirH2O,T=Ta_i,R=R,P=Pa_i)
ha_i=Enthalpy(AirH2O,T=Ta_i,R=R,P=Pa_i)
omega_i=HumRat(AirH2O,h=ha_i,R=R,P=Pa_i)

"Air heat transfer coefficient - Dry"
CALL AirHeatTransferCoefficient (Re_Dc,Dc,Dh_air,Fs,Pt,theta,Ntr,Pl:j_dry,f_a)
Re_Dc=(rho_a*V_max*Dc)/mu_a
Pr_a=(Cp_a*mu_a)/k_a
Nuss=j_dry*Re_Dc*Pr_a^(1/3)
Nuss=(h_dry*Dc)/k_a

"Fin efficiency - Dry"
X_L=sqrt((Pt/2)^2+Pl^2)/2
X_M=Pt/2
R_eq/r_o=1.27*(X_M/r_o)*(X_L/X_M-0.3)^(1/2)
PHI=(R_eq/r_o-1)*(1+0.35*ln(R_eq/r_o))
m=sqrt((2*h_dry)/(k_fin*Fin_th))
eta=(tanh(m*r_o*PHI))/(m*r_o*PHI)
eta_o=1-((A_f_inc*n*12)/A_air_total)*(1-eta)

"Air heat transfer coefficient - Wet"
j_wet=0.213262*Re_Dc^(-0.51507)*Ntr^0.09891*(A_air_total/(A_t_inc*n*12))^0.600543*(Fin_th/Pl)^0.072448
Nuss_wet=j_wet*Re_Dc*Pr_a^(1/3)
Nuss_wet=(h_wet*Dc)/k_a

"Fin efficiency - Wet"
m_wet=sqrt((2*h_wet)/(k_fin*Fin_th))
eta_wet=(tanh(m_wet*r_o*PHI))/(m_wet*r_o*PHI)
eta_o_wet=1-((A_f_inc*n*12)/A_air_total)*(1-eta_wet)
```

```
"Mass transfer coefficient"
h_wet/(Cp_a*h_m)=2.28*Ntr^0.2393*(Fs/Dc)^(0.0239*Ntr+0.4332)*(A_air_total/(A_t_inc*n*12))^(0.0321*Ntr+0.0747)*Re_Dc^(-
...0.01833*Ntr+0.194*(Fs/Dc)-0.0026*(Pl/Dc)-0.03012*(Pt/Dc)+0.0418)

"Inlet properties"
Tr_i=5+273.15
x_i=0.45
m_dot_r_total=0.2

Ta_i=25+273.15
R=0.3
Pa_i=85000
V_a=5

"Mass flow"
m_dot_r=m_dot_r_total/12
G=m_dot_r/Aff_ref

V_max=V_a/sigma_geo
m_dot_a=V_a*H_inc*L_inc*rho_a
G_c=m_dot_a/Aff_air

"Inlet refrigerant properties"
rho_f=Density(R744,P=Pr_i,x=0)
rho_g=Density(R744,P=Pr_i,x=1)
rho_r_i=rho_g*x_i+rho_f*(1-x_i)

Cp_f=Cp(R744,P=Pr_i,x=0)
Cp_g=Cp(R744,P=Pr_i,x=1)
Cpr_i=Cp_g*x_i+Cp_f*(1-x_i)

mu_f=Viscosity(R744,P=Pr_i,x=0)
mu_g=Viscosity(R744,P=Pr_i,x=1)
mu_r_i=mu_g*x_i+mu_f*(1-x_i)

k_f=Conductivity(R744,P=Pr_i,x=0)
k_g=Conductivity(R744,P=Pr_i,x=1)
k_r_i=k_g*x_i+k_f*(1-x_i)

hr_i=Enthalpy(R744,T=Tr_i,x=x_i)
sr_i=Entropy(R744,T=Tr_i,x=x_i)
Pr_i=Pressure(R744,T=Tr_i,x=x_i)

"Incremental loop intialisation"
hr_o[0]=hr_i
Pr_o[0]=Pr_i
sr_o[0]=sr_i
Cpr_o[0]=Cpr_i
k_r_o[0]=k_r_i
mu_r_o[0]=mu_r_i
rho_r_o[0]=rho_r_i
x_o[0]=x_i
inc[0]=0

"Main Loop"
n=32
Duplicate i=1,n

"Increment refrigerant side links"
sr_i[i]=sr_o[i-1]
Cpr_i[i]=Cpr_o[i-1]
x_i[i]=x_o[i-1]
k_r_i[i]=k_r_o[i-1]
mu_r_i[i]=mu_r_o[i-1]
rho_r_i[i]=rho_r_o[i-1]
Pr_i[i]=Pr_o[i-1]
hr_i[i]=hr_o[i-1]
inc[i]=inc[i-1]+1

"Increment inlet properties"
Tr_i[i]=Temperature(R744,P=Pr_i[i],h=hr_i[i])
DP[i]=DewPoint(AirH2O,T=Ta_i[i],w=omega_i[i],P=Pa_i[i])

"Refrigerant heat transfer coefficients"
Re[i]=ABS((m_dot_r*D_i)/(mu_r_i[i]*Aff_ref))
Prandl[i]=(Cpr_i[i]*mu_r_i[i])/k_r_i[i]

f_sh[i]=(1.82*log10(Re[i])-1.64)^(-2)
Nuss_sh[i]=(f_sh[i]/8)*(Re[i]-1000)*Prandl[i]*(1.07+12.7*sqrt(f_sh[i]/8)*(Prandl[i]^(2/3)-1))^(-1)
Nuss_sh[i]=(h_sh[i]*D_i)/k_r_i[i]

CALL RefrigerantFlowMap (G,Tr_i[i],hr_i[i],x_i[i],D_i,Aff_ref,A_inc_ref,L_inc,gra,m_dot_r,Pr_i,Q_flux[i]:h_tp[i],h$[i],DELTAP_r[i])
Q_flux[i]=Q[i]/A_inc_ref

h_r[i]=If(x_i[i],0.999,h_tp[i],h_sh[i],h_sh[i])
```

```
"Increment air properties"
rho_a[i]=Density(AirH2O,T=Ta_i[i],w=omega_i[i],P=Pa_i[i])
Cp_a[i]=Cp(AirH2O,T=Ta_i[i],w=omega_i[i],P=Pa_i[i])
h_sw[i]=Enthalpy(AirH2O,T=Tw_o[i],R=1,P=Pa_i[i])
omega_sw[i]=HumRat(AirH2O,T=Tw_o[i],R=1,P=Pa_i[i])
h_g[i]=Enthalpy(Steam,T=Ta_i[i],x=1)
h_w[i]=Enthalpy(Steam,T=Tw_o[i],x=0)
AirState$[i]=If(Tw_o[i],DP[i],'Wet','Dry','Dry')
rho_a_o[i]=Density(AirH2O,T=Ta_o[i],w=omega_o[i],P=Pa_o[i])
rho_a_avg[i]=(rho_a[i]+rho_a_o[i])/2

"Energy conservation"
Q[i]=m_dot_r*(hr_o[i]-hr_i[i])
Q_s[i]=m_dot_a*Cp_a[i]*(Ta_i[i]-Ta_o[i])
Q_l[i]=m_dot_a*h_g[i]*(omega_i[i]-omega_o[i])
Q[i]=Q_s[i]+Q_l[i]

"Characteristic heat ransfer"
Q[i]=h_r[i]*A_inc_ref*(Tw_i[i]-Tr_i[i])

Q_s[i]=If(Tw_o[i],DP[i],h_wet*A_inc_air*eta_o_wet*(Ta_i[i]-Tw_o[i]),h_wet*A_inc_air*eta_o_wet*(Ta_i[i]-Tw_o[i]),h_dry*A_inc_air*eta_o*(Ta_i[i]-
...Tw_o[i]))
Q_l[i]=If(Tw_o[i],DP[i],h_m*A_inc_air*eta_o_wet*(omega_sw[i]-omega_i[i])*(h_w[i]-h_g[i]),h_m*A_inc_air*eta_o_wet*(omega_sw[i]-
...omega_i[i])*(h_w[i]-h_g[i]),0)

"Tube wall conduction"
Q[i]=(2*PI*K_t*L_inc*(Tw_o[i]-Tw_i[i]))/ln(r_o/r_i)

"Increment outlet properties"
Tr_o[i]=Temperature(R744,h=hr_o[i],P=Pr_o[i])
sr_o[i]=Entropy(R744,h=hr_o[i],P=Pr_o[i])
x_o[i]=Quality(R744,h=hr_o[i],P=Pr_o[i])
Call Specificheat_out (x_o[i],Pr_o[i],hr_o[i]:Cpr_o[i])
Call Conductivity_out (x_o[i],Pr_o[i],hr_o[i]:k_r_o[i])
Call Viscosity_out (x_o[i],Pr_o[i],hr_o[i]:mu_r_o[i])
Call Densityrho_out (x_o[i],Pr_o[i],hr_o[i]:rho_r_o[i])

RH_o[i]=RelHum(AirH2O,T=Ta_o[i],w=omega_o[i],P=Pa_o[i])

"Conservation of momentum - Air"
Pa_o[i]-Pa_i+DELTAPa_0L[i]=0
DELTAPa_0L[i]=m_dot_a^2/(2*rho_a[i]*Aff_air^2)*((1-(Aff_air/(L_inc*H_inc))^2)*(rho_a[i]/rho_a_o[i]-
...1)+2*f_a*(A_inc_air/Aff_air)*(rho_a[i]/(rho_a[i]+rho_a_o[i])))

"Conservation of momentum - Refrigerant"
Pr_o[i]-Pr_i[i]+DELTAPr_0L[i]=0
DELTAPr_0L[i]=DELTAP_r[i]

END

"Increment air side links"
n_half=n*0.5
n_onehalf=n*1.5
Duplicate i=1,(n/4)
Ta_i[i]=AVERAGE(Ta_o[n_half-i+1],Ta_o[n-i+1])
omega_i[i]=AVERAGE(omega_o[n_half-i+1],omega_o[n-i+1])
Pa_i[i]=AVERAGE(Pa_o[n_half-i+1],Pa_o[n-i+1])
END
Duplicate i=(n/4+1),(n/2)
Ta_i[i]=Ta_i
omega_i[i]=omega_i
Pa_i[i]=Pa_i
END
Duplicate i=(n/2+1),(n/2+n/4)
Ta_i[i]=AVERAGE(Ta_o[n-i+1],Ta_o[n_onehalf-i+1])
omega_i[i]=AVERAGE(omega_o[n-i+1],omega_o[n_onehalf-i+1])
Pa_i[i]=AVERAGE(Pa_o[n-i+1],Pa_o[n_onehalf-i+1])
END
Duplicate i=(n/2+n/4+1),n
Ta_i[i]=Ta_i
omega_i[i]=omega_i
Pa_i[i]=Pa_i
END

"Circuit outlet properties"
Ta_o=AVERAGE(Ta_o[1..8],Ta_o[17..25])
omega_o=AVERAGE(omega_o[1..8],omega_o[17..25])
Pa_o=AVERAGE(Pa_o[1..8],Pa_o[17..25])
RH_o=RelHum(AirH2O,T=Ta_o,w=omega_o,P=Pa_o)
ha_o=Enthalpy(AirH2O,T=Ta_o,w=omega_o,P=Pa_o)

Tr_o=Temperature(R744,h=hr_o[n],P=Pr_o[n])
Pr_o=Pr_o[n]
DELTA_Pr=Pr_i-Pr_o[n]
```

"Specific values"
LMTD=((Ta_i-Tr_o)-(Ta_o-Tr_i))/(ln((Ta_i-Tr_o)/(Ta_o-Tr_i)))
LMED=((ha_i-hr_o[n])-(ha_o-hr_i))/(ln((ha_i-hr_o[n])/(ha_o-hr_i)))

Q_tube1=SUM(Q[i],i=1,8)
Q_tube2=SUM(Q[i],i=9,16)
Q_tube3=SUM(Q[i],i=17,24)
Q_tube4=SUM(Q[i],i=25,32)

DELTAP_tube1=SUM(DELTAP_r[i],i=1,8)
DELTAP_tube2=SUM(DELTAP_r[i],i=9,16)
DELTAP_tube3=SUM(DELTAP_r[i],i=17,24)
DELTAP_tube4=SUM(DELTAP_r[i],i=25,32)

Ta_o_tube1=AVERAGE(Ta_o[1..8])
Ta_o_tube2=AVERAGE(Ta_o[9..16])
Ta_o_tube3=AVERAGE(Ta_o[17..24])
Ta_o_tube4=AVERAGE(Ta_o[25..32])

RH_o_tube1=AVERAGE(RH_o[1..8])
RH_o_tube2=AVERAGE(RH_o[9..16])
RH_o_tube3=AVERAGE(RH_o[17..24])
RH_o_tube4=AVERAGE(RH_o[25..32])

"Evaporator heat transfer rates"
Q_s_total=SUM(Q_s[i],i=1,n)*12
Q_l_total=SUM(Q_l[i],i=1,n)*12

Q_total=Q_s_total+Q_l_total